Engineering quantum light-matter interactions in solid-state platforms

Martin Nicolle

Department of Physics
University of Bristol

A dissertation submitted to the University of Bristol in accordance with the requirements for award of the degree of Doctor of Philosophy in the Faculty of Physics

July 2020

Word count: Thirty-five thousand three hundred and ninety-two

Abstract

Optical quantum technologies are a cornerstone of many scalable quantum information processing architectures, such as quantum computation and communication networks. However, scaling up these such systems to support large quantum states is challenging due to the probabilistic nature of photonic quantum operations. Optical quantum memories - devices capable of storing and releasing light on-demand - have been identified as a solution to this scalability issue through the use of multiplexing schemes. Ensembles of solid-state quantum emitters are a promising medium for the implementation of a quantum memory, especially due to their compatibility with integrated devices.

In this thesis, we focus on the development of platforms enhancing the performance of current solid-state quantum memories. The atomic frequency comb (AFC) protocol is an attractive approach to quantum light storage in solid-state media. Here, we demonstrate an implementation of the AFC rephasing technique in Pr^{3+}:Y_2SiO_5 in a novel broadband regime. We also report on initial results towards the realisation of broadband memory employing cascaded two-photon absorption in the system.

Ensembles of nitrogen-vacancy centres in diamond are a promising alternative to Pr^{3+}:Y_2SiO_5, due to long spin coherence times and a large ground state splitting. Nitrogen-vacancy centres were investigated as a host for a broadband implementation of the AFC protocol. We demonstrate spectral hole burning based on optically-induced ionisation of the negative charge state of the defect. Using this technique, an atomic frequency comb is successfully prepared, paving the way for the development of an AFC quantum memory in this platform.

Another approach to light-matter interactions in atomic ensembles is investigated in the form of systems based on atomic arrays. We theoretically study collective phenomena in arrays of nitrogen-vacancy centres, focusing on a promising use case where a single defect can be strongly coupled to an optical cavity composed of atomic mirrors.

Acknowledgements

I will look back fondly at the past few years spent in Oxford and Bristol, which were undeniably the most colourful and stimulating in my life. Throughout, I was lucky to have been supported by incredible people, to whom I would like to offer of word or two of thanks.

First of all, thanks to Josh for introducing me to Ultrafast, and for encouraging me through the highs and lows of the PhD. Your infectious enthusiasm, crazy ideas and hastily scribbled lambda-systems constantly reminded me of how much fun all of this is. I am most honoured to have been part of the (real)DNation, whose members have taught me everything I know. Jonas, Patrick, I cannot understate how lucky I was to work alongside you and to have you as mentors. Thanks for the insights, the guidance and the banter. I promise to do my best to continue the legacy of operation fillDemgaps. It was also a pleasure to work with Christian, who introduced me to the memory lab with much patience and good humour.

I was happy to share the Ultrafast group with a crew of incredible people - thank you for the infinite cups of tea and the Half-Moon Mondays! Thanks in particular to the memories team for creating such a friendly environment, it was a pleasure to share a lab with all of you. And of course, thank you to Ian for building the group as I knew it.

Cohort II made my year spent in Bristol magical, thanks to all of you for the good times in the CDT office. I'm incredibly grateful for how supportive the CDT has been, and in particular for Chris and Pete's guidance and wisdom throughout the process of finding a PhD project. Thanks also to Jonathan for bearing with me and supervising my progress from the Bristol side. Your advice has kept me together and let me focus on looking forwards.

Thanks to my friends back in Paris! To Bozzio, with whom I started on the quantum path back in the Flomi days, as well as Payot, Vidipt and Brodie for their support going during all these years.

Thanks also to Suguru, Takahiro and Sunami for the many random discussions, and for teaching me so much about the wider quantum world. I'm happy I could share my time in Oxford with you. While I'm at it, thanks to the hanchankai: I think that in a convoluted way, weekly mahjong might have been what kept me sane.

Thank you to Risa for putting up with me, and whose unwavering support means so much. And finally, thanks to my family. To Da, who set me on this path and to Mum and Louise who brought me here.

Declaration

I declare that the work in this dissertation was carried out in accordance with the requirements of the University's Regulations and Code of Practice for Research Degree Programmes and that it has not been submitted for any other academic award. Except where indicated by specific reference in the text, the work is the candidate's own work. Work done in collaboration with, or with the assistance of, others, is indicated as such. Any views expressed in the dissertation are those of the author.

SIGNED: ..... DATE: .....

Manuscripts and Presentations

Manuscripts

"Gigahertz-bandwidth atomic frequency comb optical memory with a Pr^{3+}:Y_2SiO_5 crystal"

M. Nicolle, J. N. Becker, C. Weinzetl, I. A. Walmsley, and P. M. Ledingham

In preparation

"Collectively-enhanced light-matter interactions in ordered arrays of solid state quantum emitters"

M. Nicolle *et al.*

In preparation

Presentations

"Enhanced light matter interactions in ordered arrays of diamond nitrogen vacancy centres"

M. Nicolle, J. N. Becker, J. Nunn, P. M. Ledingham, and I. A. Walmsley

(Poster) *CLEO/Europe-EQEC 2019, June 2019, Munich, Germany*

"Enhanced light matter interactions in ordered arrays of diamond nitrogen vacancy centres"

M. Nicolle, J. N. Becker, J. Nunn, P. M. Ledingham, and I. A. Walmsley

(Poster) *693. WE-Heraeus-Seminar on Diamond Quantum Technologies, March 2018, Bad Honnef, Germany*

Table of contents

List of figures

List of tables

Chapter 1

Introduction

Technologies harnessing the peculiar properties of quantum entanglement and superposition carry the promise of revolutionary developments spanning many fields of science. A century after the foundations of quantum mechanics were laid out, experimental progress has finally advanced to a point where the realisation of quantum-enhanced devices is a near-term prospect. Quantum technologies pave the way to fundamentally novel approaches to engineering and information processing. These are broadly divided into applications including computation [1], communication [2], sensing [3], and the simulation of physical systems [4, 5].

The building blocks of such devices are quantum bits, or 'qubits' [6], which evolve according to the laws of quantum mechanics, thereby granting them certain benefits over their conventional counterparts. While classical bits can only represent a 0 or a 1, qubits can exist in any superposition of these two states. The number of states contained in the superposition scales exponentially with the size of the device, as a system of n qubits can support 2^n possible states [7]. The field of quantum computation is built around the implementation of algorithms which take advantage of this property to perform calculations beyond the scope of current machines. For example, these devices are particularly suited to search through a large parameters spaces due to the sheer number of states accessible simultaneously via quantum superposition [8–10]. Beyond computation, quantum bits can be used to ensure the security of cryptography protocols. Indeed, as quantum states are extremely sensitive to external disturbance, two communicating parties can be instantly alerted to the presence of an eavesdropper [11].

While the past decades have seen a headlong rush for the development of quantum devices, the jury is still out concerning which physical system will provide the best

platform [1]. As any quantum system which can support two orthogonal states can constitute a qubit, a wide range of candidates have emerged. Undoubtedly, devices based on superconducting circuits have led the race to achieve useful quantum computation. This has been accompanied by a recrudescence in the number of industrial players and the recent demonstration of a quantum device outperforming classical computation on a specific problem [12]. Alternatives include photons [13] and atom-like systems such as trapped ions [14] and solid-state emitters [15, 16], each coming with their own strengths and drawbacks. The performance of qubits is often weighed against a set of criteria defined by DiVincenzo twenty years ago [17], which remain remarkably relevant today. For instance, methods must exist to initialise, perform quantum operations on and measure the state of the system which should also exhibit long coherence times. Above all, a qubit design must be *scalable*. That is, many qubits must be connected in a way that allows the generation of large entangled quantum states. This requirement is absolutely crucial for most applications, and particularly so for computations. Unfortunately, scalability has also been the most challenging criteria to meet, and has not been achieved convincingly in any existing system [1]. It could be said that the development of a truly scalable qubit design is the greatest hurdle standing in the path of useful quantum technologies.

Faced with this challenge, one can consider combining different physical systems in order to create a platform which compensates for the weaknesses of its components [18, 19]. This is the basis of a scalable quantum information processing architecture known as quantum networks [20]. Quantum networks are composed of channels connecting nodes capable of processing and transmitting quantum information. These structures are remarkably flexible, and can either be used to facilitate computation on a local scale, or to distribute quantum information over large distances [21]. One popular approach is to connect atomic systems via optical interlinks [22], with the aim of addressing the limited scalability of atomic qubits. For example, current trapped ion systems are restricted to a small number of emitters interacting in a single trap. Photonic channels could then be used to distribute entanglement between separate traps in order to generate larger quantum states [23].

Conversely, atomic systems also offer a way of tackling the challenges inherent to optical quantum information processing schemes. While light is particularly suited for both miniaturisation [24] and information transfer, photons are particularly difficult to interface with each other. This has forced the implementation of photonic two-qubit operations to rely on probabilistic processes, making the creation of large quantum

states a long-standing issue [25]. Furtheremore, light-mediated distribution of atomic qubit entanglement also relies on two-photon interference. As a result, the non-deterministic nature of photonic operations undermines the scalability of quantum networks based on atomic nodes [26].

A solution to this challenge revolves around the use of optical quantum memories [27], devices allowing the on-demand storage and retrieval of a single photon's quantum state [28]. Given such a component, one can efficiently compensate for the probabilistic nature of quantum photonic operations with multiplexing schemes [29, 30]. Quantum memories thus offer a clear avenue towards scalable designs for both atomic and photonic quantum information processing schemes [31, 32].

A popular approach to building a quantum memory involves mapping an optical signal to the long-lived coherence of an atomic platform. The potential of such hybrid devices has motivated a significant amount of research efforts towards building an efficient light-matter interface, and led to many fascinating experimental results [31]. The most direct way of coupling an atom to light is to focus an optical beam as tightly as possible [33]. However, in this case, the interaction is severely hindered by the diffraction limit. A promising alternative is to use dielectric structures such as waveguides or cavities to confine the electromagnetic field in the vicinity of the atom. Interfaces based on Fabry-Pérot resonators [34] and optical nanofibres [35] have thus enabled the experimental demonstration of efficient interactions between single photons and trapped atoms. Quantum memories have in this way been implemented with single emitters carefully placed inside optical cavities [36].

These systems would be suitable candidates for quantum memories if it were not for demanding practical requirements. Indeed, they are typically challenging to build and maintain over extended periods of time. Another approach to deterministic light-matter coupling involves atomic ensembles, in which case the interaction probability scales linearly with the number of atoms [37]. As protocols based on atomic ensembles do not rely on engineering the dielectric environment of the system, their implementation is also often less technically demanding. This makes them an attractive platform for the realisation of quantum memories, for example enabling one of the first demonstrations of on-demand single-photon storage and retrieval [38].

The difficulty of satisfying scalability requirements with bulk optical systems has pushed research endeavours away from free space and towards integrated systems [39]. This avenue shows great promise as a single chip can hold hundreds of artificial

'atoms' which can then be interfaced with via nanophotonic structures generated by reproducible fabrication techniques [40, 41].

Interest in solid-state emitters is by no means a recent affair, as advances in our understanding of their properties have paved the way for modern optical technologies through the invention of fibre amplifiers and solid-state lasers [42]. And thus, decades of research into defects in solids as gain media now provide a knowledge base for the development of optical quantum technologies. Although the energy level structures of many solid-state emitters are understood, qubits have requirements that differ significantly from classical devices. In order to develop efficient systems, it is necessary to scout out platforms that have strong and well-defined optical transitions while also supporting long-lived ground states. Atomic emitters such as quantum dots [43], colour centres in diamond [44] and rare-earth ions [45] have been investigated as prime candidates for the realisation of solid-state quantum memories [46, 47].

Building a quantum memory not only requires an intimate knowledge of light-matter interaction but also a collection of robust control techniques. For example, system initialisation often relies on optical pumping schemes [48], and efficient spectral hole burning is a requirement for many protocols in inhomogeneously broadened media [49]. The aim of our work is to contribute novel approaches to the current set of tools used to engineer quantum light-matter interactions in solid-state platforms. We focus on atomic ensembles, and consider two types of emitters: praseodymium ions doped into a crystalline host and nitrogen-vacancy colour centres in diamond. The first part of this thesis concerns the experimental realisation of broadband quantum memories. In a later chapter, we study an alternative approach to light-matter interactions in atomic ensembles, based on optical cavities engineered from ordered arrays of emitters.

Outline

The thesis is structured as follows:

- Chapter 2 is a general introduction to the field of quantum memories. We briefly detail why they are so important to the development of quantum networks, then provide a brief overview of some major quantum memory protocols. Particular attention is given to the atomic frequency comb rephasing technique, which forms the basis of much of the work contained in the rest of the thesis.

- In Chapter 3, we introduce rare-earth ion doped solid, a promising platform for the implementation of quantum memories. Starting from the physical nature of the system, we explain how their electronic structure gives rise to their optical properties. A focus is made on praseodymium ions doped into a orthosilicate host, which is the system chosen for the experiments presented in the following chapter.

- In Chapter 4, we experimentally study a broadband implementation of the atomic frequency comb rephasing protocol in Pr^{3+}:Y_2SiO_5. A novel approach to spectral hole burning in the system is designed and implemented. This method is used to successfully store and retrieve optical pulses which match the inhomogeneous linewidth of the material, thereby going far beyond the limit imposed by the hyperfine state splitting of praseodymium.

- Chapter 5 introduces a well-known quantum solid-state platform in the form of nitrogen-vacancy colour centres in diamond. As was done for rare-earth ions, we explore how the optical response of the system arises from its physical nature. The energy level structure of the system is detailed, explaining the processes that shape its emission spectrum. We also provide an overview of its optical, spin and charge state dynamics along with a short introduction to common techniques used to control each of these degrees of freedom.

- Chapter 6 reports the results of a new spectral hole burning technique in ensembles of nitrogen-vacancy centres, based on light-induced ionisation of the defect's charge state. Ionisation transients in the system are briefly studied in order to scope out the charge state dynamics in the system. This investigation is followed by the first successful observation of an atomic frequency comb in an ensemble of NV centres.

- Chapter 7 focuses on how atomic arrays can form the basis of a promising new way of interfacing light and atoms. We start by laying down a physical model allowing the description of these phenomena which arise from the interference of light emitted by regularly spaced dipoles. We see how these collective effects can modify the optical properties of the array, and how this can be applied to light-matter interaction schemes. This formalism is then applied to the particular case of arrays of nitrogen-vacancy centres, and we theoretically investigate how realistic imperfections can affect the observation of collective effects. We consider

an interesting use case of these phenomena, whereby atomic arrays can become highly-reflective atomic mirrors which can then be used to form a cavity enabling the optical interfacing of solid-state quantum emitters.

- We conclude in Chapter 8 with a summary of the work presented throughout this thesis, providing an outlook on prospects for further research.

Chapter 2

Optical quantum memories

An optical quantum memory refers to any device which can coherently store an optically-encoded quantum state and retrieve it at a later time. The process should also be on-demand, i.e. it must be possible to choose the storage and retrieval timings at will. This type of operation is most commonly implemented by mapping the optical signal onto the coherence of an atomic or atom-like system. In this chapter, we review some of the main protocols for the experimental realisation of quantum memories. We start by making the case for quantum memories, explaining why they are such a crucial component for the success of optical quantum technologies. We then follow with a brief description of the physics behind the storage and retrieval of single photons in atomic ensembles. This leads to a description of a few common quantum memory protocols underpinning much of the work presented further in this thesis.

2.1 Applications of quantum memories

Many of the operations enabling optical quantum technologies are currently probabilistic in nature. Desired applications often rely on scaling up devices to systems where many concurrent operations are successfully performed in a single sequence. If the implementation of a single operation is inherently probabilistic, the performance of the system scales unfavourably. In this section, we outline various ways in which quantum memories can enhance the performance of photonic quantum devices.

2.1.1 Limitations of photonic quantum technologies

Optical quantum systems are an attractive system for the implementation of quantum technologies. As photons are insensitive to thermal noise and are easily transported across large distances, they offer properties that differ much from commonly used atom-like systems such as superconducting transmons or trapped ions. They also support a wide range of encoding bases [50–54] which can allow for easy to implement single-qubit operations. These aspects have consolidated optical technologies as the main platform for quantum communications [55, 56] and a notable contender for the implementation of quantum computation schemes [57].

Of course, this is balanced by a major disadvantage: photons are notoriously difficult to interface with each other. As a result, realising the deterministic two-qubit interactions necessary for many quantum computation models has proven a major challenge in optical systems. Linear optical quantum computing (LOQC) schemes [58, 59] tackle this problem with probabilistic gates [60, 61] which inherently limits their scalability. Furthermore, deterministic sources of pure and indistinguishable single photons are vital for photonic quantum information schemes [62]. While great progress has been made towards developing such devices, reaching performances sufficient to generate large [63] quantum states remains a challenge [64]. Sources based on spontaneous parametric down-conversion (SPDC) [65] can produce single photons with highly desirable purity and indistinguishability properties [66–68]. These sources only have a small chance of producing a single photon in a given time bin, making the process probabilistic. In general, the single photon generation probability of the source must be limited artificially to $\sim 1\%$ in order to avoid the production of multi-photon states [69], meaning that a compromise must be made between the quality of the output field and the photon production rate. Furthermore, the spectrum of the photons produced is typically very wide, up to several THz, whereas the acceptance bandwidth of typical storage media is in the MHz-GHz range. As a result, the source often has to be spectrally filtered down to match the memory which highly limits its brightness [70]. Alternatively, SPDC sources have been placed inside a cavity to produce narrowband photons, at the expense of a considerable increase in experimental complexity [71–73].

Sources based on single quantum emitters [74–76] - quantum dots in particular[77] - offer a promising alternative. The non-linear nature of single atomic systems allow the development of deterministic 'push-button' devices. Single-photon sources based on quantum dots in integrated nanocavities have shown exceptional output rates [78]. Such devices are currently limited by frequency jitter in the emission caused

by environmental fluctuations. This instability reduces the indistinguishability of the output single photons, for example via mechanisms further elucidated in Ref. [79]. Furthermore, although quantum dot sources are in principle deterministic, the probability of generating a single photon in a given spatial mode is determined by the collection efficiency of the source. This figure is currently limited to $\sim 80\%$ in state-of-the-art experimental realisations, leading to overall single-photon generation efficiencies of $\sim 57\%$ [80, 81].

Currently, limitations in both photonic two-qubit gates and single-photon sources force optical quantum information processing protocols to rely on probabilistic processes. Performing a computation involves the successful implementation of many such operations in quick succession. In this case, the overall success probability becomes vanishingly small as the number of operations increases. For example, even if a flipped coin has a 90% chance of returning heads, the probability of this coin landing heads a hundred times in a row is vanishingly small. Quantum memories offer a solution to this issue by storing the successful subsets of a system and thus allowing each operation to be attempted independently. So to speak, we can keep the coins that land heads and flip the other ones until satisfactory results are achieved.

2.1.2 Quantum repeaters

Quantum communication schemes based on quantum key distribution (QKD) rely on the no-cloning property [82] of quantum information to ensure secure information transfer between two parties [83]. According to the no-cloning theorem, an arbitrary quantum state cannot be copied without affecting the original. This feature is also the source of one of the main limitations of existing implementations of QKD protocols. Optically encoded channels carried by optical fibre are overwhelmingly the best candidate for sending quantum information over long distances. However, this means that the transmission is subject to fibre losses, which are typically around 0.2 dB/km for telecom photons - after 100 km, 99% of the signal is lost [30]. In the case of classical communications, this issue is solved by using repeater stations which amplify and re-emit the signal to extend the range of the channel [84]. As the single photons carrying quantum information in QKD schemes are subject to the no-cloning theorem, [85], they cannot be amplified without adding noise which precludes the use of an analogue to the classical approach.

One possible way of overcoming this challenge is by dividing the transmission link into shorter segments connecting nodes over which entanglement can be faithfully

established. Then, the entanglement needs to be shared between the segments, which can be achieved using a technique known as entanglement 'swapping' [86]. This idea, shown in Fig. 2.1 forms the basis of so-called 'quantum repeaters' [87]. For example, if pairwise entanglement exists between pairs of nodes 1 and 2, and 3 and 4, a Bell-state measurement can be applied between nodes 2 and 3 in order to entangle 1 and 4.

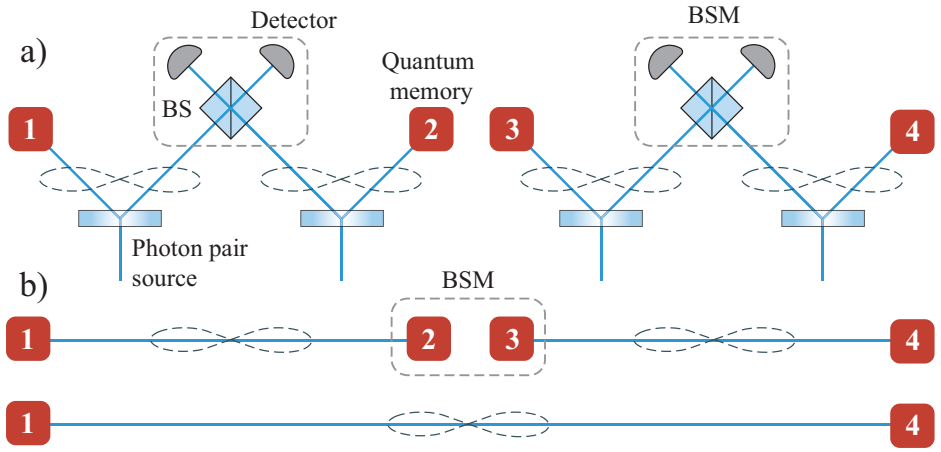

Fig. 2.1 : (a) Example of a quantum repeater protocol relying on quantum memories. Two photon sources each produce a pair of entangled photons, and one of each pair is stored in a quantum memory. The other two photons, one from each source, are interfered on a beam splitter (BS). The detection of a photon at either output of the BS is equivalent to a Bell-state measurement and yields entanglement between the two quantum memories. (b) Once pairwise entanglement has been established between memories (1 and 2), and (3 and 4), another Bell-state measurement can be performed between memories 2 and 3 to yield entanglement 1 and 4.

The mains drawback of this technique is that the photonic Bell-state measurement is applied through linear optical operations - for example via interference on a beam splitter - making it probabilistic. As a result, most schemes for the experimental realisation of a quantum repeater rely on the use of quantum memories to synchronise successful entanglement swapping events[30]. In this case, all of the Bell-state measurements do not have to be successful at once, as one has the option to store the successfully entangled photons while the operation is attempted again on the segments that failed the first time. A possible scheme using quantum repeaters for entanglement distribution is shown in Fig. 2.1.

While repeater schemes can be implemented with any on-demand quantum memory, the efficiency and repetition rate of the process must be such that the performance of the system surpasses that which can be achieved with just a lossy fibre link. Overall, quantum repeaters are considered the cornerstone of quantum networks, making the

development of quantum memories essential for distributed quantum communication and computing schemes.

2.1.3 Single-photon synchronisation and filtering

Quantum memories can also be used to synchronise operations on a local scale, for example in the context of LOQC. Photonic two-qubit gates are also implemented with linear operations, for example by interfering photons on a beamsplitter, a probabilistic process somewhat similar to the Bell-state measurements mentioned above. A 'repeat until success' strategy can thus also be used in this context. Photonic quantum computing protocols often rely on the generation of a multi-photon state based on simultaneous preparation of N photons in N modes of an interferometric device. With current probabilistic single-photon sources, achieving even 10-photon states is a challenging task which requires many hours of data accumulation [88, 89]. This can be understood as the probability p of producing N single photons simultaneously given the same number of sources with heralding probability q scales as $p \sim q^N$. According to a scheme proposed by Nunn *et al.*[29], using quantum memories to store successfully generated photons until they can all be released simultaneously greatly increases multiphoton rates (see Fig. 2.2). This analysis also suggests that for this application the bandwidth of the memory is just as important as its efficiency, while the storage time itself can be relatively short depending on the sources used. The bandwidth of the memory sets a lower bound on the temporal length of photons which can be stored, which in turn defines the maximum repetition rate of the multiplexing scheme. A memory with a large bandwidth is thus key to reduce the time necessary to generate many-photon states.

A recent result has also shown that quantum memories can also be used as coherent filters for single-photon sources with non-ideal properties such as low indistinguishability [90]. This scheme employs the single-mode aspect of certain quantum memory protocols to produce identical photons from distinguishable noisy sources without reducing their brightness as much as conventional filtering methods. This type of 'quantum buffer' is particularly suited for mitigating the temporal-spectral jitter of quantum dot sources.

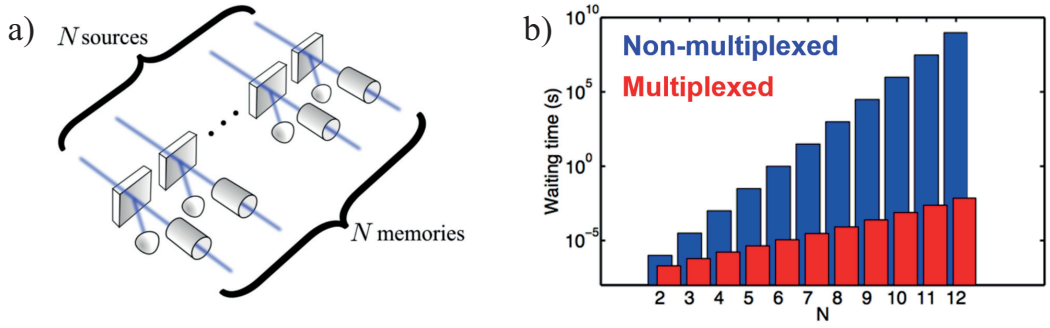

Fig. 2.2 : (a) Multiplexing scheme for the generation of N-photon states using quantum memories. The storage of a single photon generated by a pair source in a quantum memory is signalled by the detection of the other photon in the heralding arm. Once N memories in N spatial modes are successfully loaded with a single photon, all photons can be released simultaneously for use in any experiment. Figure from [29]. (b) Expected waiting time required for the generation of an N-photon quantum state, comparing the use of unsynchronised SPDC sources to the memory-synchronised case.

2.2 Figures of merit

The performance criteria for quantum memories vary greatly depending on the application considered [91]. A brief summary of the main figures of merit used to assess the capabilities of a quantum memory is provided below.

- **Efficiency**
  An efficient quantum memory can store and retrieve an optical quantum state with low losses. The efficiency of the memory is defined as the ratio of the retrieved pulse energy to that of the input pulse. As losses are detrimental to virtually every quantum information protocol, efficiency is one of the most important figures of merit for a quantum memory.

- **Storage time**
  In the case quantum memories based on atomic systems, a quantum state encoded into a single photon is mapped onto an atomic excitation. The maximum storage time of the memory is limited by the decoherence mechanisms specific to the atomic medium. The storage time is typically defined as the $1/e$ decay time of the stored atomic excitation. In the context of quantum repeaters, the storage time must be at least as long as the average time required to successfully entangle photonic qubits [30].

- **Bandwidth**
  The spectral profile of the optical signal to be stored must be compatible with the acceptance bandwidth of the memory. This bandwidth defines the length of photons which can be read into the system, and thus the maximum repetition rate a protocol can be run at.

- **Time-bandwith product**
  The time-bandwidth product, straightforwardly defined as the product of the storage time of the memory with its bandwidth characterises the maximum of storage attempts that can be performed within the lifetime of the memory. This quantity is particularly relevant when evaluating the performance of a memory for multiphoton synchronisation schemes [29].

- **Fidelity**
  The fidelity $\mathcal{F}$ of a memory represents the similarity between the input and output quantum states. It is often quantified by calculating the overlap between the read-in and read-out density matrices ρ_{in} and ρ_{out} following [92]

$$\mathcal{F} = \mathrm{Tr}\left[\sqrt{\sqrt{\rho_{in}}\rho_{out}\sqrt{\rho_{in}}}\right]^2. \tag{2.1}$$

  The fidelity encompasses crucial information such as the effect of storage on the photon statistics of the input state and the amount of noise injected during the process. $\mathcal{F}$ is bounded by 1 for a fully quantum process and is limited to 2/3 in the classical case [93]. A value $\mathcal{F} > 2/3$ for single qubits is thus required in order to ensure that the quantum nature of the protocol is not compromised (this value increases to $(N+1)/(N+2)$ for N qubits).

- **Multimode capacity**
  The modal capacity refers to the number of modes (spectral, temporal, spatial...) [94–96] which can be stored inside the memory at any given time. For atomic ensembles, this property depends on the optical depth of the system according with a scaling particular to each storage protocol [97]. Multimodality is particularly desirable in context of quantum repeaters, as a memory which can store N modes can can used to increase the success probability of the protocol by a factor of N via a multiplexing approach [98, 99]. On the other hand, single-mode memories are required for single-photon filtering applications [90].

- **Operating wavelength**
  Quantum communications heavily rely on the use of optical fibre to transport optical signal and operate in a frequency windows where absorption losses are minimised, such as the telecom O-band (from 1250 nm to 1360 nm) and C-band (from 1530 nm to 1560 nm). A memory compatible with this wavelength range is thus particularly attractive for quantum repeater applications. Frequency conversion schemes [100, 101] can be used to account for an eventual wavelength mismatch between components but reduce the overall efficiency of the process. In the context of the repeater protocol shown in Fig. 2.1, photon pair sources with different signal and idler frequencies, as in Ref. [46], offer an alternative approach at of the cost of an increaed technical overhead. In the context of optical quantum computing schemes, the memory also needs to be compatible with single-photon sources and eventual waveguides used to build photonic networks.

More detail can be found in Ref. [102] along with an evaluation of certain memory protocols in the light of these criteria.

2.3 Quantum memory protocols in atomic ensembles

Significant experimental efforts were assigned towards the development of reliable quantum memories as their importance for optical quantum information processing became increasingly clear over the years. Many novel schemes have been proposed and implemented in a wide variety of systems, a extensive review of which can be found in references [30]. Here, we outline a subset of these protocols relevant to the results presented later in this thesis.

The storage medium of a quantum memory can consist of any physical system as long as the mechanism can be triggered on-demand and preserves the state of a single read-in photon. For example, an entirely photonic quantum memory can be realised by routing a single photon in and out of an optical cavity with an electro-optical switch. The multiplexing of two independent single-photon sources was successfully demonstrated with such a device boasting a storage time of 830 ns and output photons with high indistinguishability [103]. The lifetime of cavity-based all-photonic memories is limited to tens of nanoseconds by optical losses while increasing the bandwidth requires shorter round-trip times (and thus higher losses) and faster switches than the

currently achievable to the GHz range. As a result, improving these systems beyond their current performance is a potentially challenging task.

Another approach to quantum memories involves the use of single quantum emitters. In this case, the quantum state of a single photon is mapped onto the coherence of an atomic state. Mappings of this sort have been achieved in many different systems, from trapped atoms [36] or ions [104] to solid-state systems such as colour centres in diamond [47, 105]. The performance of the process is determined by the light-matter coupling. Beyond the oscillator strength, this coupling depends mainly on how well the bandwidth and spatial cross-section of the optical signal match that of the atomic emitter, and is typically weak in free-space systems. Photonic cavities are often used to increase the interaction strengths, but such systems are technically challenging to engineer (particularly so in the solid-state) and severely limit the acceptance bandwidth of the device.

The light-matter coupling of an atomic system can otherwise be enhanced by increasing the number of emitters by making use of atomic ensembles. As the probability of a single photon to interact with the ensemble scales linearly with the number of atoms, the efficiency of the process can be increased without the need for significant technical improvements. A wide variety of quantum memory protocols have been designed and implemented in systems such as warm [106] or cold atomic vapours [107], as well as crystals doped with rare-earth ions [108]. Research efforts have led to individual demonstrations of quantum memories with storage times in excess of one second [109] or efficiencies higher than 85% [110]. However, there currently exists no device which satisfies all of the requirements of scalable quantum information processing, prompting the need for further research. Quantum memory schemes in atomic ensembles can be broadly separated into two categories: protocols which rely on the rephasing of atomic dipoles [49] and protocols in which the storage and retrieval mechanisms are enabled by externally triggered two-photon processes.

2.3.1 Optically-controlled memories

A common approach to photon storage in atomic media involves the mapping of the optical field to a long-lived atomic coherence. However, this device is only fully 'on-demand' if the memory process can be triggered at will. This can be achieved via the application of a 'control' optical field in a system with a lambda-type energy level structure with two ground states $|g\rangle$ and $|s\rangle$ and an excited state $|e\rangle$ as shown in Fig. 2.3. The ground states are both connected to the excited state via optical

transitions while the $|g\rangle \leftrightarrow |s\rangle$ transition is forbidden by selection rules. Applying a strong optical field to the $|s\rangle \leftrightarrow |e\rangle$ transition modifies the absorption of a 'signal' field resonant with the $|g\rangle \leftrightarrow |e\rangle$ transition. This type of system can operate in different regimes depending on the detuning Δ of the fields from their respective resonance, leading to different memory protocols.

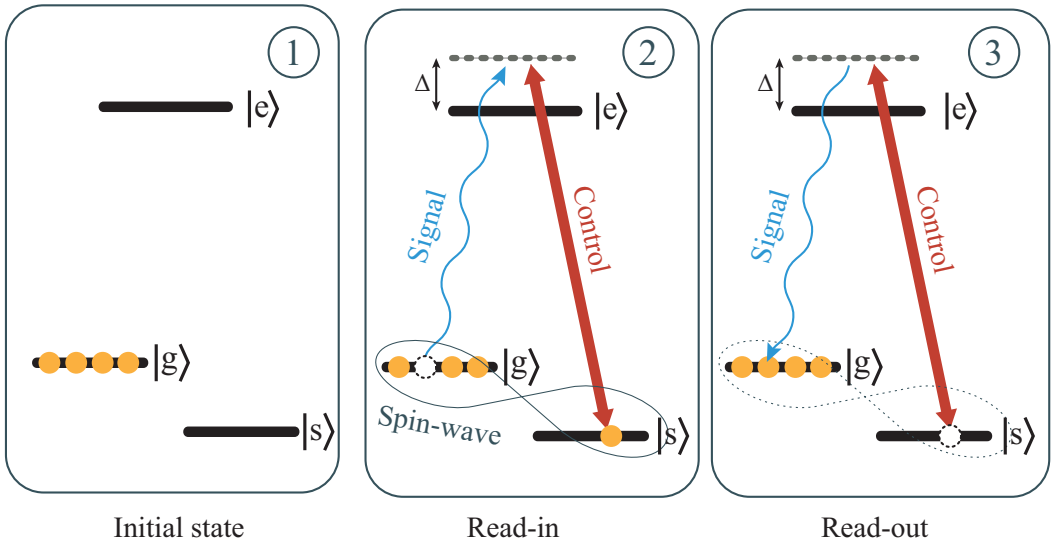

Fig. 2.3 : Quantum memory schemes in atomic Λ-systems. (1) Optical pumping techniques are used to initialise the state of an atomic ensemble into the ground state $|g\rangle$. (2) A signal absorbed on the $|g\rangle \leftrightarrow |s\rangle$ transition is coherently mapped to a collective coherence of the ground states $|g\rangle$ and $|s\rangle$, or 'spin-wave', via the application of a control field applied to the $|e\rangle \leftrightarrow |s\rangle$ transition. (3) The signal field can be read out via a subsequent application of the control field, mapping the spin-wave back onto an optical field. In the EIT protocol, both fields are resonant with their respective transition with $\Delta \ll \Gamma$, whereas in the in Raman case both fields satisfy a two-photon resonance condition with $\Delta \gg \Gamma$.

When Δ is smaller than the linewidth of the excited state Γ, the application of the control field creates a small window of transparency around the signal frequency - a phenomenon known as electromagnetically induced transparency (EIT) [111]. Following the Kramers-Krönig relations, this effect is associated with the emergence of a strongly dispersive feature on resonance which slows down the group velocity of the signal field to a halt. If the control field is adiabatically switched off, this feature disappears, transferring the signal onto a collective ground state coherence of the atomic ensemble. This process can be reversed at will simply by turning the control field on again. The storage and retrieval processes were shown to be equivalent under time-reversal symmetry in theoretical work by Gorshkov *et al.* [112]. The first quantum memories

were based on EIT [113, 114], and have since been demonstrated in both warm [115] and cold [116] atom vapours, as well as solid-state ensembles of rare-earth ions [117]. Although this protocol allows for particularly long storage times (reaching minutes in some systems [118, 119]) and high efficiencies upwards of 68% [107, 110], its bandwidth is limited to only a few MHz by the spectral width of the transparency window.

The storage and retrieval of broadband signals can be achieved in the off-resonant regime where $\Delta \gg \Gamma$ via optical Raman scattering [97]. In this case, the signal field is mapped onto a collective coherence of the ensemble through an off-resonant optical absorption feature generated by the application of the control field. Raman scattering consists of a two-photon process where there signal field is absorbed on the $|g\rangle \leftrightarrow |e\rangle$ and coherently transferred to $|s\rangle$ leading to the creation of a collective coherence of the ensemble also referred to as a 'spin-wave'. The width of this feature is defined by the bandwidth of the control field which allows for much greater flexibility and the storage of GHz-order fields [120]. For example, a control pulse can be shaped in order to filter temporal modes of the signal or conversely manipulate the shape of the retrieved field [53, 121]. Memory efficiencies beyond 80% have also been demonstrated using specifically tailored control pulses [122]. Fundamentally, the bandwidth of the protocol is limited by the atomic ground state splitting, as excitation with a wider pulse would simultaneously excite both transitions. In general, the efficiency of the process is bounded by a value which depends only on, and scales quadratically with, the resonant optical depth of the storage medium [112].

Although broadband single photon storage has been demonstrated with Raman quantum memories [120, 123], the photon statistics of the retrieved field are heavily deteriorated due to noise primarily caused by four-wave mixing processes [70, 124]. This mechanism is due to the control field coupling to the signal transition and generating ground state coherences which are not part of the memory interaction. This coherence leads to the detection of noisy photons at the signal frequency which cannot be easily separated from the genuine read-out signal. This phenomenon, which can even lead to gain at the signal frequency [125], has hindered the demonstration of a fully quantum Raman memory in warm atomic vapours. To a certain extent, four-wave mixing noise has been reduced by using a cavity-enhanced Raman scheme [126], or by selecting signal and control frequencies so as to introduce linear absorption loss at the anti-Stokes frequency [127].

Another class of protocols has been introduced which instead rely on ladder-type energy configurations, in part to address the issue of four-wave mixing in lambda

systems. In such a system, the three levels - a ground state $|g\rangle$, and excited state $|e\rangle$ and a doubly-excited state $|s\rangle$ - which are ordered in increasing energy as shown in Fig. 2.4. The $|g\rangle \leftrightarrow |e\rangle$ and $|e\rangle \leftrightarrow |s\rangle$ can be accessed via optical fields, and excitation of $|g\rangle$ into $|s\rangle$ can be mediated by a two-photon process. In this configuration, a single photon can be absorbed on the lower transition and stored in a coherence between the $|g\rangle$ and $|s\rangle$ states conditioned the application of a strong control field on the upper $|e\rangle \leftrightarrow |s\rangle$ control field. As was the case in a lambda-system with EIT and Raman, storage can be achieved both in the resonant or far-detuned regimes with protocols such as FLAME [128] (Fast Ladder Memory) and ORCA (off-resonant cascaded absorption) [106]. Remarkably low-noise single photon storage and retrieval was successfully demonstrated in warm Caesium vapour using the ORCA scheme, with efficiencies currently limited to $\sim 14\%$.

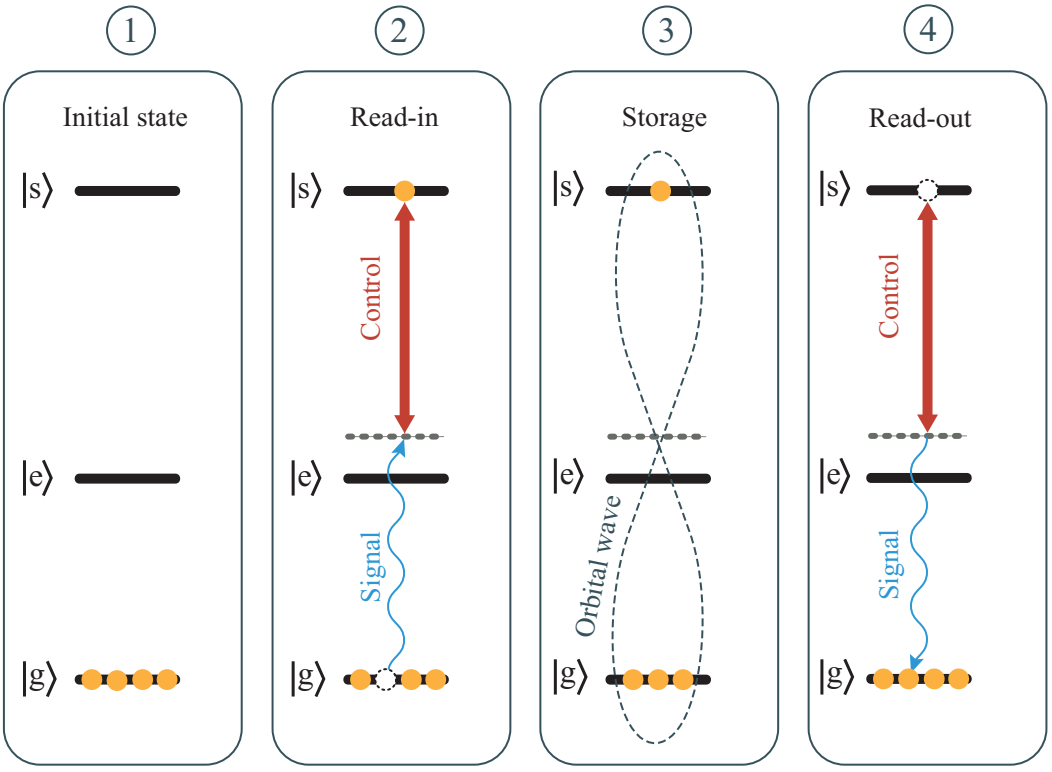

Fig. 2.4 : Schematic of the ORCA protocol. (1) An optical signal is absorbed on the $|g\rangle \leftrightarrow |e\rangle$ transition via an off-resonant two-photon absorption process enabled by the application of a strong control field on the $|e\rangle \leftrightarrow |s\rangle$ transition. (2) Through this process, the signal is coherently mapped to a collective coherence of the states $|g\rangle$ and $|s\rangle$, termed 'orbital-wave' (3) Applying the control field at a later time maps the orbital-wave back onto an optical field, prompting the retrieval of the signal photon.

Ladder configurations benefit from the absence of four-wave mixing processes as the control field does not couple to the ground state, leading to storage and retrieval interactions which are remarkably noise-free. Noise mechanisms related to imperfect optical pumping in lambda-systems are also suppressed due to the negligible occupancy of the storage state even at room temperature. Furthermore, fast repetition rates can in principle be achieved due to the relaxation of the fundamental bandwidth limit imposed by the ground-state splitting in lambda-type systems. Using such schemes, the storage and retrieval of single photons was recorded in warm atomic vapours with negligible change in photon statistics [106]. The main drawback of these schemes come from the fast decay of the doubly-excited state used for storage, leading to short memory lifetimes (5 ns in Caesium vapours and 86 ns in Rubidium). They are thus well-suited to photon synchronisation applications but currently do not satisfy the requirements of quantum repeater protocols.

2.3.2 Echo-based memories

Another subset of quantum memory protocols relies on photon-echo phenomena occurring in atomic ensembles with an inhomogeneously broadened optical transition [129]. In such a system, the emitters can be shifted away from resonance by local electromagnetic fields or Doppler effects, hereby distributing their central frequencies according to an inhomogeneously broadened profile with width Γ_{inh}. Depending on the atomic medium considered, Γ_{inh} can be orders of magnitude wider than the linewidth of each individual emitter. An optical signal in the form of a light pulse can be absorbed on such a transition and is mapped onto a collective excitation of the ensemble, where each emitter is in a superposition of the ground and excited state. The coherence of each emitter then accumulates a phase at a rate given by its resonant frequency. As the ensemble is inhomogeneously broadened, this phase is different for each atom leading to rapid dephasing of the stored excitation. However, this effect can be reversed using control techniques first developed in the context of nuclear magnetic resonance [130]. By successfully reversing the dephasing mechanism, the coherences can rephase leading to the coherent retrieval of the original signal field in a process known as a 'photon echo' [131]. Photon echoes are often used in spectroscopy experiments and implemented by applying resonant optical pulses to the ensemble. Unfortunately, this approach leads to population inversion in the ensemble which does not conserve photon statistics, and thus cannot be used to build a quantum memory [132, 133]. One approach to bypass this issue is to mute the first echo using non-phasematched pulses, as in the

ROSE (Revival of Silenced Echo) protocol [134]. Other endeavours have led to the development of schemes based on the manipulation of the inhomogeneously broadened transition itself, as presented in the following.

Some echo-based protocols such as CRIB [129, 135, 99] (Controlled Reversible Inhomogeneous Broadening) or GEM [136, 137] (Gradient Echo Memory) use an external field to broaden the transition though the Zeeman or Stark effects. This field can be controlled in order to manipulate the dephasing rate of the emitters through the broadening of the transition. In the case of CRIB, a narrow absorption feature is first created with spectral hole burning techniques which is then broadened with the help of an external field with a transverse gradient. An optical signal with a spectrum matching that of the broadened feature is then absorbed on the transition and allowed to evolve in time. The polarity of the field gradient can then be reversed at any time in order to cause a rephasing of the dipoles and retrieve the signal field. GEM consists of a similar protocol, except that the external field is applied longitudinally which prevents re-absorption of the retrieval echo and allows for typically higher efficiencies. GEM memories have been demonstrated in both rare-earth ion doped solids and warm atom ensembles with efficiencies of 69% [108] and 87% [138] respectively while typically being limited to MHz bandwidths by the achievable linewidth of the artificially broadened feature.

2.3.3 Quantum memories based on atomic frequency combs

Another promising way to realise a quantum memory in an inhomogeneously broadened medium is via the atomic frequency comb (AFC) technique [96], which will be the focus of work presented in later chapters.

Unlike CRIB and GEM, the AFC protocol does not rely on the application of external electromagnetic fields. The absorption profile of an atomic ensemble is shaped into a periodic comb-type structure made of a series of thin strongly-absorbing peaks by frequency-selective optical pumping of an inhomogeneously broadened optical transition. The atomic spectral density function then consists of a series of narrow peaks [96]. A single photon spanning many such peaks can then be absorbed on the transition. If the system is left to evolve freely, a single photon-echo will be re-emitted due to the rephasing of the atomic ensemble occurring after a time depending on the characteristics of the comb [139]. Until this point, the protocol only enacts a photonic delay line, in the sense that the read-out time is predetermined. However, in a well-chosen system, it is often possible to map the excitation onto a long-lived ground state, freezing the

phase evolution of the process and effectively enacting an on-demand quantum memory [96].

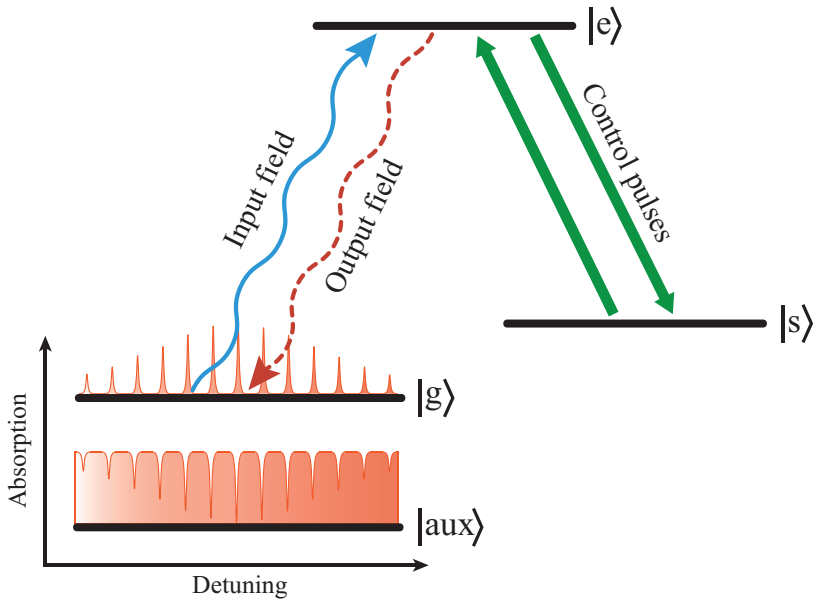

Fig. 2.5 : Illustration of the AFC quantum memory protocol. The inhomogeneously broadened profile of the $|g\rangle$ - $|e\rangle$ transition is shaped into an atomic frequency comb using spectral hole burning techniques. After absorption of the input field, application of control fields allow the storage of the excitation by freezing the dephasing processes inside a long-lived ground state coherence.

Ideally, the storage medium is an inhomogeneously broadened ensemble of atomic emitters with three ground states $|g\rangle$, $|s\rangle$, and $|aux\rangle$, all optically coupled to a single excited state $|e\rangle$. The inhomogeneous broadening must also be much wider than the homogeneous linewidth of the emitters. The first step of the process consists in the creation of periodic absorption peaks on the $|g\rangle$ - $|e\rangle$ transition (the so-called atomic frequency comb) using optical pumping and spectral hole burning techniques, i.e. emitters sitting at well-defined frequencies are pumped into an auxiliary level $|aux\rangle$. The resulting absorption profile is then that described in Fig. 2.5, with the atomic spectral density given by

$$g(\delta) \propto e^{-\delta^2/4\Gamma^2} \sum_{j=-\infty}^{\infty} e^{-(\delta - j\Delta)^2/4\gamma^2}, \tag{2.2}$$

that is, a series of Gaussian peaks with individual width γ separated by a frequency interval Δ. Γ is defined as the overall spectral width and δ the detuning from resonance. This is the so-called 'atomic frequency comb' [96]. Note that scheme does not prescribe

any particular profile of the AFC peaks. In Ref. [96], Afzelius *et al.* opt for Gaussians to simplify the analysis, and this assumption underpins Eq. 2.7. However, square-shaped teeth have been shown [140] to lead to higher efficiencies.

A single photon of spectral width γ_p satisfying $\Delta \ll \gamma_p \leq \Gamma$ can then be absorbed into the medium. This single excitation is delocalised over all N atoms within the storage medium and can be described as a Dicke state [141] given by

$$|\psi\rangle = \sum_{i=1}^{N} c_i e^{i\delta_i t} e^{-ikz_i} |g_1 ... e_i ... g_N\rangle \,. \tag{2.3}$$

Here, z_i and δ_i are the position and detunings of the ith atom, k the light wavenumber and the c_is a set of atom-dependent amplitudes. Due to the AFC profile, provided the comb has narrow peaks, the atomic detunings can be approximated as $\delta_i = m_i\Delta$ with integer m_i. This fixed phase relationship between the dipoles leads to the emission of a rephasing echo at $\tau = 2\pi/\Delta$ when all the atoms oscillate in phase again.

The full AFC protocol includes control pulses in order to transfer the excitation towards a long-lived storage state $|s\rangle$. The dephasing of the collective excitation is then effectively frozen for the duration of the storage. The stored excitation, or spin-wave [97], can be subsequently read-out by applying a second control pulse after a time T_S. By using this technique, not only can the storage time of the memory protocol be extended to $\tau + T_S$, but also the read-out timing can be chosen at will which is requirement in most quantum information processing schemes. The typical pulse sequence for the realisation of such a scheme is shown in Fig. 2.6.

A more rigorous treatment of this phenomenon can be found in Ref. [96] which employs the Maxwell-Bloch equations. For the two-level echo scheme, these are given by

$$\frac{\partial}{\partial t}\sigma(z,t;\delta) = -i\delta\sigma(z,t;\delta) + i\mu_{ge}^2 E(z,t) \tag{2.4}$$

$$\left(\frac{\partial}{\partial t} + c\frac{\partial}{\partial t}\right) E(z,t) = i\mu_{ge}\int_{-\infty}^{\infty} g(\delta)\sigma(z,t;\delta)d\delta, \tag{2.5}$$

where σ is the atomic polarization, the mean coherence of atoms at detuning δ and μ_{ge} is the dipole moment for the transition. These expressions, written for the case of a two-level system, describe the effect of a light pulse travelling through a material on the coherence of the atoms composing it. Substituting the atomic spectral distribution

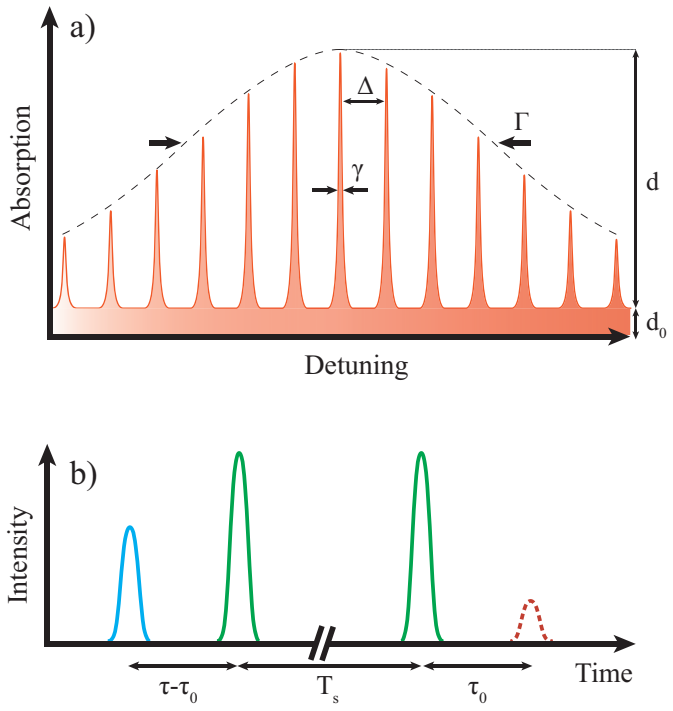

Fig. 2.6 : Details of the AFC protocol. (a) Spectral structure of an atomic frequency comb with total width Γ, peak separation Δ, and individual peak width γ. The comb has an optical depth d and d_0 refers to any remaining absorbing background. The dashed line refers to the shape of the original inhomogeneously broadened profile. (b) Pulse sequence for the AFC protocol with spin-wave storage. The signal (blue) is absorbed at $t = 0$. A control pulse can be applied after a time $\tau - \tau_0$, where $\tau = 2\pi/\Delta$ is the AFC echo rephasing time. The control pulse freezes the dephasing process for a time T_S until another control pulse is applied. The stored field is then recovered via a rephasing echo after a time τ_0.

$g(\delta)$ above and solving for the re-emitted field readily yields the expression below:

$$E_{out} = -E_{in} e^{-(\pi^2/4\ln 2F^2)} \tilde{d} e^{-\tilde{d}/2}, \tag{2.6}$$

where $F = \Delta/\gamma$ is the finesse of the AFC and $\tilde{d} = d/F$ is the optical depth experienced by the pulse for a material of full optical depth d at the relevant wavelength. An analytical expression for the efficiency of the process can then be derived to be

$$\eta = \frac{|E_{out}^2|}{|E_{in}^2|} \approx \tilde{d}^2 e^{-7/F^2} e^{-\tilde{d}} e^{-\tilde{d}_0}, \tag{2.7}$$

d_0 representing an absorbing background, i.e. comb troughs not reaching full transparency. This analysis implies that much care must go into the preparation of the AFC

in order to reach high efficiency values. In particular, there is an inherent tradeoff in increasing the finesse which also often implies reducing the optical depth of the comb. Furthermore, while the second factor in Eq. 2.7 benefits from higher values of F, the first does not. Applying optimisation techniques to tailor the shape of the AFC is a key factor in increasing the performance of the memory interaction, as shown in Ref. [140].

The beauty of this protocol is that the application of the control is resonant, thus avoiding four-wave mixing noise phenomena, and temporally separated from the signal emission, allowing the use of efficient time-domain filtering. It is also interesting to note that the full AFC protocol (with spin-wave storage) offers the possibility of retrieving the excitation by applying a counter-propagating control field, which has been shown theoretically [96] to significantly increase the maximum efficiency of the memory due to reduced re-absorption in the medium.

Another advantage of the AFC method is its multimode capacity [95]. Unlike many other quantum memory protocols, the number of modes one can store in the medium of interest is not limited by the optical depth of the material [96]. Indeed, it only depends on the number of peaks in the atomic frequency comb. One way of seeing this is that the number of modes N one can store using this method is proportional to τ_{AFC}/τ_p, i.e. the ratio between the storage time and the pulse duration. However, as the optimal pulse duration has a spectral width matching that of the comb, $\tau_p \sim 2\pi/\Gamma$ and since $\tau_{AFC} = 2\pi/\Delta$, the accepted number of modes follows $N \propto \Gamma/\Delta$ which is just the number of AFC peaks.

Rare-earth ion doped solids, characterised by narrow homogeneous and wide inhomogeneous linewidths, are a natural platform for the implementation of the AFC protocol [142–144]. Fully quantum AFC spin-wave memories were first demonstrated simultaneously in Pr:YSO and Eu:YSO with weak coherent pulses [145, 146] and then in Pr:YSO with single photons [46]. The efficiency of the spin-wave AFC protocol is currently limited to $\sim 4\%$ by the quality of the comb as well as the optical depth of the ensemble. While the bandwidth of the AFC technique itself is only defined by that of the comb profile, the maximal acceptance bandwidth of the spin-wave storage protocol is fundamentally defined by the ground state splitting of the chosen atomic system. This splitting is relatively small in many rare-earth ions ($\sim$MHz in praseodymium for example), limiting the repetition rate of experiments as well as making the protocol currently compatible with a small number of narrowband single photon sources [72]. Recently, alternative on-demand AFC memory schemes relying on electric field pulses [147] have emerged, with initial results demonstrating higher efficiencies $\sim 38\%$.

2.4 Summary

In this chapter, we have introduced the topic of quantum memories and provided an overview of why they are a highly desirable device for optical quantum information processing. A focus was made on the use of atomic ensembles as a storage medium. Some of the more common memory protocols were briefly presented in the light of performance criteria desirable for different applications. A quantum memory scheme based on atomic frequency combs is highlighted as a particularly promising approach in inhomogeneously broadened systems. In the following chapters we will report on some work aiming to improve experimental realisations of the AFC protocol in solid-state platforms.

Chapter 3

Rare-earth ion doped solids

This chapter aims to briefly introduce rare-earth ion (REI) doped solids, a promising platform for the implementation of efficient light-matter interaction protocols. We will discuss the particular example of Praseodymium ions doped into an Yttrium Orthosilicate crystal (Pr^{3+}:Y_2SiO_5 or Pr:YSO), which was used in all the experiments involving REIs presented in this thesis. In order to provide an insight into the dynamics of this system, a focus will be made on how the optical and spectral properties of Pr^{3+}:Y_2SiO_5 arise from the electronic structure of the Praseodymium ion and its interaction with the host lattice.

3.1 Electronic structure

Rare-earth metals refer to group of elements including the Lanthanide series with atomic numbers ranging from 57 (Lanthanum) to 71 (Lutetium), which are particular for having a partially full $4f$ electronic shell within full $5s$ and $5p$ orbitals. The ions' trivalent (e.g. Pr^{3+}) oxidation state is the most common and is generally achieved through ionisation of two electrons in shells of quantum number higher than $5p$, and one $4f$ electron. In the case of Praseodymium, the $4f$ electrons are spatially closer to the nucleus than those in the filled $5s$ and $5p$ as shown in Fig. 3.1. As a result, the outer orbitals provide a partial Faraday cage that shields the $4f$ electrons from external electric fields. This property guarantees that the energy level structure rare-earth ions doped into a solid-state lattice remains relatively similar to the free space case. This screening effect also allows for remarkably narrow $4f$-$4f$ transitions making REIs an attractive platform for solid-state optical devices.

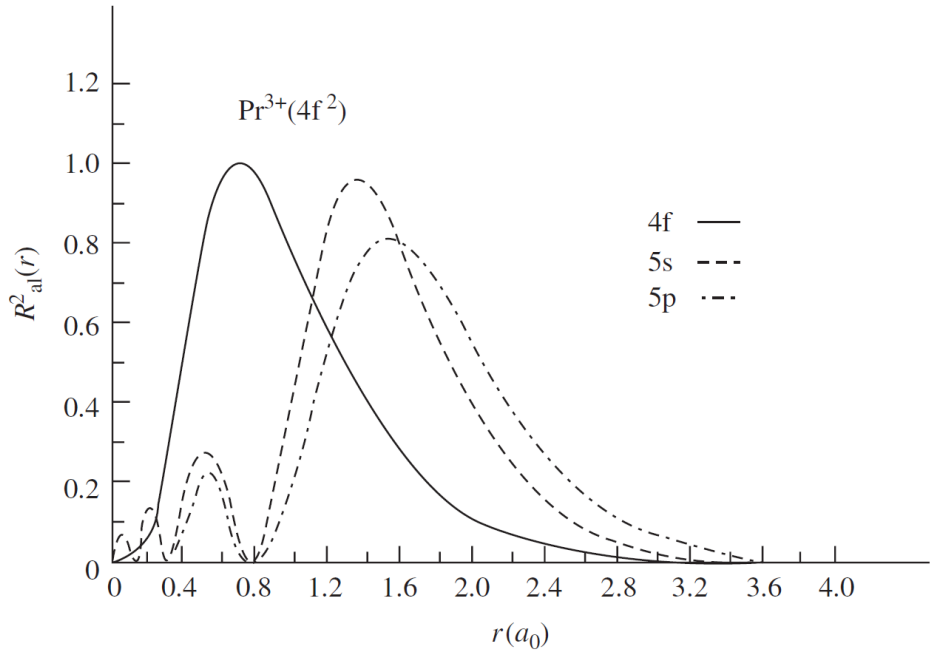

Fig. 3.1 : Radial distribution of different electronic orbitals for the Pr^{3+} ion. (Adapted from [148])

3.2 Energy levels

The electrically isolated nature of the $4f$ electrons implies that the influence of the external fields, such as that exerted by a host crystal lattice in a REI doped sample, can be treated as a perturbation to the free-ion case. The full Hamiltonian of Pr^{3+}:Y_2SiO_5 is then composed of a set of terms:

$$\mathrm{H} = \mathrm{H}_0 + \mathrm{H}_C + \mathrm{H}_{SO} + \mathrm{H}_{CF} + \mathrm{H}_{HF} + \mathrm{H}_Q + \mathrm{H}_{NZ} + \mathrm{H}_{EZ}, \tag{3.1}$$

each describing a different physical effect defining the energy level structure of the system, outlined in Fig. 3.2. In the following, we will only briefly describe each of these terms but more detail is readily available in reference [149]. Similarly, the the full energy level structure of Pr^{3+}:Y_2SiO_5 can be found in reference [150].

H_0 accounts for the potential and kinetic energy of the electrons in the field of the nucleus and due to its spherical symmetry does not shift the energy levels. The Coulomb repulsion between the electrons, represented by H_C, does lift the degeneracy of the $4f$ shell and leads to the emergence of ground and excited states. The splitting is of hundreds of terahertz ($\sim$494 THz in Pr^{3+}), and hence the resulting transitions can be accessed with optical frequencies.

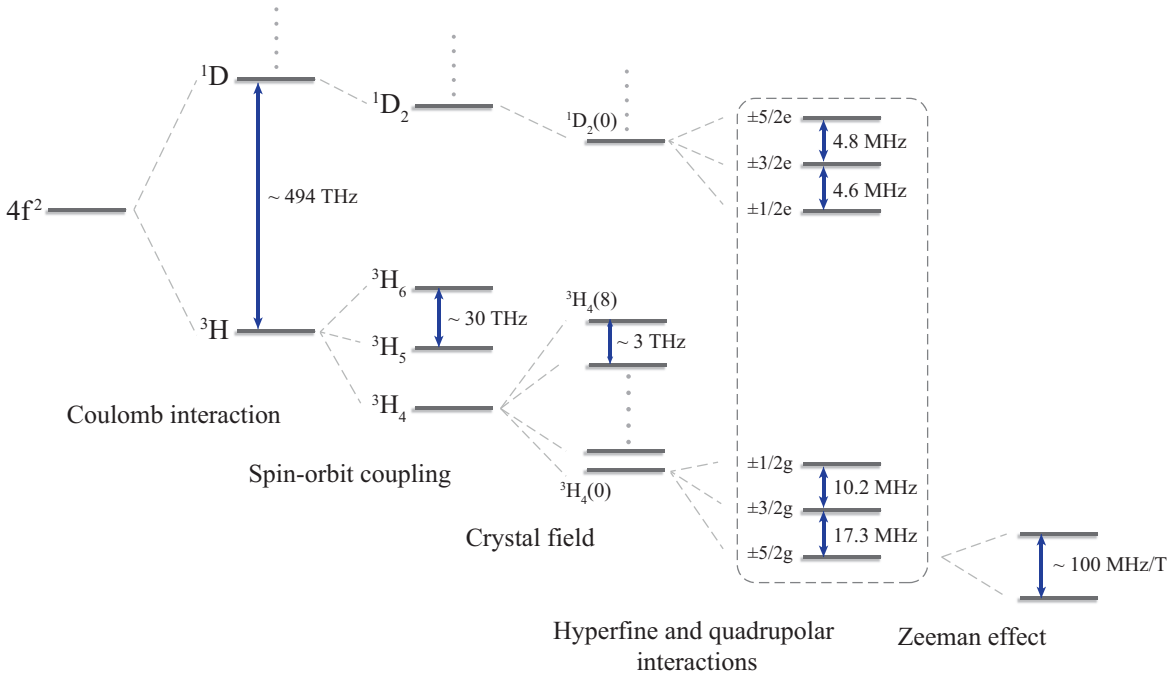

Fig. 3.2 : Typical energy level structure of rare-earth ions in solids, along with the splittings induced by the interaction with local electromagnetic fields, shown for the example of Pr^{3+}:Y_2SiO_5.

H_{SO} refers to the spin-orbit coupling, where the magnetic field generated by the electrons' orbit around the nucleus interacts with the electron spins. This term leads to another set of spectral terms split by tens of terahertz which are labeled $^{2S+1}L_J$ where S is the net electronic spin, J the total angular momentum and L the total orbital quantum number. Hence, according to this notation, the ground state of Praseodymium is $^3H_4$.

The electric field of the host crystal also affects the energy structure of the system and is accounted for by H_{CF}. Depending on whether the ion has an even or odd number of electrons and the crystal's site symmetry, the levels can be further split into a maximum of 2J+1 additional levels with typical separations of $0.1 - 1$ THz. The relevance of the atomic state labelling is preserved by these splittings being of considerably smaller magnitude than those induced by spin-orbit coupling. The additional levels which emerge in presence of the crystal field are simply noted $^{2S+1}L_J(n)$ with n ranging from 0 to 2J.

H_{HF} represents the hyperfine coupling between the nuclear spin and the magnetic field generated by the electronic angular momentum. In the case of Pr^{3+}:Y_2SiO_5, the hyperfine term vanishes to first order and is often treated jointly with H_Q, the electric

quadrupole interaction between the nuclear quadrupole moment and the electric field gradient at the nucleus generated by the surrounding charges [149]. This effective hyperfine interaction splits each crystal field singlet into three doubly degenerate levels labeled $\pm 5/2$, $\pm 3/2$, and $\pm 1/2$ by convention.

Finally, the degeneracy between pairs of hyperfine states can be lifted by the application of an external magnetic field. This interaction is accounted for by the electronic and nuclear Zeeman terms H_{EZ} and H_{NZ}. The splitting is directly proportional to the magnitude of the field, and recorded to be of approximately 100 MHz/T in Pr^{3+}:Y_2SiO_5 [151].

3.3 Broadening mechanisms

Having elucidated the fundamental mechanisms defining the typical energy level structure of most REI doped solids, we can now look at the environmental phenomena limiting the lifetime of the electronic states. The spectral linewidth of a single ion's absorption and emission profile is defined by

$$\Gamma_h = \frac{1}{2T_1} + \frac{1}{T_2} = \frac{1}{T_2^*} \tag{3.2}$$

where T_1 represents population decay, T_2 pure dephasing and T_2^* the overall decoherence time.

The splittings between individual crystal field levels are of comparable scale to phonon energies in the host crystal lattice, and hence ion-phonon interactions lead to rapid decay of population to the lower crystal field levels and subsequent broadening of the transitions. Elastic Raman scattering events can also cause dephasing of the electronic state and reduce the ion's coherence time. In order to reduce the magnitude of these effects, experiments are often run at temperatures below 6K where phonon contributions are minimised [152]. Furthermore, transitions linking the lowest crystal field states are often chosen in order to avoid phonon-mediated decay.

At low temperatures, the homogeneous linewidth of REIs is limited by spin-spin interactions with elements in the host lattice or simply other REIs. For example, the excitation of one ion may cause fluctuations in the electromagnetic environment of another ion nearby leading to spectral diffusion[153]. In general, interactions between REIs are highly dependent on the distance between the ions and hence reducing the dopant concentration is enough to mitigate this effect. Fluctuations in nearby nuclear

spins result in the rare-earth ion experiencing a time-dependent magnetic field and thus loss of coherence. The zero first-order Zeeman (ZEFOZ) technique [154] has been successful in reducing the REI's sensitivity to ambient magnetic fields and allowed the observation of long spin coherence times[155]. In general, host materials with low nuclear magnetic moments such as YSO are also chosen in order to further minimise host-ion interactions. At low temperatures and given the right environment, rare-earth ions can exhibit particularly narrow homogeneous linewidths [156] which contributes to their attractiveness as quantum optical devices.

However, in practice, the full linewidth of a crystal doped with an ensemble of rare-earth ions is orders of magnitude wider than that which would be expected from homogeneous broadening alone. Indeed, each ion experiences a slightly different environment due to the anisotropicity of the crystal field, strain in the crystal or the presence of chemical impurities in the sample and as a result their resonance frequencies can be shifted from each other. When probing the ensemble as a whole, the overall absorption line can then be much larger than the individual narrow linewidths. This is known as the inhomogeneously broadened linewidth Γ_{inh} and depends notably on the doping concentration of the crystal. Hence, for ensembles of ions the full coherence time can be expressed as

$$\Gamma_{tot} = \frac{1}{T_2*} = \frac{1}{2T_1} + \frac{1}{T_2} + \frac{1}{T_{2'}} \tag{3.3}$$

where $\frac{1}{T_{2'}} = 1/\Gamma_{inh}$ corresponds to the contribution from inhomogeneous effects.

Since the inhomogeneous line is much wider than the hyperfine splitting, a single optical frequency can simultaneously excite all of the transitions. As a result, gaining access to the homogeneous linewidth of the ions, be it for spectroscopy or quantum information storage, requires the use of coherence rephasing techniques [131, 157]. This issue is often tackled using techniques such as spectral hole burning which allow optical manipulation of the inhomogeneous ensemble.

3.4 Spectral hole burning in Pr^{3+}:Y_2SiO_5

The main optical transition of interest in Pr^{3+}:Y_2SiO_5 links the lowest-lying crystal field levels of the $^3H_4$ and $^1D_2$ manifolds. This transition is only weakly allowed and has a relatively low dipole moment of 3.7×10^{-32} C.m [135] (compared to 3.58×10^{-29} C.m for the Rubidium D_2 line [158]). Praseodymium ions can replace Y^{3+} ions at

two possible sites in YSO, simply known as sites 1 and 2[159]. The crystal field shift experienced by Pr^{3+} ions in each site varies slightly leading to two spectroscopically distinguishable $^3H_4(0) \leftrightarrow {}^1D_2(0)$ transitions at 606 nm and 608 nm for sites 1 and 2 respectively. All experiments in this thesis are run on site 1 ions due to larger population offering a transition with a higher optical depth. The host crystal, Y_2SiO_5, is characterised by three mutually perpendicular axes noted b, D_1 and D_2 defined by the crystal birefringence [149, 160]. Light resonant with the transition is maximally absorbed when its polarisation is aligned to the D_2 axis.

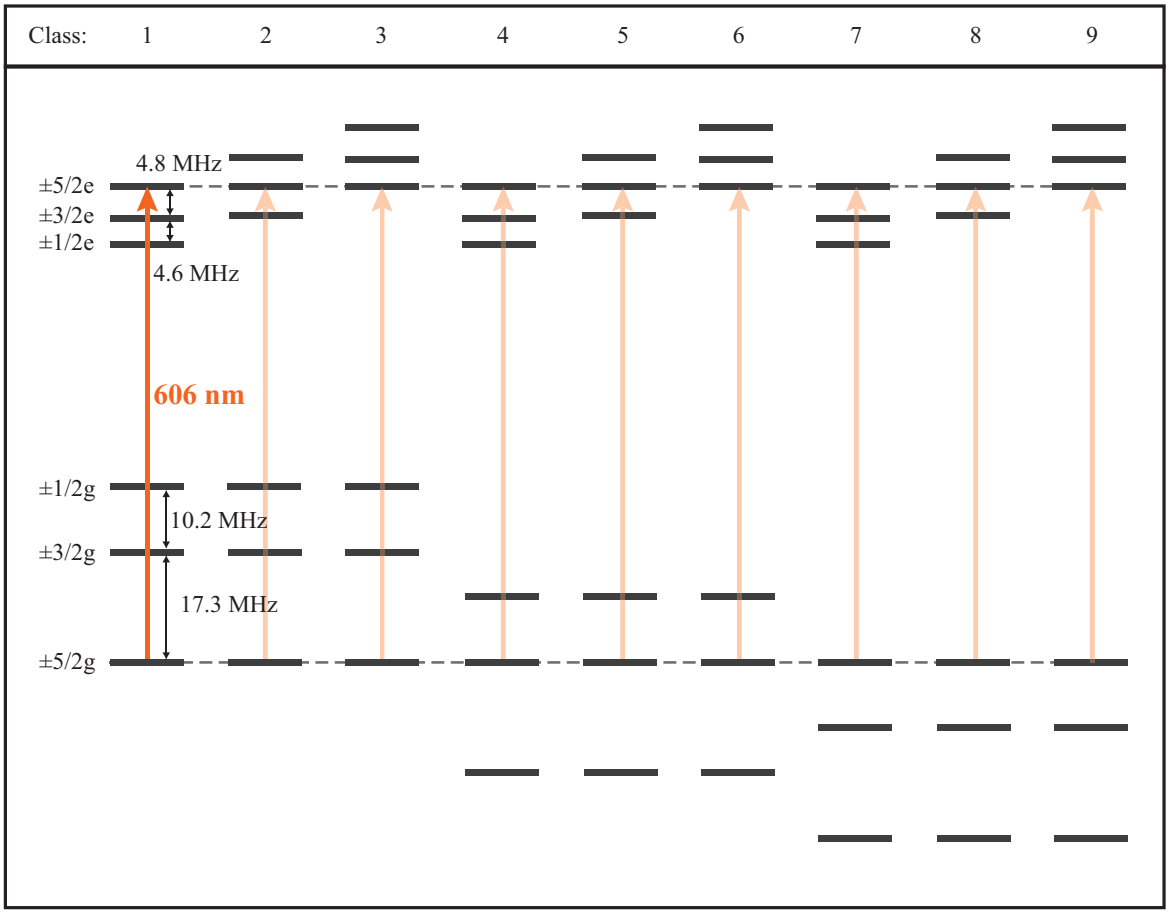

Fig. 3.3 : Diagram showing the hyperfine level structure of the $^3H_4(0)$ and $^1D_2(0)$ states in Pr^{3+}:Y_2SiO_5, along with the 9 classes of ions within an ensemble which can interact with a single narrowband optical field.

The $^3H_4(0) \leftrightarrow {}^1D_2(0)$ zero-phonon line in Pr^{3+}:Y_2SiO_5 is a narrow transition, with an optical decay T_1 of 160 μs and a reported decoherence time T_2 of 111 μs at 4K and zero magnetic field[159]. As mentioned previously, the ground and excited states are both split into three hyperfine levels which are separated by 4 to 17 MHz

(see Fig. 3.3). The ground states can be extremely long lived, with $T_1 > 1$ min and $T_2 \sim 500\,\mu$s[161, 162]. The subsequent 9 possible transitions are all weakly allowed, with varying oscillator strengths detailed in Table 3.1 [135]. The $^3H_4(0) \leftrightarrow {}^1D_2(0)$ transition is also inhomogeneously broadened by typically of $1 - 10$ GHz dependent on the Pr^{3+} doping concentration. We recorded a 9 GHz linewidth with a 0.05% doping level.

As the inhomogeneous broadening is many orders of magnitude wider than the homogeneous line, a single optical frequency can simultaneously be resonant with nine groups (known as classes) of atoms whose transitions are shifted with respect to each other as shown in Fig. 3.3. As a result, optical control of the ensemble can be challenging and requires careful consideration of which ions are being addressed.

g/e	$\pm 1/2$	$\pm 3/2$	$\pm 5/2$
$\pm 1/2$	0.55	0.38	0.07
$\pm 3/2$	0.4	0.60	0.01
$\pm 5/2$	0.05	0.02	0.93

Table 3.1 : Relative oscillator strengths of the transitions between the hyperfine states of the ground $^3H_4(0)$ and excited $^1D_2(0)$ manifolds, sourced from Ref. [135]

Pr^{3+}:Y_2SiO_5 is a material which can benefit from the application of spectral hole burning, whereby the spectral profile of an ensemble is manipulated via optical pumping. Indeed, the long lifetimes of the hyperfine ground states allow the construction of durable spectral structures, such as atomic frequency combs (see section 2.3.3) within the inhomogeneously broadened line. If a single class is considered, the application of a long enough pulse in resonance with one of the transitions will empty one of the hyperfine ground states of population, which will be redistributed to the neighbouring levels. Spectrally, this leads to the appearance of a narrow window of transparency (or *hole*) at the excitation frequency and two associated troughs corresponding to the transitions linking the now emptied-out state to the two other excited hyperfine states. Due to population conservation, six enhanced absorption features (or *anti-holes*) will also be observable, corresponding to the two states with increased population. Of course, when taking all nine classes into account, the spectral structures can become considerably more complex and can be found in more detail in Ref. [135], and is shown in Fig. 3.4 below.

Note that in Pr^{3+}:Y_2SiO_5, the maximum possible width of a transparent hole, or 'spectral pit', is limited to 18.1 MHz [163] by the hyperfine structure of the ion, as

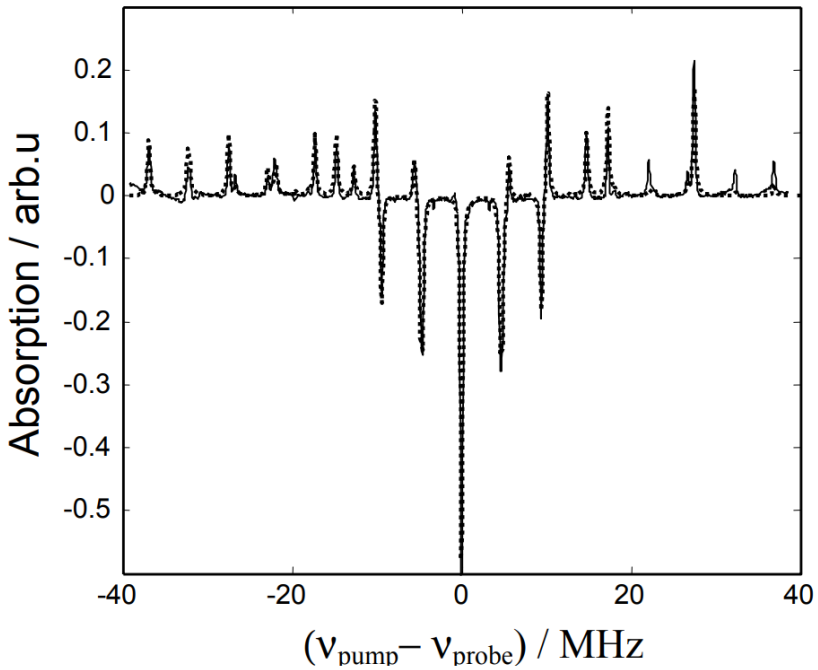

Fig. 3.4 : Experimental trace (solid line) and simulation (dashed line) of the hole-burning spectrum of the ${}^3H_4 - {}^1D_2$ transition in Pr^{3+}:Y_2SiO_5. Figure from Ref. [135].

beyond that population is re-pumped into the hole. This value is defined by the total separation of the hyperfine ground states (27.5 MHz) reduced by the total separation of the excited state levels (9.4 MHz). Such a feature can be created by sweeping a narrowband laser across a desired frequency interval. Using similar techniques, the spectral density of an inhomogeneously broadened ensemble can be shaped into structures such as atomic frequency combs (see section 2.3.3). Atomic frequency combs can then be used to implement quantum memory protocols in the system. Spectral hole burning is a cornerstone of many experiments involving Pr^{3+}:Y_2SiO_5 [164, 165] and will be the focus of results presented in the following section.

Chapter 4

Light-matter interactions for broadband quantum memories in Pr^{3+}:Y_2SiO_5

In this chapter, we present experimental results obtained using ensembles of praseodymium ions doped in an yttrium orthosilicate host crystal. The first part (4.1) focuses on a new technique for engineering broadband atomic frequency combs in Pr^{3+}:Y_2SiO_5. We first describe the experimental setup before providing a summary of the outcome of the measurements accompanied by an evaluation of the advantages and limitations of the method. This discussion leads to the description of a scheme for the realisation of a ladder-type quantum memory in Pr^{3+}:Y_2SiO_5, which is the main subject of the second part. In section 4.2, we present the results of experiments investigating the feasibility of such a device, in particular studying the two-photon $^3H_4(0) \leftrightarrow ^3 F_3(0) \leftrightarrow ^1D_2(0)$ transition. All experiments in this chapter we performed by myself with the assistance of J. N. Becker and P. M. Ledingham, and simulations were performed by myself.

4.1 Atomic frequency comb storage of broadband light pulses in Pr^{3+}:Y_2SiO_5

Pr^{3+}:Y_2SiO_5 is well-known to be a platform of choice for the implementation of the atomic frequency comb quantum memory protocol [96, 164] - see section 2.3.3. In-depth understanding of its properties has led to many exciting results including one of the first demonstrations of single photons storage in a solid-state quantum memory with

on-demand readout [46]. As the properties of the memory depend immensely on the exact profile of the comb structure, developing further spectral hole burning techniques is crucial in order to tailor the system to any desired application [140].

Traditionally, the AFC profile is constructed within the ensemble by carefully sweeping a narrowband laser across the inhomogeneous line [144, 145]. A window of transparency (or 'spectral pit') is first prepared via spectral hole burning. Ions are then selectively pumped back into the pit at specific detunings in order to generate the "teeth" of the comb profile. Hence, careful control of the burning laser is necessary to obtain a comb with high optical depth contrast between the spectral peaks and troughs. The width of this AFC structure is bounded to a few MHz by the hyperfine ground state splitting, limiting the acceptance bandwidth of the photon to be absorbed. In this work, we introduce a simple method allowing the generation of broadband GHz-wide atomic frequency combs in Pr^{3+}:Y_2SiO_5.

4.1.1 Concept

Consider an inhomogeneously broadened atomic ensemble with a lambda-type electronic structure. A narrowband laser can imprint a spectral hole within the inhomogeneously broadened line by pumping population into one of the two ground states. A pulse train in time corresponds to a set of evenly spaced narrow peaks in the spectral domain. Hence, given a large enough ground state splitting, an atomic frequency comb can in principle be generated with a single pulsed laser.

In this section, we apply this idea to Pr^{3+}:Y_2SiO_5 in order to produce a broadband AFC. However, Pr:YSO is a complex system, with three ground and excited hyperfine states leading to a total of nine optical transitions. Furthermore, as the inhomogeneous broadening is much wider than the hyperfine state splittings, a single frequency addresses up to nine classes of atoms. As a result, optically pumping the ensemble with narrowband light leads to a intricate spectral structure with many holes and anti-holes [161]. Applying a resonant train of short pulses to the system is equivalent to pumping it with an optical frequency comb. The aim of this experiment is to show that a periodic spectral structure can be engineered within an ensemble of praseodymium ions using a frequency comb, despite its hyperfine structure. We then implement the basic AFC light storage protocol using this technique and discuss its advantages and limitations in the context of solid-state quantum memories.

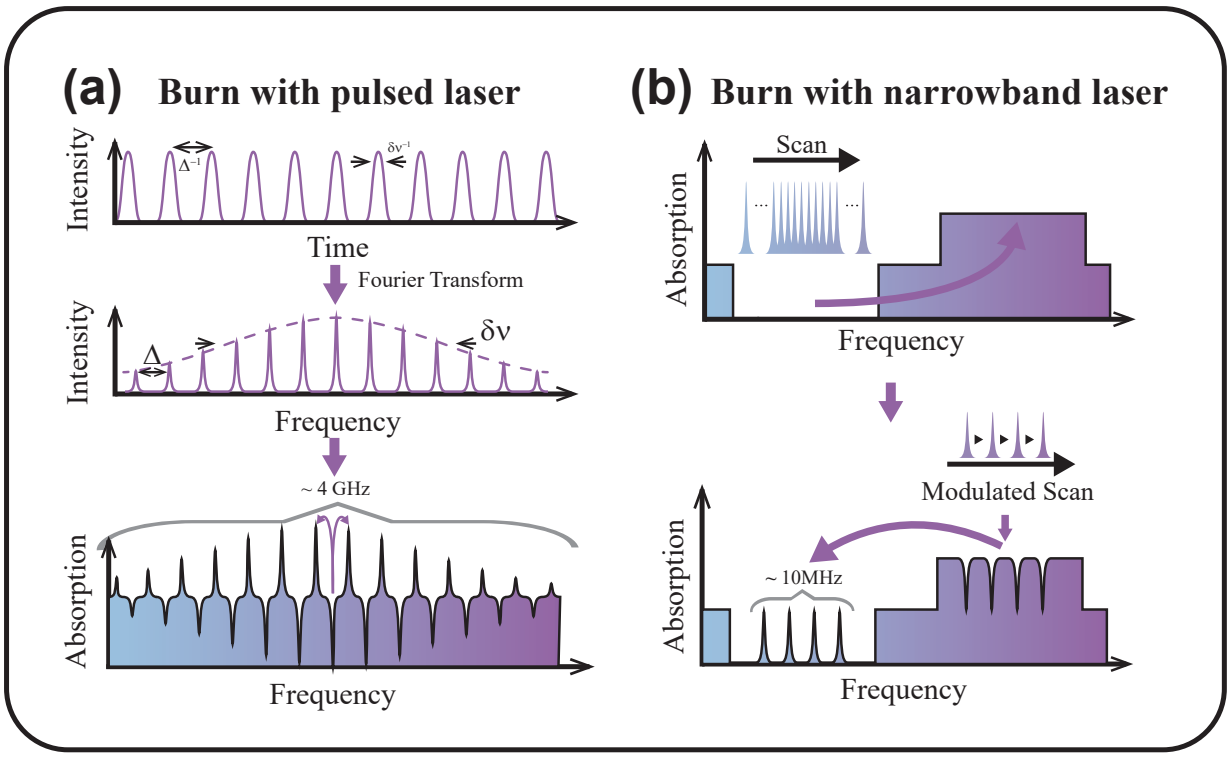

Fig. 4.1 : Diagram comparing broadband and narrowband AFC spectral hole burning techniques. We prepare a broadband AFC (a) by the direct application of an optical frequency comb generated by a pulsed laser. (b) The conventional narrowband AFC preparation is achieved first by the creation of a transparency window followed by selective repumping with a narrowband laser.

4.1.2 Experimental setup

The experimental setup necessary in order to investigate the hole burning technique described above is composed of three main elements. We distinguish a stage used for the preparation of the optical fields required in the experiment, the cryostat containing the Pr^{3+}:Y_2SiO_5 sample and a section where the light transmitted through the setup is collected and analysed.

Light Sources

All the optical fields used in this experiment are generated by a synchronously pumped pulsed dye-laser system (Sirah Gropius). The laser outputs a train of 70ps-long pulses broadly tuneable in the 575-620 nm range using Rhodamine 6G in ethylene glycol as a gain medium, allowing the $^3H_4(0) \leftrightarrow {}^1D_2(0)$ transition at 606 nm to be addressed

resonantly. The dye is pumped by 3ps-long pulses from an Ytterbium-doped fibre laser (NKT AeroPULSE PS) converted to 516 nm by an optical frequency doubling stage (APE Emerald Engine) produced at a repetition rate of 80 MHz. Pulses produced by the dye laser itself are also spaced in time by 12.5 ns and have an average power of up to 120 mW. The laser output can be tuned in steps of ~ 1 GHz via a birefringent filter and a thin etalon placed inside the cavity. In the frequency domain, the spectrum of the pulse train is a frequency comb with a 4 GHz envelope and peaks separated by 80 MHz. The width of the peaks in the frequency comb is limited to ~ 40 MHz by rapid fluctuations in the laser spectrum mainly caused by instability in the dye jet.

The excitation setup is detailed in Fig. 4.2 below. The laser output is first split into a strong and a weak beam. The first we refer to as *pump* or *burn* and will be used for spectral hole burning. The remaining attenuated beam serves to probe the absorption profile of the ensemble. Both arms of the setup can be switched on or off by mechanical shutters attached to servomotors and electronically controlled by an Arduino setup. The laser first passes through an acousto-optic modulator (AOM) which is used in double-pass configuration and driven by an external radio frequency (RF) generator. The light from the first diffracted order of an AOM is spectrally shifted by a value equal to the modulation frequency. We can modulate the frequency of the RF signal driving the AOM by 40 MHz at a rate of 10 kHz using an arbitrary waveform generator. In effect, this sweeps the laser by 80 MHz at a 10 kHz rate, washing out the frequency comb structure and resulting in a smoother spectral profile.

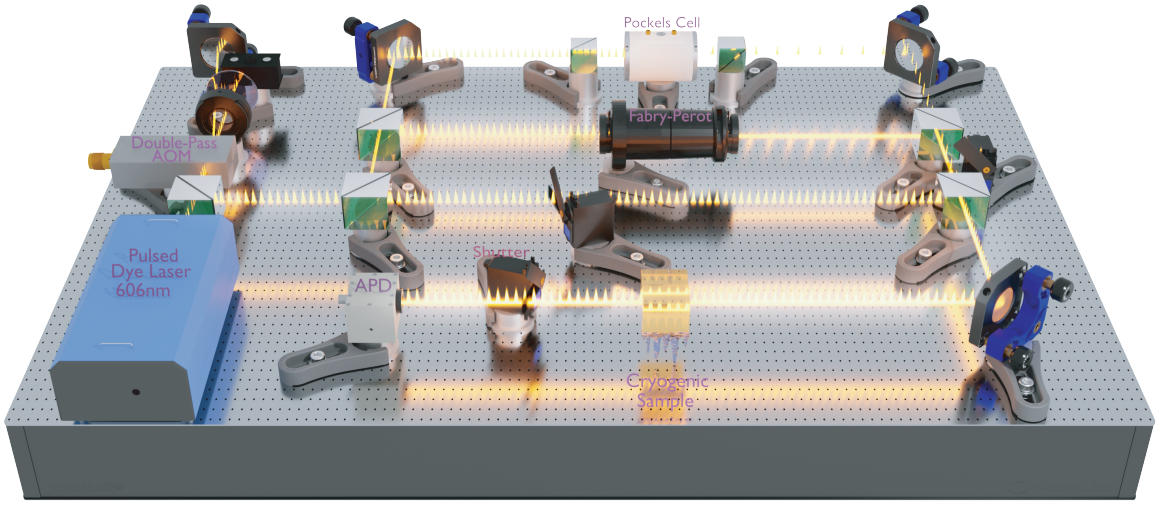

Fig. 4.2 : Optical setup used to prepare and probe a broadband atomic frequency comb in Pr^{3+}:Y_2SiO_5. Figure courtesy of J. N. Becker.

This preparatory step is necessary in order to generate the probe beam. A small portion of this beam is picked off using a half-wave plate and a polarising beamsplitter to form a train of weak coherent pulses. It then passes through an SFPI where the cavity length is swept according to a sawtooth signal provided by a Toptica SC110 high-voltage scanning module. The SFPI filters the input signal down to a narrowband optical probe with a frequency depending on the interferometer cavity length. Furthermore, as the pulses are initially spectrally broader than the SFPI free spectral range, the signal has to be initially filtered using a thin monolithic etalon with 1 GHz bandwidth. The output of the SFPI is then limited to 7.5 MHz by the cavity finesse with a scanning range of 1.5 GHz. This setup allows us to perform spectroscopy on the transition without resorting to a narrowband diode laser which was not readily available at the transition wavelength.

A pulse-picking setup is also installed in the probe arm, and is accessible via a set of flip-mirrors. The ability ot select single pulses form the laser is necessary in order to generate the read-in signal for the memory protocol, where a single weak classical pulse is resonantly absorbed by the atomic ensemble. This stage consists of a Pockels cell (Leysop Ltd. cell with BME switching electronics) placed between two Glan-Taylor prisms. The first prism is aligned to the input polarisation of the cell, and the second is set such that all incoming light is blocked while the Pockels cell is off. Applying a high voltage to the cell rotates the polarisation of the incoming beam with a $\sim$1 ns rise time allowing light to pass through the second polariser. The cell is controlled by an electronic signal provided by a Stanford DG635 delay generator. The DG635 is synchronised to the incoming laser pulse with a trigger signal from a fast photodiode collecting light picked off from the 516 nm Emerald Engine fibre laser used to pump the dye laser system. This setup allows pulses to be picked at maximum rate of 10 kHz from the 80 MHz input pulse train with an extinction ratio of approximately 1:2000 without spatial filtering via fibre coupling.

The pump beam is simply the unfiltered AOM output. Since the spectral blurring effect conferred by the AOM can be gated on or off electronically, the beam has two distinct modes of operation. The bare laser is used for spectral hole burning on the inhomogeneous line. The beam with the AOM active is used to optically pump all classes and populations in the ensemble equally and thus reset the system to its equilibrium state. The pump and probe beams are then recombined and sent directly to the sample via optical fibre.

Cryostat and sample

For the course of the experiment, we use a 3 mm long Pr^{3+}:Y_2SiO_5 with a 0.05% doping concentration of praseodymium. The relevant transition connecting the $^3H_4(0)$ ground and $^1D_2(0)$ excited states was detected at 605.977 nm. Its absorption profile is shown in Fig. 4.3, corrected for the width of the weak pulses from the Gropius system used as a probe. The blue curve corresponds to the maximally absorbed polarisation, which occurs when it is aligned to the D_2 axis of the crystal, and the red curve to the minimally absorbed polarisation. We measure a inhomogeneous transition width $\Gamma_{inh} \sim 9$ GHz with an optical depth $d_{max} = 3$, accounting for the linewidth of the probe laser.

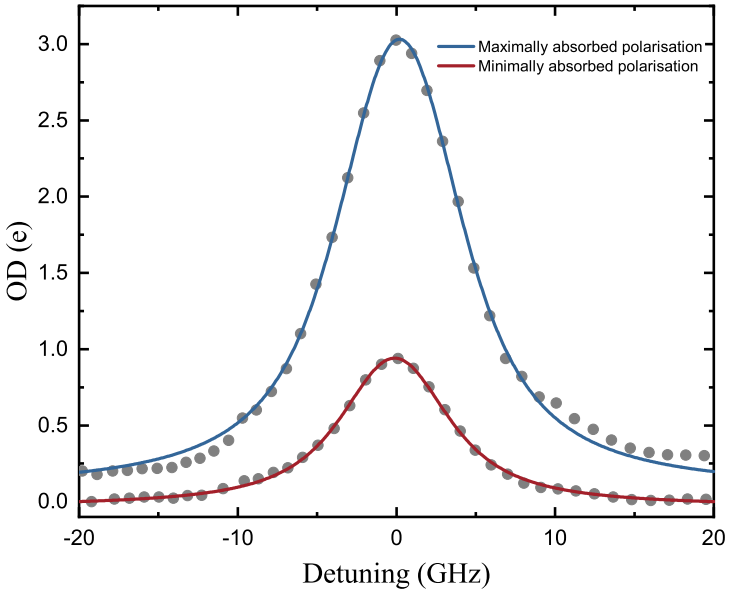

Fig. 4.3 : Optical depth of the ensemble $^3H_4(0) \leftrightarrow {}^1D_2(0)$ zero-phonon line as a function of detuning from resonance. As $\Gamma_{\text{inh}} \gg \Gamma_{\text{hom}}$, this is also a measure of inhomogeneous broadening in the ensemble. The blue and red curve correspond to the maximally and minimally absorbed polarisations respectively. The spectra are corrected for the probe pulse linewidth taking $\Delta\nu = 4$ GHz.

The sample is cooled to 2.6K using an Oxford Instruments Optistat Dry closed-cycle cryostat system, to which additional heat shields were added. Silver paint is used to fix the Pr:YSO sample to a holder connected to the cold finger. The cooling process induces vibrations in the cold head (estimated at $\sim 10\,\mu$m) at a rate of ~ 1 Hz, defined by the length of the compression cycle. Measurements are affected by these vibrations,

although not critically due to appropriate polishing of the crystal facets and the long timescales involved in the experiment. Excitation light from an optical fibre passes through a PBS and waveplates for polarisation cleaning and control and is then focused onto the centre of the sample with a f=200 mm plano-convex lens leading to a beam waist of approximately 100 μm. As neither the crystal nor the cryostat windows are anti-reflectively coated the transmission baseline of the cryostat setup is about 70% off-resonance.

Detection and measurement

After going through the cryostat, the beam is collimated using another f=100 mm lens and sent to the detection stage. In order to apply spectral hole burning on short enough timescales, a large amount of optical power is required in the pump beam. On the other hand, the probe has to remain many orders of magnitude weaker so as to not impact the atomic state of the ensemble. Filtering is thus essential to avoid contamination of the detected optical signal or damage to the detectors. Thankfully, the pulse sequences used in the experiment never require both beams to be active simultaneously. Spurious light can thus be simply filtered away using an additional shutter blocking the beam path when necessary.

For all absorption measurements, light was detected with a fixed-gain Thorlabs APD110A silicon avalanche photodiode (APD). In order to measure the AFC read-out pulses, a variable-gain APD (Menlo systems APD210) boasting a 0.5 ns rise time was used. With either detector, data is acquired with a fast oscilloscope (Teledyne Lecroy Wavesurfer 10). This setup is sufficient to accurately detect the weak classical pulses used throughout the experiment.

4.1.3 Broadband spectral hole burning

Using the setup described above, we manipulate the $^3H_4(0) \leftrightarrow {}^1D_2(0)$ transition in Pr^{3+}:Y_2SiO_5. The pulse sequence is as shown in Fig. 4.4: we first apply the pump beam, then the probe, and finally the we use the modulated pump beam to reset the ensemble to equilibrium populations. After imprinting the spectrum of the laser onto the inhomogeneously broadened line via spectral hole burning, the narrowband probe is scanned in order to perform spectroscopy of the shaped transition.

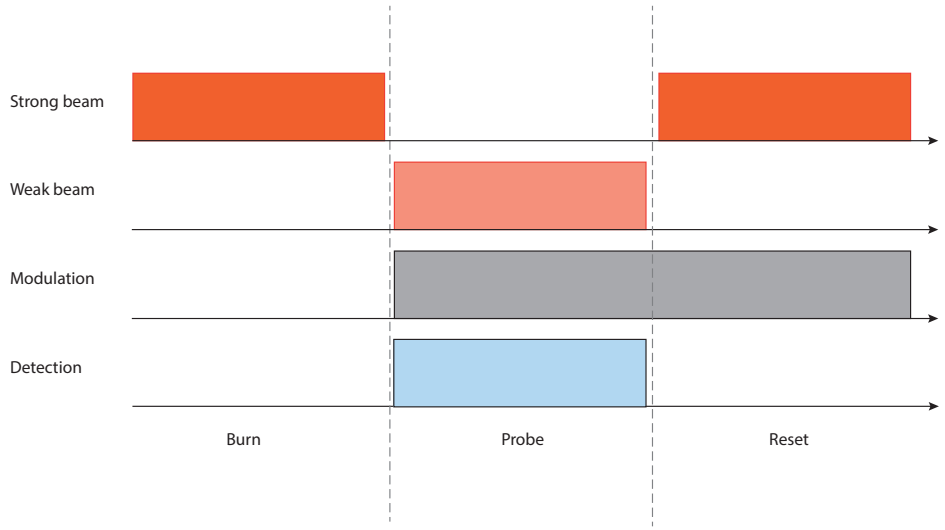

Fig. 4.4 : Pulse sequence used to prepare and probe the AFC profile.

Time traces are collected with an oscilloscope synchronised to the scanning cycle of the SPFI used to sweep the probe frequency. The reconstituted spectrum is presented in Fig. 4.5, showing the probe with and without the application of the pump beam.

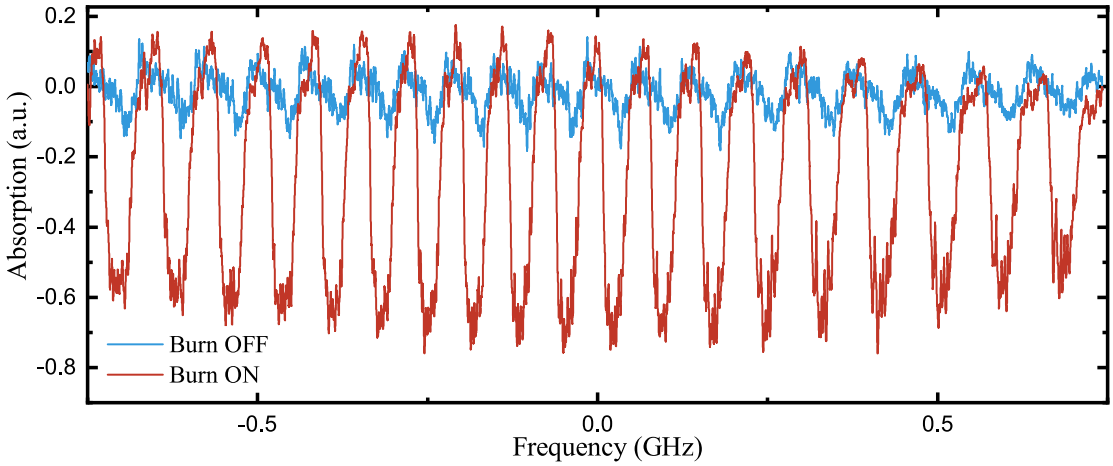

Fig. 4.5 : Transmission spectrum of the probe beam with and without activation of the burn beam, analysed by scanning and monitoring the absorption of a weak probe beam.

When the pump beam is on, the periodic structure of an AFC is very clearly imprinted over more than 1 GHz. The bare probe beam, shown in blue, also exhibits some periodic structure remaining from the original laser spectrum. This is due to

the diffraction efficiency of the AOM used for modulation depending on its driving frequency, which results in imperfections in the desired 'smoothing' effect.

Jitter in the laser causes the optical frequency comb to effectively have 40 MHz wide peaks and troughs, which is much wider than the hyperfine state splitting. The relative ground state populations are thus rearranged according to the relative transition strengths leading to the the observation of additional structure within the AFC peaks and troughs. This effect is also observed in results obtained from numerical simulations shown in Fig. 4.6. The burning laser is modelled as a collection of narrowband probes separated by 80 MHz which jitters by a maximum of 40 MHz around a central frequency, inspired from measurements of the laser spectrum. Each of the burning frequencies is taken into account in order to compute the pumping of atomic population along the inhomogeneous line and the resulting atomic frequency comb profile. We also consider the relative hyperfine state populations, which are redistributed according to the relative oscillator strengths for the optical transitions between the $^3H_4$ and $^1D_2$ hyperfine manifolds [135]. Within this framework, relaxation of the hyperfine states is neglected.

Due to its energy level structure, the widest maximally transparent spectral pit (i.e. where no ions are left to interact with a designated frequency band) achievable in praseodymium is 18.1 MHz [163]. Attempting to burn broader spectral features necessarily implies re-pumping some population into a state that has already been emptied out. This is the case with this experiment, and limits the contrast of the comb (defined as the ratio between absorption peaks and background absorption) to approximately 30%, with peaks at an optical depth $d_{peak} \sim 3.5$ and troughs at $d_{bg} \sim 2.5$.

The characteristics of the comb were further investigated as a function of burning time T_B and power P_B, as displayed in Fig. 4.7(a) and 4.7(b). The OD contrast plateaus when the pump beam is applied for longer times, suggesting an equilibrium state is reached with the internal atomic dynamics. For high optical intensities in the pump beam, power broadening in the ensemble blurs out the structure and reduces its contrast, which ultimately sets a lower bound on the how fast an AFC can be prepared. Unfortunately, when burning with lower powers, the comb contrast is limited by frequency drifts in the setup. These are due to both the laser central frequency drifting away from resonance as well as the cavity length of the etalon in the probe arm being subject to temperature fluctuations. The comb profile was also studied for a variety of laser detunings as shown in Fig. 4.7(c). While the flat difference in

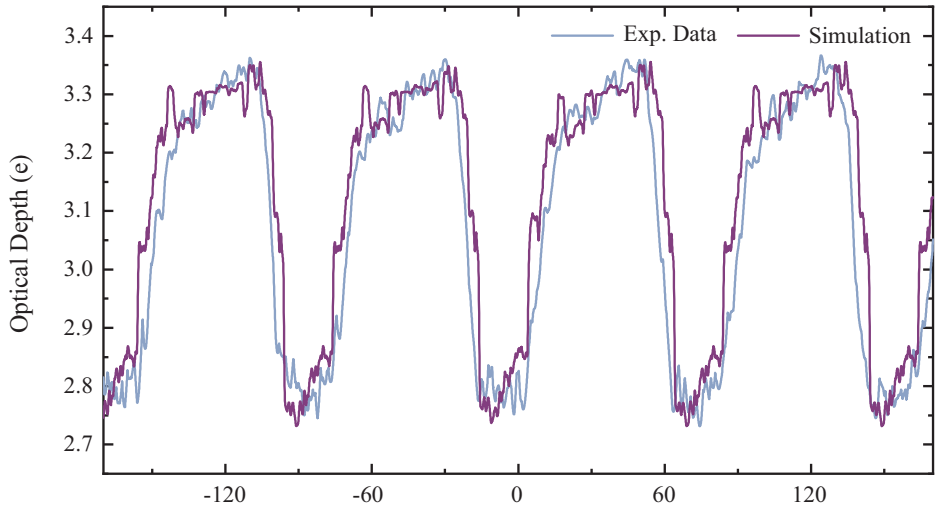

Fig. 4.6 : Comparison of measured (blue) and simulated (purple) comb shapes, assuming a laser centre frequency jitter of 40 MHz.

optical depth only decreases mildly with increasing detuning, the absorbing background can be almost entirely burned away when operating far away from resonance. This is relevant for the AFC protocol, as background absorption negatively impacts the read-out efficiency due to a portion of the collective atomic excitation being lost to random dephasing [96].

4.1.4 Storage of classical pulses

Having scouted out favourable pumping regimes, the base atomic frequency comb memory protocol is implemented. After preparing the AFC, a single weak classical pulse is selected using the pulse-picking setup and absorbed resonantly onto the transition in order to excite the ensemble. An echo-like readout pulse is then expected when the ions rephase after a time interval defined by the inverse of the comb peak separation, here 12.5 ns [96]. This technique enacts a pre-programmed delay line where light is stored in the excited state, as opposed to the true 'on-demand' quantum memory required for photon synchronisation. This demonstration is however a necessary step towards the development of a more complete protocol allowing long-term storage. However, enacting broadband ($\sim$ GHz) spin-wave storage with π-pulses would require upwards of 50 W of average optical power at 80 MHz, which is not accessible with the laser system used in these experiments.

A typical experimental sequence is then as follows. An atomic frequency comb is first prepared on the transition by directly applying the pulse train produced by the

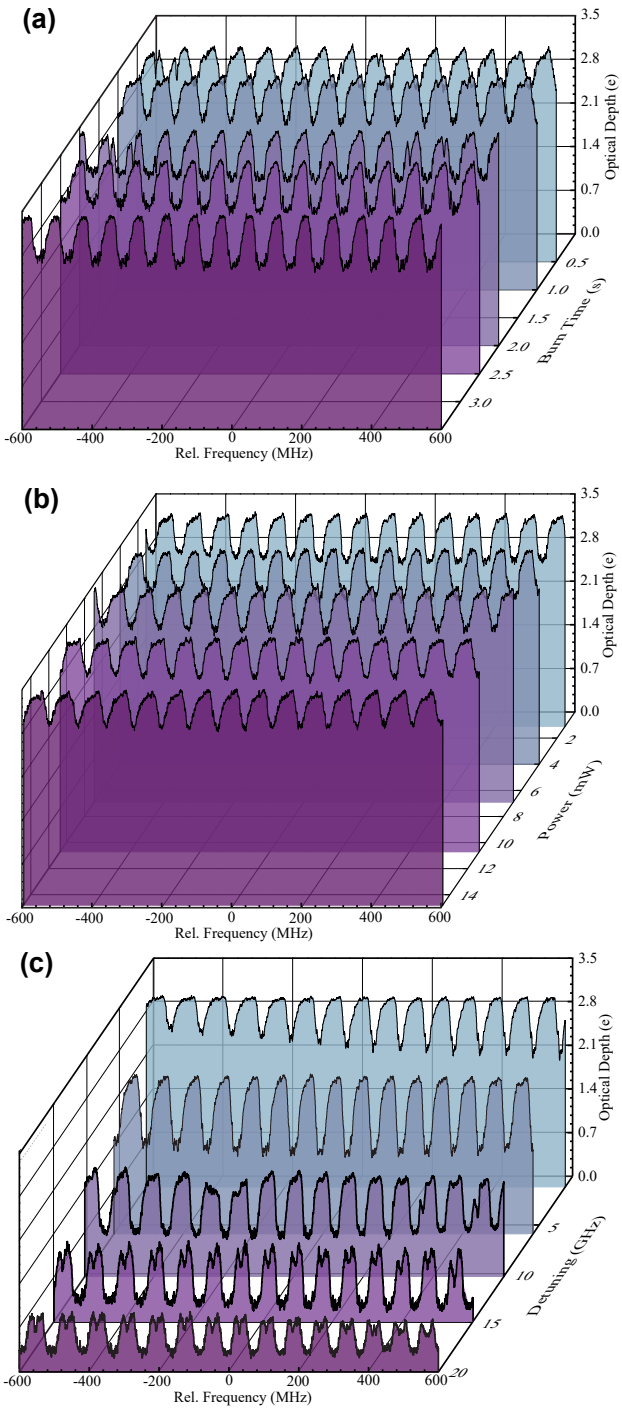

Fig. 4.7 : Broadband atomic frequency comb structures depending on (a) Burn time T_B i.e. length of the applied preparation pulse train (burn power $P_B = 1.1\,\mathrm{mW}$) (b) Burn power of the preparation pulse train P_B (T_B=2s) (c) Detuning from the centre of the inhomogeneous line ($T_B = 2\,\mathrm{s}$, $P_B = 1\,\mathrm{mW}$).

laser onto the sample at approximately 10 mW of average optical power. The burning beam is then blocked with a mechanical shutter with no detectable leakage, and a single read-in pulse is picked using the Pockels cell and absorbed onto the shaped transition. During this phase, the detector arm is unblocked and the absorption of the read-in pulse is measured along with the emission of any subsequent read-out echoes. Finally, the detector arm is blocked again, the AOM modulation is switched on, and the full power of the laser - approximately 25 mW before the cryostat - is applied onto the sample for at least 5 seconds. This has the effect of pumping the transition with power-broadened smooth profile until equilibrium is reached, effectively resetting the experiment. Throughout this experiment, the polarisation of all beams is horizontal, aligned to maximal absorption in the sample. The recorded signal is shown in Fig. 4.8, clearly displaying not one but many rephasing echoes.

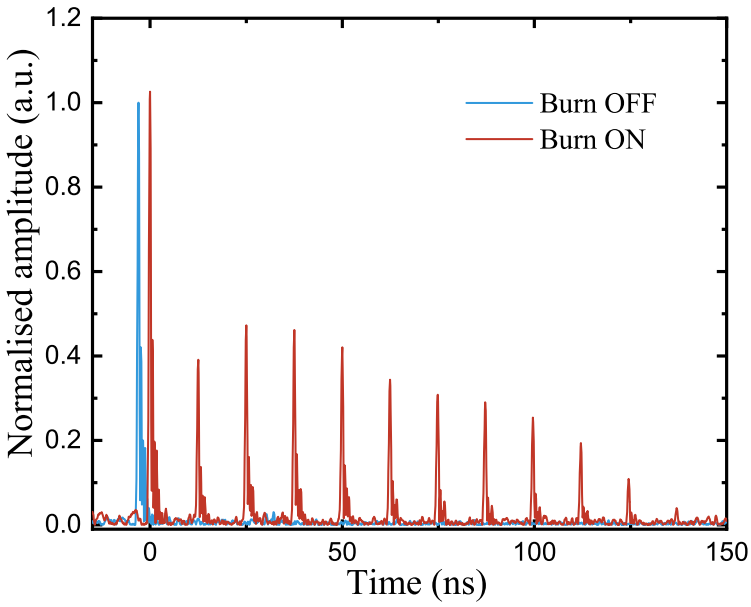

Fig. 4.8 : Time trace (red) of the photon echoes observed using a broadband AFC at $\Delta = 5$ GHz. The signal recorded in the absence of any AFC preparation is included for reference in blue, arbitrarily scaled for visibility.

The echoes are separated in time by 12.5 ns which is, as expected, the inverse of the comb spacing. However, the relative amplitude of successive echoes does not simply decrease due to the decay of the atomic excitation as would be the case of a perfect comb in a two-level system. Instead, the envelope first increases and then dies out

on a timescale of a few tens of nanoseconds. This additional structure is attributed to the excitation being spread over all ground states leading to an additional beating phenomenon which is reflected in the numerical simulations shown in Fig. 4.10. The secondary peaks observed after each echo in the experimental trace are artifacts caused by afterpulsing in the detector.

In the AFC protocol, each excited emitter accumulates a phase depending on its resonant frequency. An echo is observed when the collective state of the ensemble, given in Eq.2.3 rephases due to the comb structure. This occurs when each of the terms in the superposition $\sim c_i e^{i\delta_i t}$ for an emitter i interfere constructively. Formally, the temporal profile of the rephasing echoes is determined by the Fourier transform of the atomic spectral distribution. In our simulations, measurements of the AFC profile are used to define parameters c_i and δ_i. We also assume that by the end of the comb preparation process, the majority of the ions are pumped into the $\pm 5/2$ hyperfine ground state, which is coupled to three optical transitions. These transitions are modelled as three distinct atomic frequency combs with equal spacing but detuned with respect to each other by an amount equal to the hyperfine state splitting. While broadband pumping of the ensemble could lead to re-pumping of population into the other hyperfine state, including only three transitions in our model was sufficient to reproduce the relevant dynamics. Finally, a finite AFC peak γ width is associated with exponential decay of successive echo amplitudes following a time constant $\sim 1/\gamma$.

The read-out signal was plotted for two different detunings and displayed in Fig. 4.9.

This data provides additional information concerning the regimes in which the memory scheme can be operated. For average burning powers in excess of 20 mW, no echoes are recorded. This is in accordance with the deterioration of the comb profile for higher powers due to power broadening shown in Fig. 4.7. Detuning the laser seems to increase the read-out amplitude, which agrees with previous results where higher comb contrasts could be obtained off resonance. The efficiency of the memory scheme, defined as the ratio of input to output, is plotted below (Fig. 4.11 for a range of detunings. The highest efficiency recorded values are $\eta_{AFC}^{(tot)} \sim 20\%$ summing over all echoes and $\eta_{AFC}^{(1)} \sim 10\%$ for any single echo. Here, the efficiency is defined as the ratio of the echo amplitude to the imput amplitude. These values cannot be reproduced using the analytical expression given in Eq. 2.7, as it relies on many assumptions - Gaussian AFC peaks, narrow input signal bandwidth, and a single class of emitters - that are not valid in this experiment.

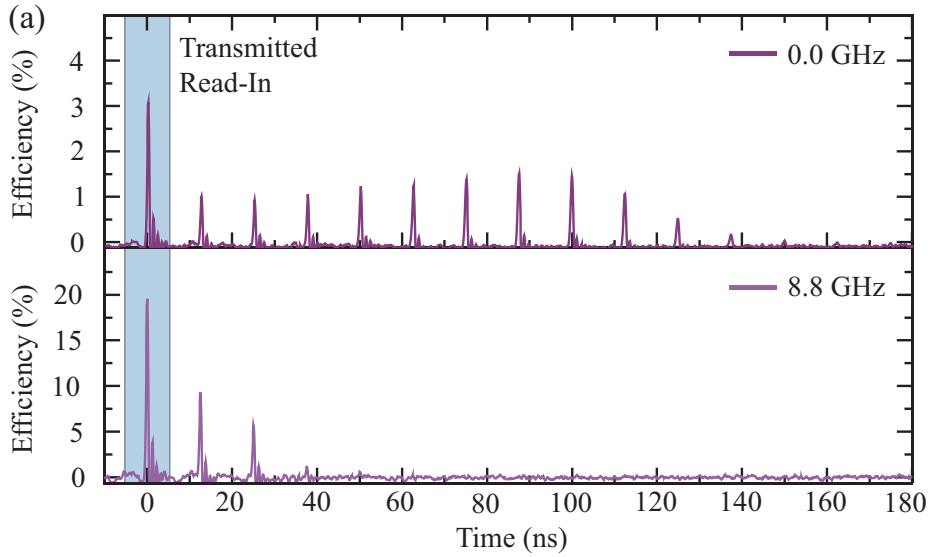

Fig. 4.9 : Photon-echo time traces for 0 and 8.8 GHz detuning from the inhomogeneous line center (burn time $T_B = 2\,\mathrm{s}$, burn power $P_B = 1\,\mathrm{mW}$)

This experiment constitutes to our knowledge the first demonstration of a GHz-compatible AFC echo scheme in praseodymium, and paves the way for the realisation of a fully on-demand broadband quantum memory in the solid state. The setup is however far from being optimised, and many technical aspects have yet to be addressed. Indeed, spectral jitter of the laser is the one of the main factors limiting the comb contrast, as it fixes the comb teeth width to ∼40 MHz which induces re-pumping within the ensemble. The ability to produce an optical frequency comb with peak widths under 18.1 MHz (the maximal width of a spectral pit [135]) would then allow the engineering of AFCs with much higher comb contrast. Furthermore, given more control over the laser spectrum one could burn potentially wider features using techniques described in Ref. [163], leading to higher echo efficiencies.

The laser spectrum is broadened on short timescales by two main factors caused by fluctuations in dye jet. Such fluctuations affect the laser cavity length, leading to jitter of the comb centre frequency which shifts the entire spectrum. Furthermore, instability of the carrier-envelope offset phase leads to a breathing motion in the optical comb, where peaks close to the central frequency are shifted less than peaks further away. Both of these effects may in principle be addressed by applying active stabilisation techniques to the laser [166]. For example, cavity length fluctuations can be mitigated by placing a fast electro-optic modulator within the cavity in order to adjust the

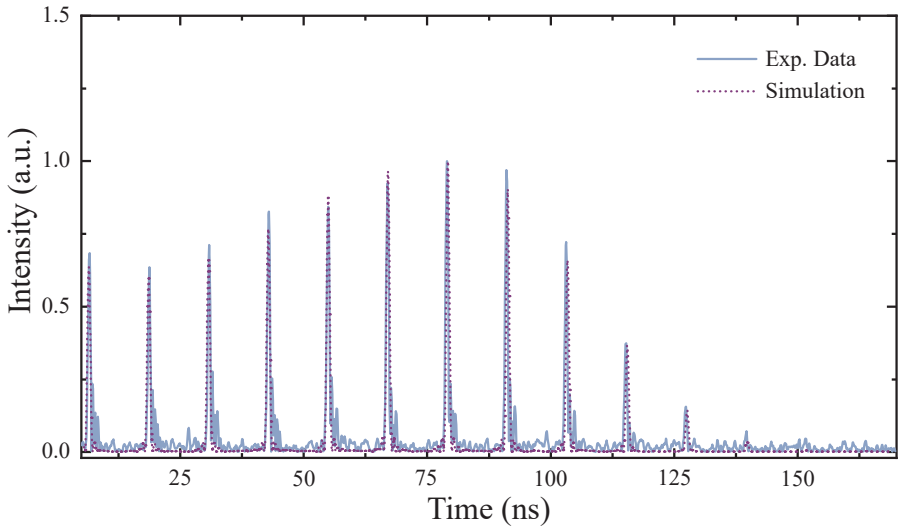

Fig. 4.10 : Comparison of simulated and measured photon echoes. The measured echoes were observed for the following comb preparation parameters: 0 GHz detuning, $T_B = 2\,\mathrm{s}$, and $P_B = 1.1\,\mathrm{mW}$. The secondary peaks observed after each echo in the experimental trace are artifacts caused by afterpulsing in the detector.

the optical path length in real time via an external feedback signal collected from a measurement of the laser spectrum.

Although the efficiency of the protocol is respectable for a proof-of-principle demonstration, it is not sufficient when considering applications such as quantum repeaters or photon synchronisation. Increasing the optical depth of the sample is perhaps the most straightforward way towards addressing this issue. Increasing the doping concentration in the host crystal tends to introduce further strain and damage to the lattice and introduces further inhomogeneous broadening on all transitions. However, this is only true until the REI concentration exceeds that of the element it replaces within the host. Beyond that, the rare-earth becomes a major element of the lattice and further increasing the concentration instead reduces broadening as the crystal approaches stoichiometry. Stoichiometric samples exhibit both high optical depths and lower inhomogeneous broadening [167], providing an ideal system for the implementation of this protocol. Using waveguides to confine light to smaller volumes in the sample can also lead to more efficient light-matter interaction with the ensemble. Nanophotonic structures have been successfully used as an optical interface with REI ensembles, allowing for example the storage and retrieval of single photons in a praseodymium-doped laser-written waveguide [168], as well as in an erbium-doped lithium niobate waveguide [169].

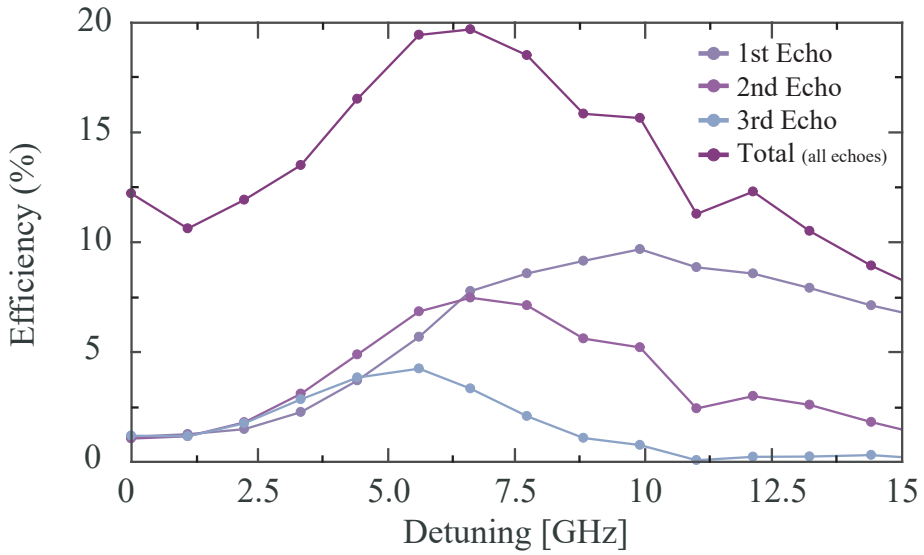

Fig. 4.11 : Plot showing the efficiencies of the first, second and third echoes as well as the total efficiency (sum of all visible echoes) as a function of detuning.

Finally there remains the underlying issue of the narrow hyperfine splitting in praseodymium, which sets an intrinsic limit of a few MHz to the bandwidth of pulses one can store in the long-lived hyperfine ground states. As a result, the traditional full AFC protocol with spin-state storage cannot be implemented using GHz-order pulses in praseodymium. Considering other species of rare-earths with larger ground-state splittings such Ytterbium [170] or Thulium [171] may offer a way forwards. Alternatively, one can consider applying a memory protocol which does not require transfer to the ground state, such as ORCA [106] (described in section 2.3.1) where an excitation is stored in an excited state of an atomic ensemble using a two-photon transition via an intermediate state. In Pr^{3+}:Y_2SiO_5, an AFC can then be used in order to mitigate the fast dephasing of the excited state and allow storage times approaching its T_2 coherence time. This idea is explored in more detail in the following section, where preliminary results investigating the $^3H_4(0) \leftrightarrow ^3 F_3(0)$ transition at 1550 nm (telecom C-band compatible) and $^3F_3(0) \leftrightarrow ^1D_2(0)$ transition at 995 nm in Pr^{3+}:Y_2SiO_5 are presented.

4.2 Towards a ladder-type memory in Pr^{3+}:Y_2SiO_5

Storage and retrieval of broadband classical pulses was successfully demonstrated in the previous section. However, the usefulness of this technique for the development

of interesting applications such as photon synchronisation or quantum repeaters is limited by two fundamental aspects. The first and main drawback is the lack of on-demand read-out of the memory, which occurs only when the excitation stored in the excited state rephases after a time given by the AFC characteristics. Furthermore, the wavelength of the $^3H_4(0) \leftrightarrow {}^1D_2(0)$ transition is relatively inconvenient for both single-photon generation and long-range optical communication. In order to address these issues, we propose to implement the off-resonant cascaded absorption quantum memory protocol (ORCA - see section 2.3.1) in this system. ORCA relies on a ladder-type three-level energy structure with ground, intermediate and storage states labeled $|g\rangle$, $|e\rangle$ and $|s\rangle$ respectively as shown in Fig. 4.12. A strong 'control' field applied to the $|e\rangle \leftrightarrow |s\rangle$ transition enables the absorption of a weak propagating optical 'signal' field on the $|g\rangle \leftrightarrow |e\rangle$ transition and its subsequent mapping to a coherence between the $|g\rangle$ and $|s\rangle$ states of the atomic ensemble. The coherence can be stored for the collective atomic excitation decoheres, and the signal retrieved in the form of an optical signal by applying the control field again.

Such an atomic system exists in Pr^{3+}:Y_2SiO_5 via two weakly allowed transitions, $^3H_4(0) \leftrightarrow {}^3F_3(0)$ at 1550 nm and $^3F_3(0) \leftrightarrow {}^1D_2(0)$ at 995 nm (see Fig. 4.12). In principle, this allows the implementation of the ORCA protocol with a signal wavelength compatible with telecom C-band optics and storage in the $^1D_2(0)$ state. Due to substantial inhomogeneous broadening of the storage state, the coherence is expected to dephase extremely fast. However, this pure dephasing effected can be mitigated by additionally generating an atomic frequency comb on the $^3H_4(0) \leftrightarrow {}^1D_2(0)$ transition. In theory, the storage time of the memory is then only bounded by the coherence time of the storage state $T_2/4$ due to the holeburning resolution limit imposed by the homogeneous linewidth of the emitter [172]. Momentum conservation has to be satisfied in this system, leading to two phasematching conditions necessary for the retrieval of the stored excitation.

The collective excitation of the ensemble generated via the ORCA protocol, known as the orbital wave, has a well-defined spatial phase profile and associated wavevector. This wavevector is dependent on the detunings and propagation direction of the signal and control beams during the storage interaction. In order to recover the excitation, momentum conservation stipulates that the wavevectors associated with the signal, control and orbital wave should add up to zero during the retrieval process. This first condition makes the application of the control field necessary to the retrieval process.

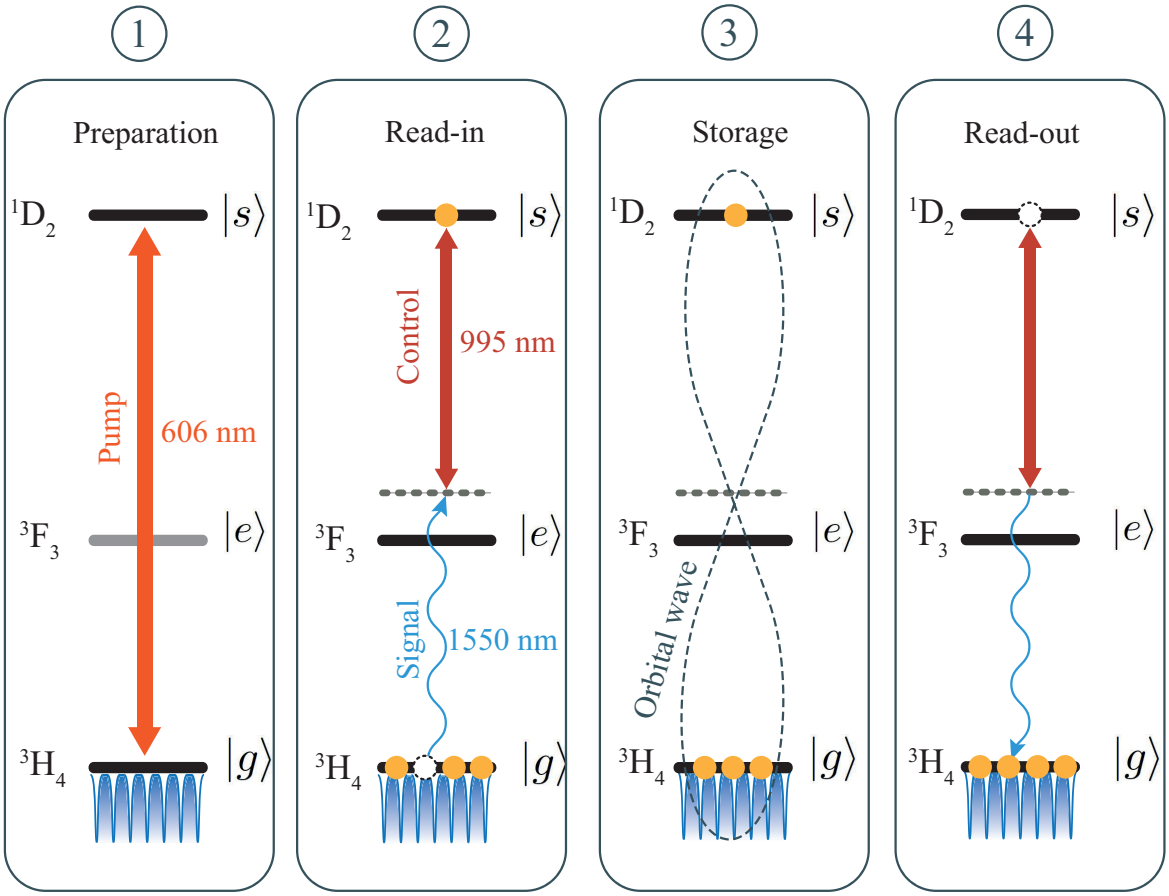

Fig. 4.12 : Diagram describing a combined AFC-ORCA quantum memory protocol. 1) An AFC is first prepared on the $^3H_4 \leftrightarrow {}^1D_2$ transition. 2) A photon is absorbed on the lower transition using a strong control field on the upper transition. 3) The excitation is mapped to a coherence of the $|g\rangle$ and $|s\rangle$ states or 'orbital wave'. 4) The signal can only be retrieved via an application of the control field concurrent with an AFC echo.

The second condition is simply the rephasing of the inhomogeneous atomic emitters according to the AFC protocol.

The control field can thus be switched on in order to retrieve the stored excitation during any of the periodically occurring AFC rephasing windows. This constitutes a protocol for a (quasi-)on-demand telecom-compatible broadband quantum memory in a solid-state platform.

To the best of my knowledge, the relevant transitions in Pr^{3+}:Y_2SiO_5 were found to be somewhat under-documented. In this section, we present the results of a preliminary spectroscopic investigation of the $^3H_4(0) \leftrightarrow {}^3F_3(0)$ and $^3F_3(0) \leftrightarrow {}^1D_2(0)$ transitions, which aim to determine the feasibility of the protocol outlined above.

4.2.1 Experimental setup

The same cryostat system and sample were used for these experiments as in the previous section. However, the wavelengths necessary here required a different set of light sources and detection systems altogether, which will be described in the following.

Light sources

A semiconductor laser (Santec TSL510) was used in order to address the 1550 nm $^3H_4(0) \leftrightarrow {}^3F_3(0)$ transition. It outputs a fibre-coupled continuous-wave (CW) narrowband optical signal with a 40 MHz linewidth and 40 mW average power. The laser is finely tunable from 1500 nm to 1630 nm in 1 pm (∼125 MHz) increments while offering 65 dB suppression of amplified spontaneous emission noise, and is a reliable tool for narrowband absorption spectroscopy.

Higher optical power may be required in order to reliably pump the $^3H_4(0) \leftrightarrow {}^3F_3(0)$ transition and observe absorption on the $^3F_3(0) \leftrightarrow {}^1D_2(0)$ line. To this end, the Santec TSL510 can be used to seed a Pritel PMFA-33 erbium/ytterbium-doped fiber amplifier (EDFA). The EDFA then offers up to approximately 1 W of optical power with negligible impact on the signal linewidth within the 1535-1565 nm range. In the following, we sometimes refer to this assembly simply as the 'telecom laser'.

Light at 995 nm is provided by a self-seeded tapered amplifier (TA) designed and built in house for this experiment, which consists of an external cavity placed around a DILAS TAL-1010-2000 chip (see Figs. 4.13 and 4.14).

When the chip is pumped electrically, it emits ASE from both its front and back facets with a broad spectral profile ranging from approximately 980 nm to 1030 nm. ASE from the back facet is collected with an aspheric lens, polarisation rotated with a HWP, spectrally filtered with a thin etalon, and sent onto a diffraction grating (1800 lines/mm). The first diffracted order is reflected back into the chip and seeds the lasing process, where the tapered amplifier is the gain medium and the cavity 'mirrors' consist of the chip front facet and the grating. The seed light heavily skews the gain dynamics of the laser and determines its spectral properties accordingly. Here, ASE from the seed beam is spectrally filtered down twice, first by the etalon and then by the fact that only a small portion of the light dispersed by the grating is coupled back into the tapered amplifier. This ensures narrowband operation of the laser system. Temperature and current stability of the device is guaranteed by a Thorlabs LDC4005

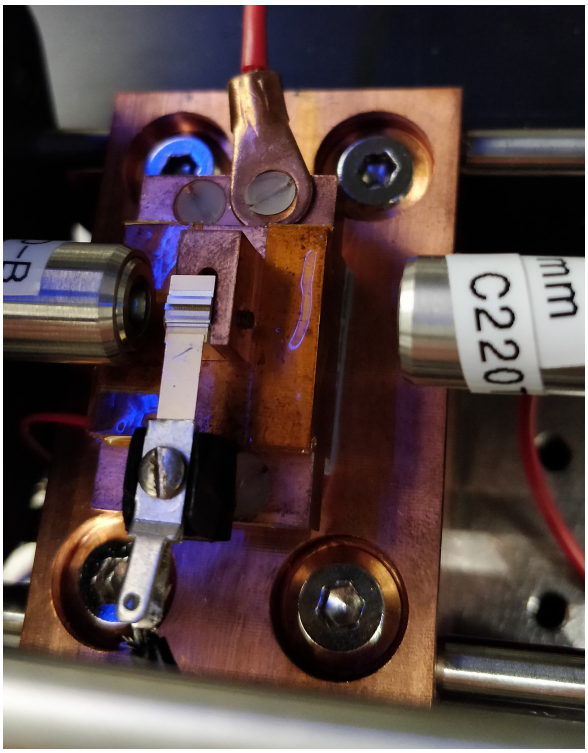

Fig. 4.13 : Photograph of the mounted tapered amplifier chip.

high-power laser diode controller, connected to a thermal sensor and a Peltier element applied to the chip mount.

The laser output is collected from the chip front facet and has an elongated and very divergent spatial profile due to the geometry of the gain medium. Rudimentary beam-shaping is achieved via a cylindrical lens with 100 mm focal length allowing the beam to be coupled into optical fibre in order to obtain a clean Gaussian mode. Further beam processing was limited by the device remaining very sensitive to back-reflections despite the inclusion of an optical isolator. Light is picked off from the main output and sent to an optical diagnostic stage, consisting of a Thorlabs SA210-8B SFPI (10 GHz FSR, 67 MHz resolution) for fast spectrum imaging and a HighFinesse WS6-600 wavelength meter (600 MHz resolution) for frequency monitoring. As previously, the SFPI is controlled by a Toptica SC110 scanning module. With a cavity length of 48 cm, the laser provides a continuous-wave optical signal tunable from 990 nm to 1030 nm. It offers stability down to approximately 100 MHz while providing 700 mW of optical power. A measurement of the laser spectrum with the SFPI is limited by the resolution of the interferometer, only allowing a bound to be placed on the linewidth given by $\Delta\nu_{TA} \leq 67\,\mathrm{MHz}$.

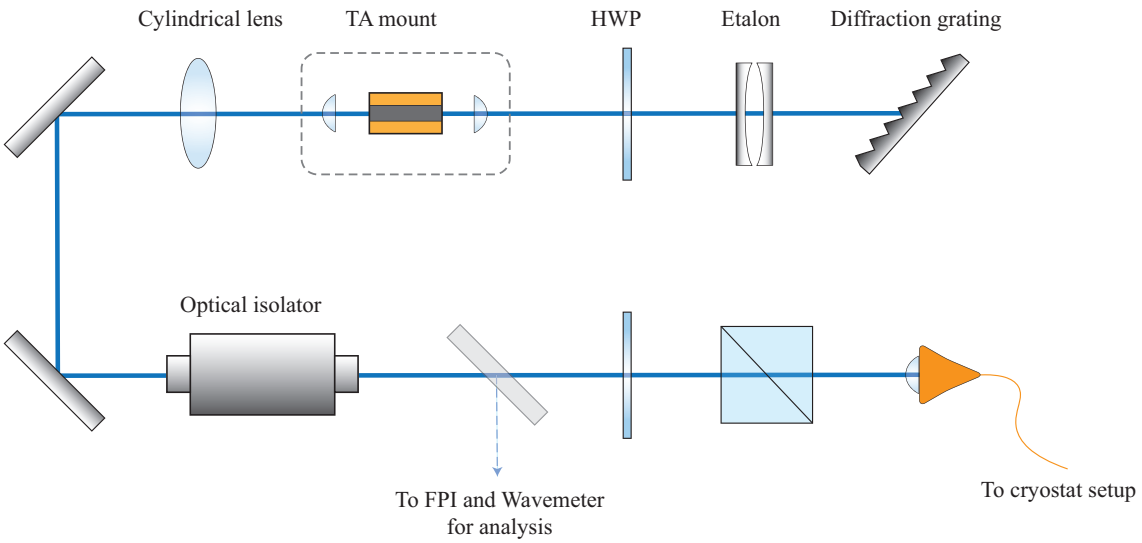

Fig. 4.14 : Optical diagram of the self-seeded TA setup. Emission from the back facet is filtered via a diffraction grating and reflected back into the chip in order to seed a lasing process. The laser emission is collected from the front facet.

Light from both lasers is brought to the main setup via optical fibre and collimated with aspheric lenses selected in order to generate beams of equal diameters. A small portion of the 1550 nm beam is picked off and sent to a frequency doubling stage, which was necessary for calibration purposes (see section 4.2.2). The infrared light is focused onto a beta barium borate (BBO) crystal in order to pump a type-I frequency-doubling process. The pump beam is then blocked out using a standard low-pass filter and the signal is collected at 775 nm with an aspheric lens and coupled into fibre. The setup is outlined in Fig. 4.15.

After polarisation control with a QWP and HWP in each beam path, both wavelengths are combined on a dichroic mirror (Thorlabs DMLP1180) before being focused onto the Pr^{3+}:Y_2SiO_5 sample placed in the cryostat (see section 4.1.2) via a 75 mm focal length achromatic plano-convex lens. Light transmitted through the crystal is then collimated using another identical lens and the two wavelengths are separated with a dichroic mirror before being sent to detectors.

Detectors

This experiment requires detection of light at 1550nm, 995nm, and 606nm at light levels ranging from sub-pW to mW. For higher powers a standard free-space switchable gain germanium photodiode is used (Thorlabs PDA50B2, 800-1800 nm). The electrical

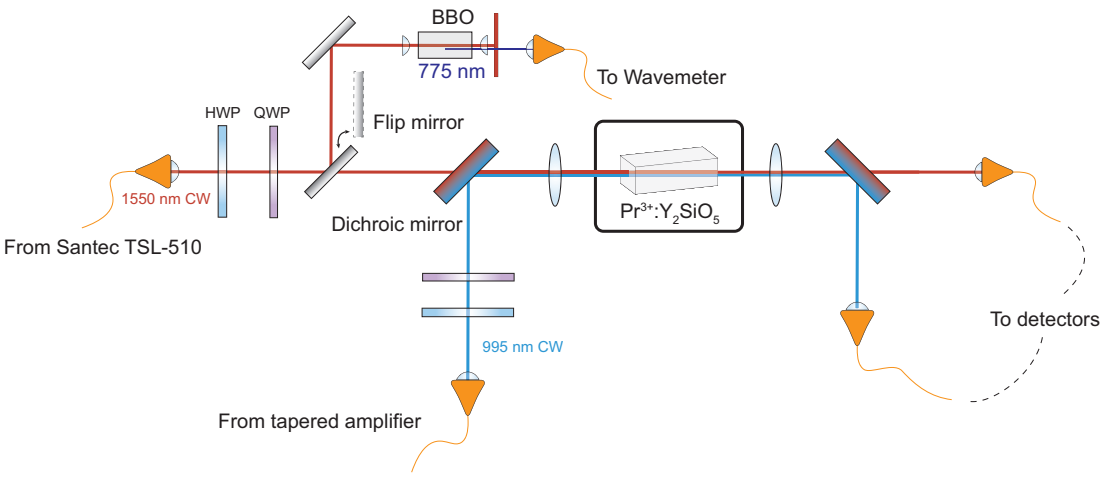

Fig. 4.15 : Diagram of the optical setup used for probing the $^3H_4(0) \leftrightarrow {}^3F_3(0)$ and $^3F_3(0) \leftrightarrow {}^1D_2(0)$ transition in Pr^{3+}:Y_2SiO_5. CW lasers at 1550 nm and 995 nm are combined and sent directly onto the cryogenically cooled sample in order to perform narrowband spectroscopy. The 1550 nm beam is also frequency-doubled for calibration purposes.

signal from the diode is then recorded on a fast oscilloscope. Level fluorescence from the $^1D_2(0)$ state at 606 nm is detected using an Excelitas silicon single-photon counting module (SPCM-AQRH) with 150 Hz dark counts, a quantum efficiency of ~65%, and a timing resolution of 350 ps. The SPCM produces a digital signal which is read out using counting electronics in the form of a Swabian TimeTagger (3 ps timing resolution, 4 channels). Similarly, detection of weak infrared light was achieved via the use of an InGaAs SPCM (ID Quantique ID220).

The relevant optical fields and transitions are summarised in Fig.4.16 for clarity.

4.2.2 Absorption spectroscopy of the $^3H_4 \leftrightarrow {}^3F_3$ transition in Pr^{3+}:Y_2SiO_5

Simple absorption spectroscopy of the $^3H_4 \leftrightarrow {}^3F_3$ transition around 1550 nm is performed. The laser is swept from 1500 nm to 1630 nm at a rate of 100 nm/s, with light transmitted through the sample collected onto a Ge photodiode. Traces are recorded on a fast oscilloscope for two different polarisation settings and shown in Fig. 4.17 in units of OD. Six absorption peaks are observed from 1507 nm to 1550 nm with widths ranging from 5 to 70 GHz, corresponding to different crystal field energy levels. Note that $2J + 1 = 7$ peaks should be expected: we surmise that an eventual seventh peak could not be observed due to low visibility or the limited wavelength range of the

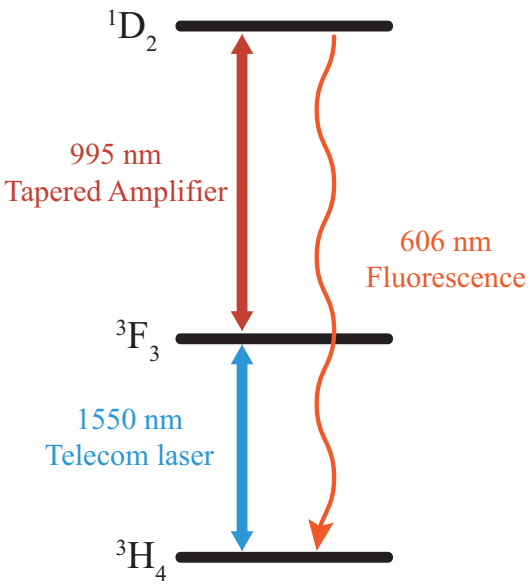

Fig. 4.16 : Relevant ladder system in Pr^{3+}:Y_2SiO_5.

laser scan. The zero-phonon line corresponds to the lowest-energy peak (number 1) at 1550.3 nm and is also the narrowest as expected due to the absence of phononic decay processes. The width and centre wavelength of each absorption feature can be found in more detail in table 4.1.

Peak	Wavelength (nm)	Width (nm)	Width (GHz)
1	1550.3	0.04	5.0
2	1542.8	0.06	7.9
3	1528	0.38	48.5
4	1524	0.38	49.4
5	1513.2	0.48	63.2
6	1507.5	0.53	70.1

Table 4.1 : Central wavelengths and peak widths associated with the transitions shown in Fig. 4.17

All transitions except for number 3 (as numbered in Fig. 4.17) show polarisation dependent absorption. The optical depth of each feature as a function of input light polarisation is plotted in Fig. 4.18. Transitions 1 and 6 appear orthogonal to 2,4, and 5 with peak 3 remaining constant throughout and showing no distinguishable polarisation dependence.

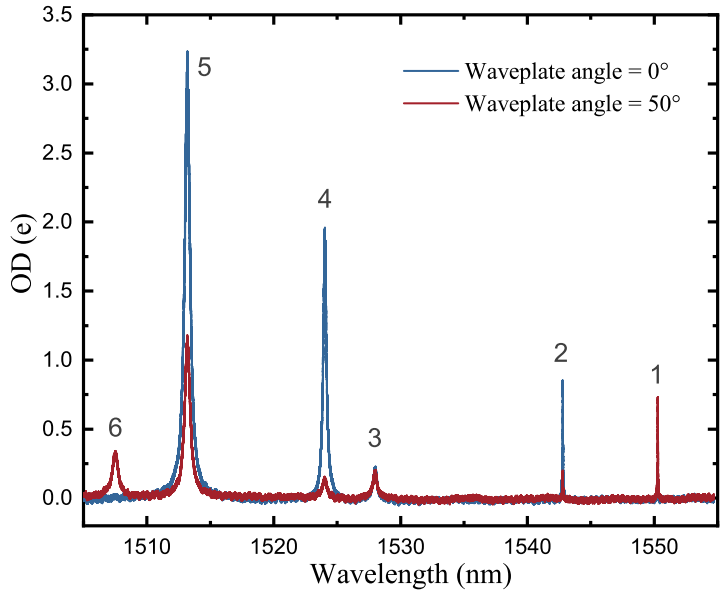

Fig. 4.17 : Transitions associated with the different crystal field levels in the $^3F_3$ manifold, numbered from 1 to 6 with increasing energy. The zero-phonon line corresponds to peak 1. Traces are taken for two orthogonal polarisations aligned for maximal (orange) and minimal (blue) absorption on the ZPL.

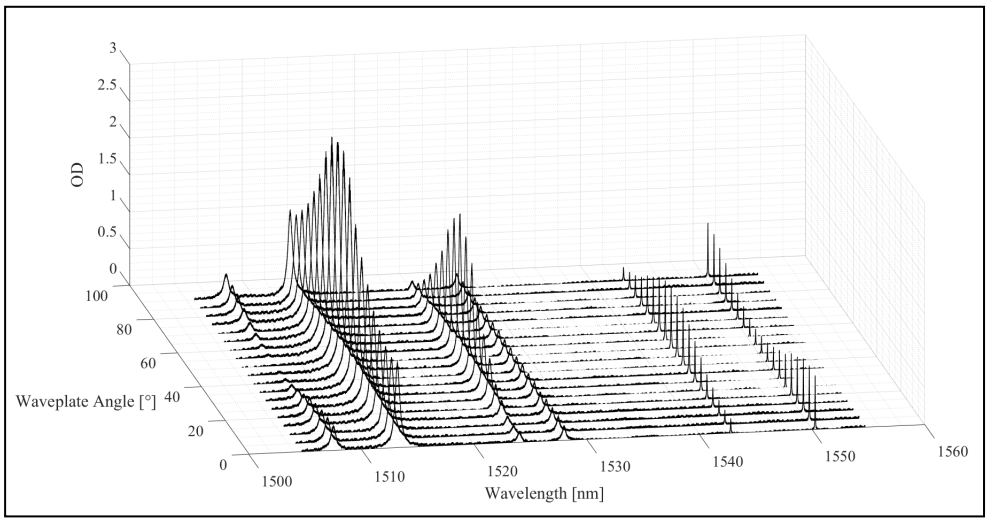

Fig. 4.18 : Polarisation dependence of the transitions associated with the different crystal field levels in the $^3F_3$ manifold.

Of these transitions, only the ZPL is of potential interest for the implementation of the ORCA protocol as it is unaffected by phonon-mediated decay processes. Going forwards we will focus on $^3H_4(0) \leftrightarrow {}^3F_3(0)$ transition in particular. The absorption feature is shown in Fig. 4.19.

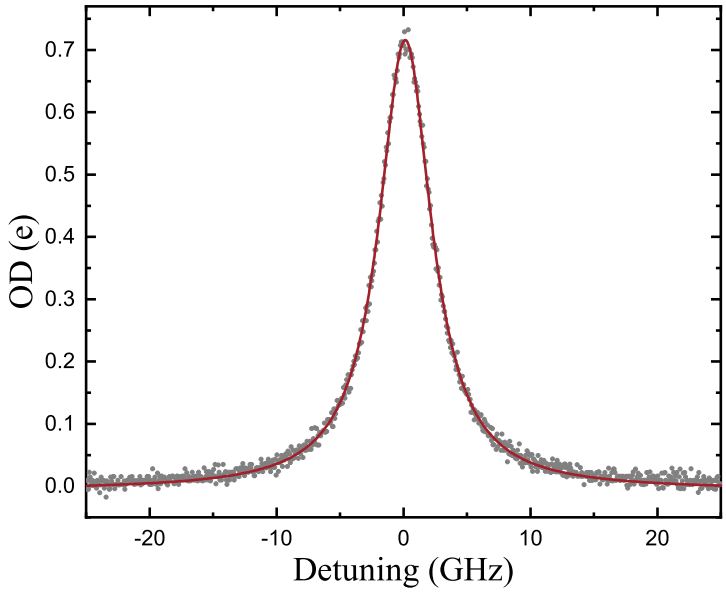

Fig. 4.19 : Absorption spectrum of the $^3H_4(0) \leftrightarrow {}^3F_3(0)$ transition zero-phonon line, measured using a weak narrowband probe.

This measurement confirms a transition width of $\Gamma_{\text{inh}} \sim 5\,\text{GHz}$ and suggests an optical depth $d \sim 0.7$ after correcting for losses at the cryostat windows.

After confirming the existence of the required absorption feature at 1550 nm, we now turn our eye to the $^3F_3(0) \leftrightarrow {}^1D_2(0)$ transition, supposedly located around 995 nm. As the tapered amplifier is not easily scanned across more than a few MHz before mode-hopping typically by GHz at a time, finding the exact wavelength of the transition is a tedious task. Furthermore, as the 1550 nm laser is continuous-wave, it is difficult to saturate the lower transition. Due to low steady-state population in the $^3F_3(0)$ state we expect very weak absorption on the upper transition, making the task of locating the transition more of a challenge.

In order to approach this issue, we choose instead to detect fluorescence emitted from the $^1D_2$ state. As the storage state is expected to be empty when the system is at rest, detection of fluorescence at 606 nm while both infrared fields are on resonance is a

clear marker of absorption on the $^3F_3(0) \leftrightarrow {}^1D_2(0)$ line. We infer the wavelength of the upper transition via energy conservation rules, as the frequencies of the $^3H_4(0) \leftrightarrow {}^3F_3(0)$ and the $^3H_4(0) \leftrightarrow {}^1D_2(0)$ lines are known precisely. The absolute wavelength of the telecom laser is however also unknown, and outside of the measurement range accepted by the Wavemeter used to measure the 606 nm transition. In order to obtain an estimate of the Santec laser frequency which is compatible with the Wavemeter calibration, we opt to frequency-double the telecom signal. As mentioned previously, light from the 1550 nm beam is focused onto a BBO crystal and used to pump a Type-I up-conversion process whereby a secondary optical signal is produced at half the pump wavelength. Up-converted photons are isolated from the pump beam using optical low pass filtering, coupled into optical fibre, and sent to the wavemeter.

A strong beam in resonance with the lower transition is then applied to the sample. We scan the TA and monitor fluorescence emitted on the $^1D_2(0) \rightarrow {}^3H_4(0)$ line with a single-photon counting detector while blocking the pump wavelengths using stacked optical filters with no detectable leakage (estimated $OD_{filters} > 12$). The results are presented in Fig. 4.20 for an average power of 40 mW at 995 nm and both 40 mW and 1 W at 1550 nm.

The emission peak is centred around 994.85 nm and shows a width of approximately 5 GHz for a telecom excitation power of $P_{telecom} = 40$ mW, possibly limited by the width of the lower transition.

Having successfully located the transition, we now look to measure the absorption of a weak resonant optical signal at 995 nm conditioned on the application of a strong control beam at 1550 nm. Here, the signal and control wavelengths are reversed with respect to the ORCA protocol described previously out of convenience, as high optical powers were more readily available at 1550 nm through use of the EDFA. The tapered amplifier is tuned onto resonance with the upper transition while the EDFA seed is scanned across the $^3H_4(0) \leftrightarrow {}^3F_3(0)$ line. The control beam is filtered out and we collect light at 995 nm transmitted through the sample using a photodiode, the signal of which is then then fed into a lock-in amplifier (LIA, Stanford Research 810). The LIA outputs a DC voltage proportional to any modulation of the input signal at a given reference frequency. The amplitude of the 1550 nm beam is modulated at 800 Hz using an optical chopper (Thorlabs MC1F10A, controlled by a MC2000B module) using a stable external input provided by an arbitrary waveform generator which generates a square wave with 50% duty cycle. The output from the AWG is also used as the reference frequency of the lock-in amplifier. Effectively, this setup allows the detection

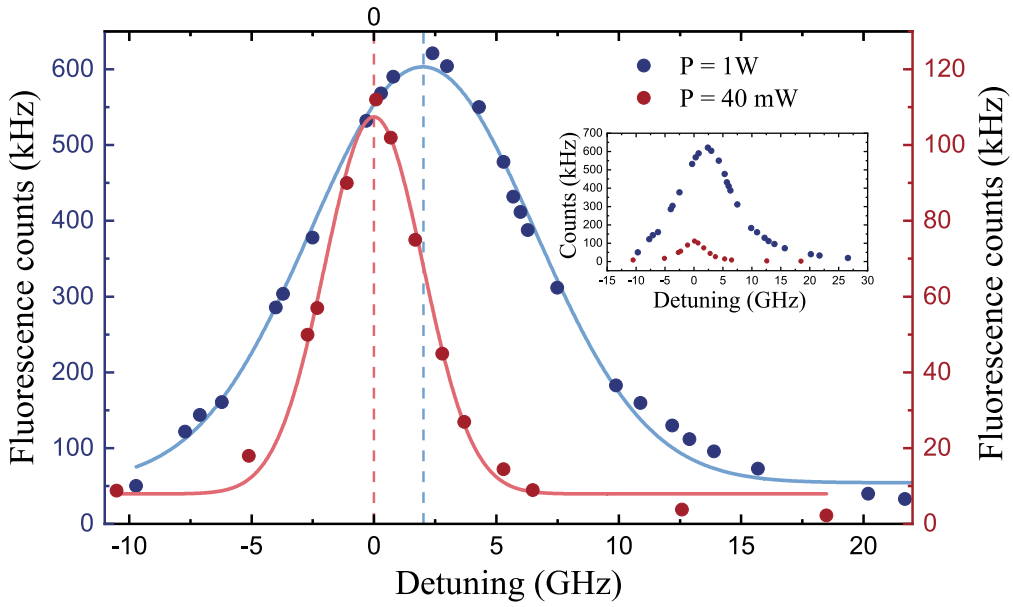

Fig. 4.20 : Fluorescence emission on the $^1D_2(0) \rightarrow^3 H_4(0)$ line as a function of the frequency of the 995 nm laser used to excite the $^3F_3(0) \leftrightarrow {}^1D_2(0)$ transition conditioned on the application of a strong resonant optical field on the $^3H_4(0) \leftrightarrow {}^3F_3(0)$ transition. Traces are recorded for telecom excitation powers of 40 mW and 1 W. The x-axis refers to detuning of the tapered amplifier.

of any change in amplitude of the signal beam conditioned on the application of the control while filtering out noise and unrelated systematic effects in the system. The lock-in voltage as a function of control frequency is presented in Fig. 4.21, showing a clear 5 GHz wide absorption feature.

This measurement confirms that at least in principle, this system can be used to implement a resonant ladder quantum memory protocol. The ORCA scheme itself is based on off-resonant two-photon transitions via an intermediary virtual state, which have yet to be observed in this system. To this end, we choose to return to fluorescence based detection. The tapered amplifier is blue-detuned $\Delta = +26$ GHz from the $^3F_3(0) \leftrightarrow {}^1D_2(0)$ line with the telecom laser scanned around a frequency red-detuned the same amount from the lower transition resonance. We monitor fluorescence at 606 nm like in previous measurements while keeping both optical fields at full power, and the results are shown in Fig. 4.22(a).The peak at $\Delta = +26$ GHz is the desired detuned two-photon transition - its width is expected to be limited by the finite decay rate of the storage state . The converse case, where the tapered amplifier is red-detuned while the telecom laser is blue detuned, is shown in Fig. 4.22(b), where a similar

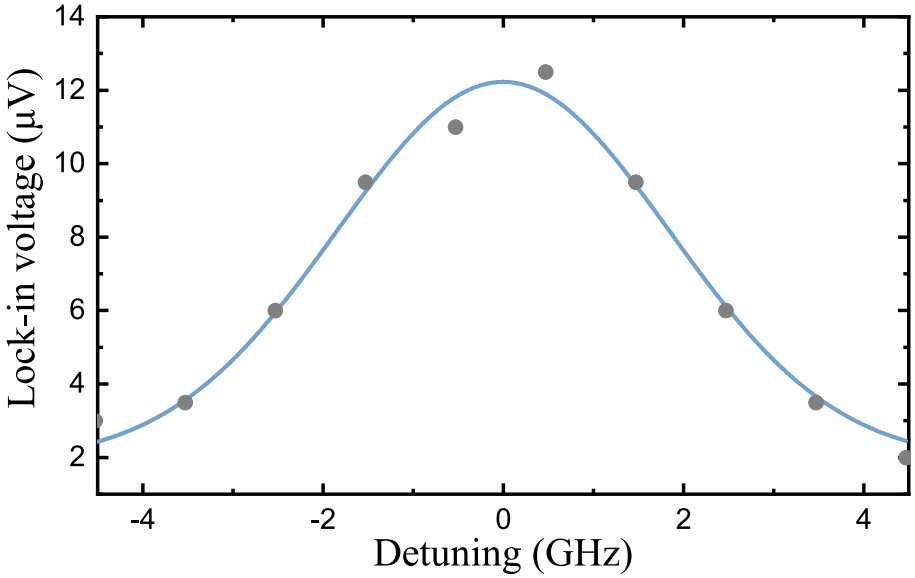

Fig. 4.21 : Lock-in voltage measuring the resonant absorption of photons on the $^3F_3(0) \leftrightarrow {}^1D_2(0)$ transition conditioned on a strong resonant control field applied to the $^3H_4(0) \leftrightarrow {}^3F_3(0)$. Here, the x-axis refers to the detuning of the telecom laser which is scanned while the tapered amplifier is kept on resonance.

feature can be observed. Although off-resonant two-photon absorption was observed in fluorescence configuration, the contrast was too low for it to be detected directly with a weak signal beam.

The set of preliminary characterisations provided in this section are the first step towards a proof-of-principle implementation of the ORCA protocol in Pr^{3+}:Y_2SiO_5. We successfully demonstrated off-resonant two photon absorption on the $^3H_4(0) \leftrightarrow {}^3F_3(0)$ at 1550 nm and $^3F_3(0) \leftrightarrow {}^1D_2(0)$ transition, one of the prerequisites for the scheme to work. However, many issues have yet to be investigated. Crucially, the response of the system in a pulsed regime is unknown as of yet. We hope that saturating the relevant transition will be possible with a pulsed control beam, thereby increasing the two-photon absorption contrast with respect to a fully CW setup. The lack of pulsed lasers has also prevented further spectroscopy of the system, namely obtaining T_1 and T_2 measurements via photon echo experiments. Current experimental efforts, running outside of the scope of this thesis, focus on a more in-depth characterisation of the system followed by the absorption of weak coherent pulses at telecom wavelengths, i.e. the read-in part of the ORCA memory protocol. This scheme will then be combined

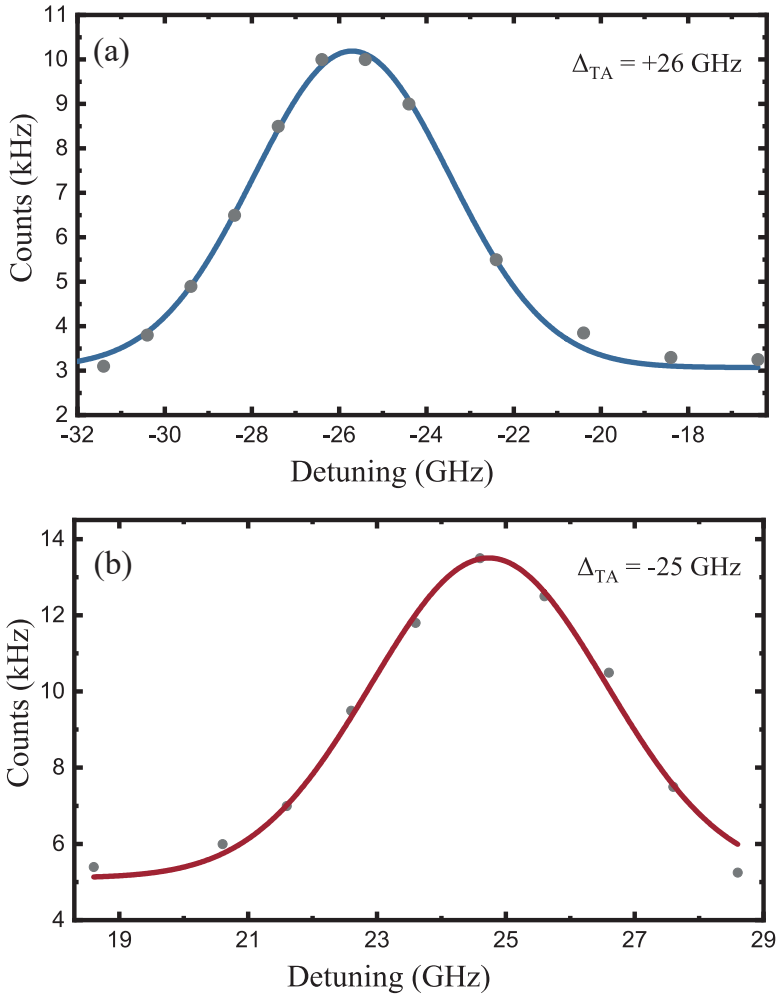

Fig. 4.22 : Fluorescence emission on the $^1D_2(0) \rightarrow^3 H_4(0)$ signalling off-resonant two-photon absorption on the $^3H_4(0) \leftrightarrow^3 F_3(0) \leftrightarrow {}^1D_2(0)$ transition. The x-axis refers to the detuning of the telecom laser. This trace is taken for 50 mW of optical power at 995 nm and 1 W at 1550 nm.

with the AFC protocol realised in section 4.1 in order to allow the observation of a readout pulse.

In the following chapter, we focus on an alternative platform for the implementation of a broadband AFC protocol, in the form of an ensemble of diamond nitrogen-vacancy centres.

Chapter 5

Optical properties of the nitrogen-vacancy centre in diamond

In this chapter, we provide a brief introduction to one of the most extensively researched solid-state quantum platforms: the nitrogen-vacancy (NV) colour centre in diamond. We first consider how the physical nature of the defect defines its energy level structure. The photoluminescence spectrum of the defect is analysed, shedding light on the various broadening mechanisms present in the system. We also review the optical, spin and charge state dynamics of the defect and present some techniques commonly used to control theses degrees of freedom. The material presented in this chapter is inspired by reference [173], in which a much more detailed review of the NV centre can be found.

Diamond is a lattice consisting of carbon atoms where each atom is bound to four neighbours forming a tetrahedron [174]. Both natural and synthetic crystals can contain irregularities known as point defects, where a carbon atom can be missing from a site (vacancy) or another atomic species is grafted into the lattice structure. Some defects cause local alterations in the crystal, thus modifying its optical properties and are referred to as colour centres [175]. Many colour centres in diamond are optically active and have been actively studied over the past decades. A more comprehensive overview of impurity-based defects in diamond can be found in reference[176, 177]. Diamond is a particularly attractive material for the optical study of point defects due to its large bandgap ($\Delta E \sim 5.5eV$) making it transparent across a very large frequency window [178].

In this chapter, we focus on a particular flavour of defect known as the nitrogen-vacancy colour centre. It is composed of a substitutional nitrogen atom and an adjacent vacancy, and can be aligned along any of the four equivalent $\langle 111 \rangle$ orientations of the

diamond lattice [179]. That is, given a vacancy at any site in the crystal, a nitrogen atom can substitute for any of the vertices of the tetrahedron formed by the adjacent sites to form an NV centre. The symmetry axis of the defect is defined by the direction running through both the nitrogen atom and the vacancy. The NV centre receives an electron from each carbon and two from the nitrogen atom. One more can be captured from a nearby impurity such as substitutional nitrogen for a total of six, which influences the charge state of the defect. It is most often found in one of two possible charge states, either negatively charged (NV^-) or neutral (NV^0) [180]. The positive state, NV^+ also exists but is rarely observed as it forms in negligible populations in nitrogen-rich diamond without additional doping or electric fields, and is also not optically active [181, 182]. As the two more common charge states have different electronic structure, their optical and spin properties differ [183]. Throughout this chapter, we focus on the negative charge state and unless stated otherwise NV will refer to NV^-.

Colour centres in diamond behave essentially as single molecule-like quantum emitters trapped within the diamond lattice. As a result, they have garnered much attention as potential solid-state platforms for the implementation of quantum information protocols [173]. The NV centre is by and large the most widely studied defects for this purpose, although over the past decade colour centres based on group IV defects such as the silicon-vacancy (SiV) and the Germanium Vacancy (GeV) have also seen a significant increase in popularity [184, 185]. This avenue of research has led to many impressive experimental demonstrations spanning from magnetometry [186] to quantum information science [187, 188].

5.1 Energy level structure

The energy level structure of the NV centre has been determined over the course of many years of research, through the combined use of experimental and theoretical methods. A full account of these efforts is beyond the scope of the thesis, and in this section we will briefly summarise some aspects relevant to the work presented later on. Detailed information on the structure of the NV centre can readily be found in references [179, 189].

5.1.1 Electronic structure

The presence of a defect in the diamond lattice breaks the symmetry of the crystal. As a result, in the region of interest, the wavefunction of the electrons is no more well-described by Bloch states. This leads to the emergence of localised electronic states in the vicinity of the defect. In the case of the NV centre, the presence of a vacancy causes electrons from the adjacent atoms to be unpaired. These electrons are localised to the vacancy region and are known as dangling bonds. The negatively charged state of the NV centre has six electrons - one from each carbon atom, two from the nitrogen and one received from a nearby impurity donor [190]. These electrons occupy the molecular orbital states defined by the symmetry of the point defect, invariant only under rotations and reflections [179]. According to ab initio calculations [189], there are four possible single electron orbital states referred to as e_x, e_y, $a_1(1)$, and $a_1(2)$. The e states are degenerate and have higher energy than the a states. As the $a_1(1)$ state is inside the valence band, it is de facto always occupied and the remaining four electrons can be distributed to the remaining states as shown in Fig. 5.2. Filling these states with six electrons defines the total spin of the system as $S = 1$ [173]. When the NV centre is in its ground state the a_1 orbital is filled and the e orbitals share the remaining two electrons. When it is excited, one electron can be promoted from the a_1 to one of the e orbitals.

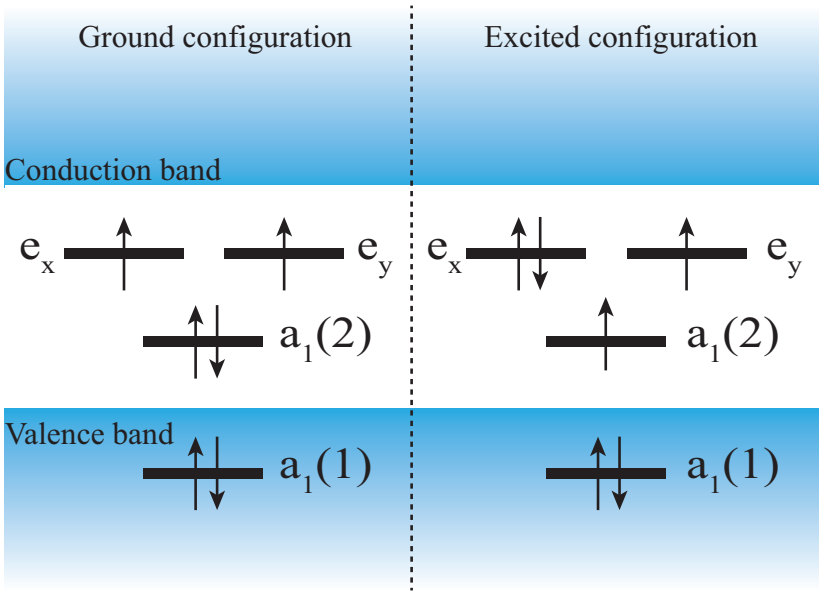

Fig. 5.1 : Depiction of the occupied single electron molecular orbitals by the six electrons in the negative NV centre. The configuration on the left corresponds to the energetic ground state while an excited configuration is shown on the right.

As there are 6 electrons present which can be in any of 8 possible states, the energy structure of the NV^- is given by combinations of the single electron wavefunctions. These multi-electron wavefunctions can also be described equivalently in terms of the two positive remaining holes (adding two electrons to the system would fill all the orbital states). In this picture, the NV is in a lower energy configuration when both holes are in the e state (noted e^2) and has more energy when there is one hole in the a orbital and one in the e (ae). Group theoretical analysis [189] finds that the defect supports one triplet and three singlet states in the e^2 configuration, while the e^2 states consist of two triplets and two singlets. States with the same electronic configuration have the same energy until the Coulomb interaction is factored in and the degeneracy is lifted. On the other hand, the degeneracy inside the triplet states remains intact until spin-orbit and spin-spin interactions are taken into account.

The energy level structure of the system is largely defined by the ordering of the states under the influence of electronic repulsion, shown in Fig. 5.1. The levels are conventionally labelled according to their symmetry (A_1, A_2 or E, defined by the irreducible representation of the NV symmetry), along with a number, added on the left, denoting the number of spin states given by $2S + 1$. The ground state $^3A_2$ is an orbital singlet, spin triplet manifold and thus contains three sublevels. On the other hand, the excited ^3E is an orbital doublet and hence contains six, noted A_1, A_2, E_x, E_y, E_1 and E_2. In summary, the NV centre has a triplet and a singlet subsystem, with a ground and two excited states each. The triplet ground state is separated from the excited state manifold by 1.945 eV (~ 637 nm), while the singlet ground state is separated from the first singlet excited state by 1.19 eV (~ 1042 nm).

5.1.2 Fine structure of the triplet states

The spin-orbit and spin-spin interactions then lift the degeneracy between the triplet states according to their orbital angular momentum and spin components respectively. The triplet ground state have zero angular momentum due to the nature of its orbital state [173] and hence does not experience any shifts imparted by the spin-orbit interaction. The spin-spin interaction splits the $m_s = 0$ and the $m_s = \pm 1$ ground states by 2.88 GHz.

The six excited sub-states have finite angular momentum and thus experience both interactions leading to more complex structure [191, 192]. The spin-orbit separates the sublevels according to their total angular momentum, leading to three pairs (A_1, A_2), (E_x, E_y), and (E_1, E_2) split by 5.5 GHz from each other [193]. Similarly, the spin-spin

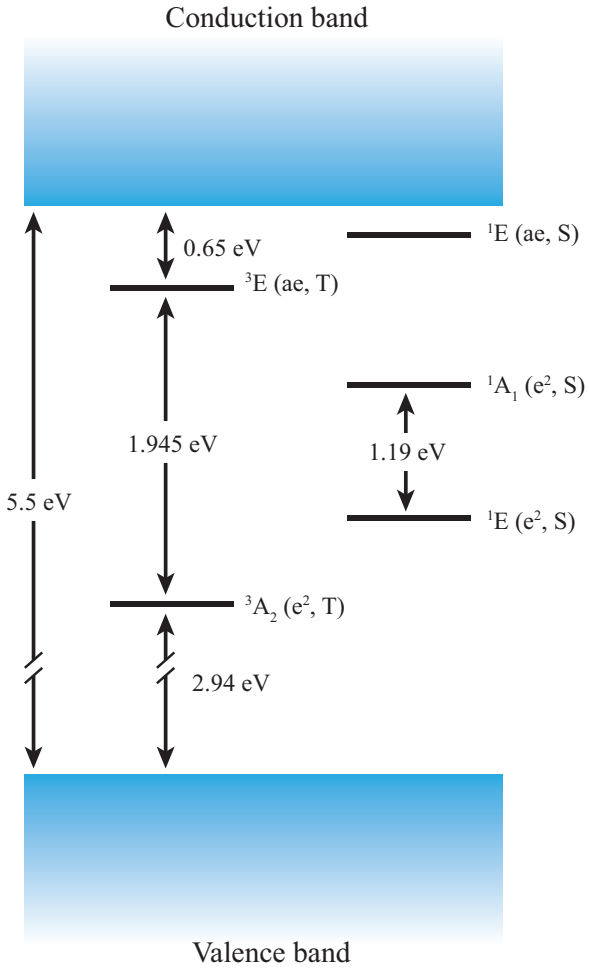

Fig. 5.2 : Energy level structure of the NV centre as defined by Coulomb repulsion. The states are labelled according to their orbital symmetry. The occupations of the molecular orbitals are noted in parentheses in terms of the equivalent holes. The spin nature of each level is also provided, with triplets labelled T and singlets as S

interaction shifts states depending on their total spin. The non-zero spin-states (A_1, A_2,E_1, E_2) are shifted up by $\sim 0.47\,\text{GHz}$ while the E_x and E_y with zero spin are shifted down by $\sim 0.94\,\text{GHz}$ [194]. The A_1 and A_2 states are further split apart by $\sim 3.3\,\text{GHz}$ [193]. Overall, this leads to pairs of E states that are fairly close together, while the A states are further apart with the A_2 state in particular being fairly well isolated energy-wise, as shown in Fig. 5.3.

The ground and excited manifolds are linked by optical transitions which obey selection rules conserving spin and total orbital angular momentum [195]. These transitions are summarised in table 5.1. Consequently, there is no spin-mixing in the system if only the triplets are considered. The spin can however be flipped via

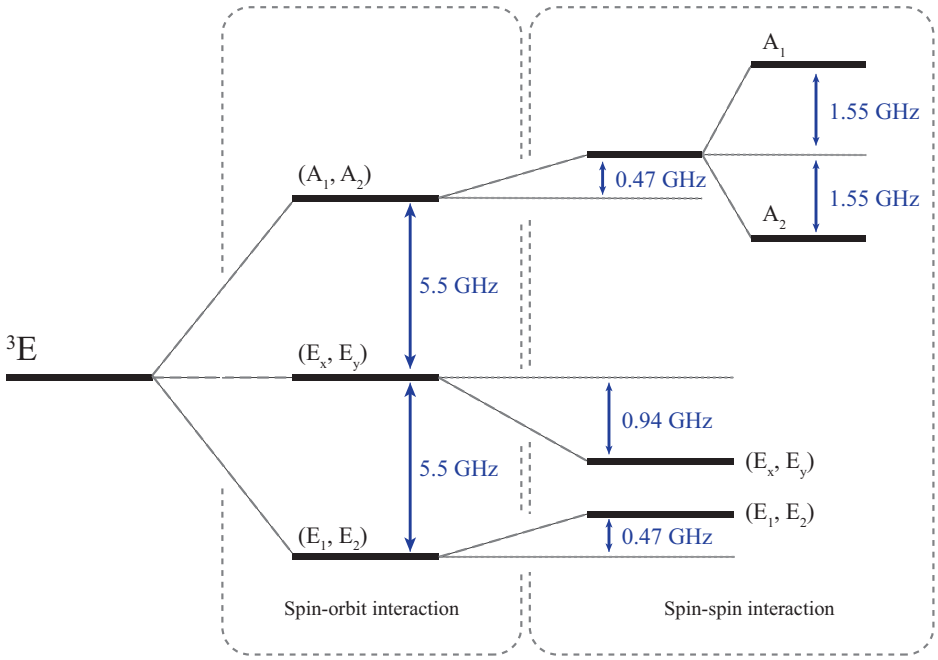

Fig. 5.3 : Schematic of the NV ^3E excited state fine structure, including the effects of the the spin-orbit and spin-spin interactions.

non-radiative transitions to the singlet states which will be detailed further in the chapter. This also means that there exists no non-degenerate lambda-system in the NV energy level structure under zero-field conditions.

g/e	A_1	A_2	E_1	E_2	E_x	E_y
$^3A_{2,-1}$	σ_+	σ_+	σ_-	σ_-		
$^3A_{2,0}$					y	x
$^3A_{2,+1}$	σ_-	σ_-	σ_+	σ_+		

Table 5.1 : Summary of the selection rules for the optical transitions between the ground and excited triplet states. x and y refer to orthogonal linear polarisations, and the circular polarisations are defined as $\sigma_\pm = x \pm iy$

5.1.3 Strain and external magnetic fields

The influence of external fields can also significantly influence the level structure of the NV centre. These effects are what form the basis of magnetic field and temperature sensing schemes with NV centres [196, 197]. None of the experiments presented in this

work require their application and we will thus only mention these effects in passing, but more detail can readily be found in references [198] and [193].

Strain in the diamond lattice affects the local electromagnetic field experienced by the NV and in particular, splits the degeneracy and induces mixing between the e_x and e_y single-electron orbitals. This separates the excited ^3E manifold into two sets of three states which can be split by several GHz in the limit of high strain [173]. On the other hand, the ground state triplet is protected from crystal field induced-effects to first order due to the nature of its electronic configuration and does not experience any noticeable shifts. The mixing of the orbital wavefunctions induces mixing of energy levels in the excited state fine structure. Under specific strain conditions, the transitions can lose their spin-preserving properties and fully allowed optically induced spin-flips can be observed [193]

The application of an external magnetic field splits the degenerate $m_s = -1$ and $m_s = +1$ states via the Zeeman effect. The states with non-zero total spin are shifted in frequency by a magnitude dependent on the projection of the field onto the NV symmetry axis [198].

5.2 Spectral properties

Having elucidated the basic energy level structure of the NV centre, we now have a basic skeleton to work upon towards understanding its physical behaviour. Unlike single atoms in vacuum, colour centres in diamond interact with the crystalline host matrix. This heavily affects their spectral properties, and conversely studying the spectrum of a defect can reveal much information about its internal dynamics. In this section we outline the main broadening mechanisms present in the NV in order to shed some light onto the optical spectrum of the defect.

5.2.1 Optical broadening mechanisms

The excited states of the NV centre experience decoherence mechanisms which define the *homogeneous* linewidths of their transitions Γ_h. As was seen previously in the context of rare-earth ions (see section 3), the linewidth of a single emitter is given by

$$\Gamma_h = \frac{1}{2T_1} + \frac{1}{T_2} = \frac{1}{T_2^*}, \tag{5.1}$$

where T_1 represents population decay, T_2 the characteristic timescale of processes leading to pure dephasing, and T_2^* the overall decoherence time. In particular, T_1 includes both purely optical channels as well as decay involving by non-radiative processes.

In the case of diamond colour centres, non-radiative processes are often caused by phonon-mediated mechanisms. Phonons are quantised excitations of the vibrational modes supported by the diamond lattice. These vibrations can couple to the orbital states of the NV centre leading to effects which are absent from isolated atoms trapped in free space [199].

Photons can interact with an optical transition even far away from resonance via the creation or destruction of phonons in the lattice. For example, the defect can be excited by the absorption of a blue-detuned photon or emit red-detuned photons aided by the subsequent creation of a lattice phonon. This can be seen as optical excitation altering the electronic wavefunction of the defect, thereby affecting the surrounding lattice atoms which relax by creating a lattice vibration. The converse process, where existing vibrations in the lattice provide the missing energy exists at room temperature but is typically suppressed in cryogenically cooled samples. There are thus two types of optical transitions in the system, depending on whether an exchange of phonons is involved or not. This distinction leads to two features in the spectrum of the NV centre (see Fig. 5.4) - a narrow peak on resonance with the native electronic transition (known as zero-phonon line or ZPL) and phonon sidebands (PSB) at both higher and lower frequencies corresponding to the emission of photons at different frequencies aided by the destruction or creation of a lattice vibration. In the following, ZPL will refer to the triplet optical transition at 637 nm unless stated otherwise.

The zero-phonon line of the NV centre itself is also affected by phonons through Raman scattering events and the dynamic Jahn-Teller effect (DJT) [200]. The DJT effect is an orbital phenomenon whereby phonons can couple orbitally degenerate energy levels. This results in a rapid exchange of population between orbitally degenerate levels in the ^3E manifold and is associated with dephasing of the excited states. The defect can also interact with lattice vibrations through a two-phonon Raman scattering process, which is another source of dephasing. Both of these phenomena lead to a sizeable broadening of the optical transition associated with rapid dephasing of both the singlet and triplet excited states of the NV centre. At cryogenic temperatures the phonon population in the lattice is minimised, which leads to the elimination of processes relying on vibrations already existing in the lattice. Linewidth broadening

induced by both Raman and DJT effects scale steeply with temperature T, exhibiting a dependence of T^7 and T^5 respectively [201]. At room temperature, the fine structure of the excited state triplets cannot be fully resolved and only three levels are observed. This is due to phonon-mediated processes averaging out the orbital components of the excited state [202]. Optically excited population is thus distributed equally over all states with the same spin projection. Phonons only couple to the orbital part of a state and thus the spin portion is left intact, leading to the observation of only states with different spin projections [173, 193].

The NV centre is very sensitive to electric fields which lead to shifts in the energy level of the excited states. Fluctuating charges in the vicinity of the defect can thus lead to jitter of the ZPL central frequency which translates to an equivalent dephasing of the excited state and homogeneous broadening of the line. Ionisation of nearby defects are thought [203] to contribute significantly to this effect, which is known as spectral diffusion.

Strain and impurity concentrations are rarely homogeneous over the entirety of a diamond crystal. As a result, NV centres in different locations experience different amounts of strain and electromagnetic fields, which shift their resonant frequencies accordingly. This phenomenon, known as inhomogeneous broadening, distributes the zero-phonon lines of the defects in any given ensemble across a potentially wide range of frequencies. The resulting inhomogeneous broadened line is apparent when scanning the absorption profile of an ensemble of NV centres, and can reach up to hundreds of GHz, orders of magnitude wider than the homogeneous linewidth of the triplet optical transitions. As inhomogeneous broadening is caused by spatial variations in the local electromagnetic field, the associated linewidth is highly dependent on the density of defects and impurities in the sample [204, 205]. As such, sparse ensembles tend to exhibit narrower inhomogeneous widths.

5.2.2 Spectrum of the NV^- centre

The fluorescence spectrum of the NV centre is most often recorded by exciting the defect off-resonantly using an optical field at a wavelength shorter than that of the NV^0 zero-phonon line. The Franck-Condon principle states that the excitation of electrons by an optical field occurs much faster than the creation or annihilation of photons arising from the relaxation of surrounding atoms [206, 207]. Consequently, the defect is first excited into a state where both the vibrational and electronic degrees of freedom are excited. The system relaxes first to the vibrational ground state due to the longer

electronic excited state lifetime. The electronic state decays preferentially into the higher vibrational states of the electronic ground state which then decays fast to the lowest energy configuration of the system [208]. The excitation nevertheless has a finite chance of decaying purely optically from the vibrational ground state of the excited electronic state to the overall ground state of the system. This process corresponds to emission into the zero-phonon line.

This type of excitation thus leads to fluorescence emission into both the ZPL and the PSB allowing the observation of the full spectrum of the defect. A typical spectrum is provided in Fig. 5.4, showing zero-phonon lines at 637 nm and 575 nm for the NV^- and NV^0 respectively. The associated phonon sidebands are also clearly visible, extending far into the near-infrared. Although not included in the figure, the NV^- singlet also has similar associated features around 1042 nm. From this spectrum, the relative proportion of the emission into the ZPL can be estimated, given by the Debye-Waller (DW) factor [209]:

$$\alpha = \frac{I_{\mathrm{ZPL}}}{I_{\mathrm{ZPL}} + I_{\mathrm{PSB}}}, \tag{5.2}$$

where $I_{\mathrm{ZPL(PSB)}}$ is the total intensity emitted into the ZPL(PSB). The NV^- Debye-Waller factor is low, with $\alpha \sim 0.04$, meaning that although the defect is quite bright, most of the light emitted is found in the sideband [210–212]. The absorption spectrum of NV^- is very similar to its photoluminescent spectrum, and the DW factor holds when considering absorption into the ZPL as well. This is perhaps the main limit factor with respect to using the NV centre as an optical qubit. The Debye-Waller factor is not limited by phonons already existing in the lattice, and thus does not benefit from cryogenic cooling.

The zero-phonon line is considerably broadened by phonon scattering mechanisms at room temperature, up to several THz [213]. Cryogenically cooling the sample will suppress these effects, leading to a linewidth much closer to the decay-limited value of $\frac{1}{T_{\mathrm{rad}}} \sim 16\,\mathrm{MHz}$ where T_{rad} is the optical decay rate of the NV excited state into the zero-phonon line [214, 215]. This nevertheless depends on the magnitude spectral diffusion which can sometimes reach several hundreds of MHz [212].

5.3 Optical and spin dynamics

The reason the NV centre has been historically so favoured for the implementation of quantum protocols lies in the unique interplay between its optical and spin properties.

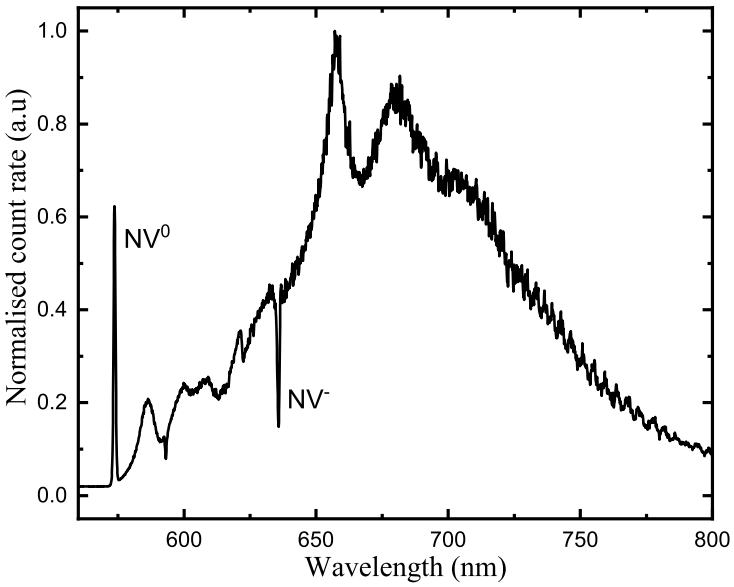

Fig. 5.4 Fluorescence spectrum of the NV centre as recorded from illumination at 532 nm at 4 K. The zero-phonon lines of both the neutral and negative charge states are visible at 575 nm and 637 nm respectively. The NV^- ZPL is seen as a dip rather than a peak due to high resonant re-absorption in the sample. Wide overalapping phonon sidebands are observed for both defects, extending into the near-infrared. Data collected from the sample used in Chap. 6.

Optical excitation can affect the spin state of the defect via a so-called inter-system crossing (ISC) [216] linking the triplet and singlet subsystems as shown in Fig. 5.5. States in the excited triplet manifold can decay non-radiatively to the ^1E singlet state via a non-radiative channel. Crucially, the rate at which this process occurs is highly spin-dependent, with the states with non-zero spin decaying into the singlet almost 7 times faster than their counterpart [217]. The excited singlet then decays to the $^1A_1$ ground state on a picosecond timescale before being transferred back to the triplet system via another crossing. The relaxation rates from the singlet to the triplet are not spin dependent and do not affect the relative spin populations. This phenomenon implies that if the defect is continually excited above-band with, say, light at 532 nm, the population will continually cycle between the two subsystems and eventually accumulate into the $m_s = 0$ spin state [218, 173].

This technique has a slew of applications, the first and foremost being a simple way of initialising the spin state of the NV centre. While ground state spin relaxation

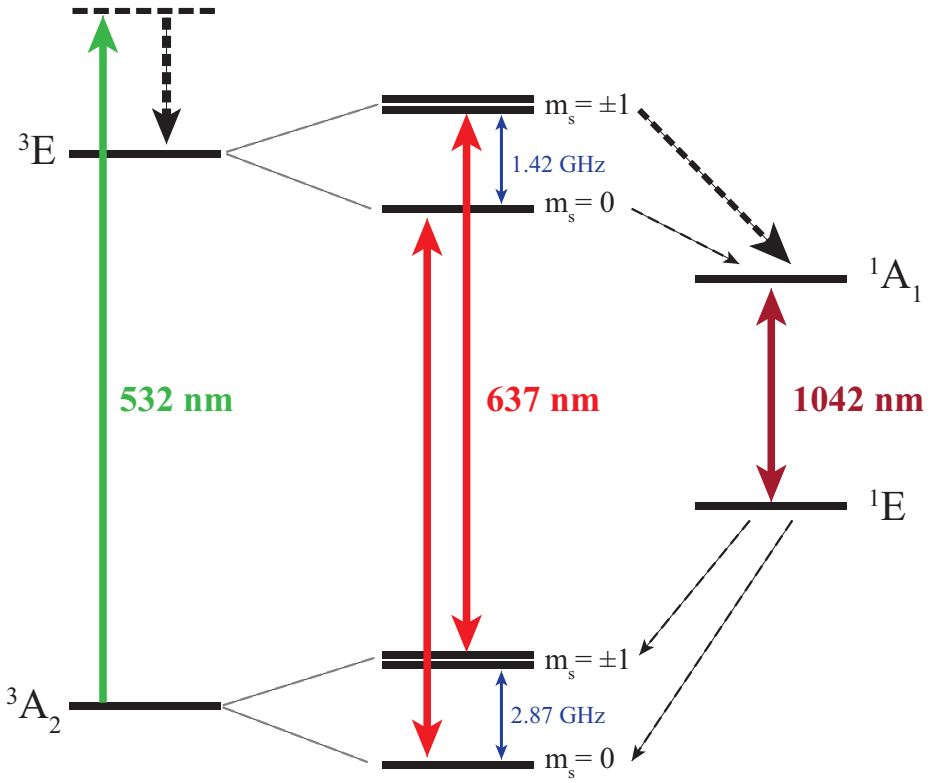

Fig. 5.5 : Schematic of the intersystem crossing present in the NV centre structure. Preferential decay of the $m_s = \pm 1$ spin states into the singlet $^1A_1$ state leads to spin polarisation of the defect under off-resonant excitation. The vibrational bands leading to the emergence of the phonon sideband are omitted in this diagram.

timescales do limit the achievable spin polarization, it is not the main factor as the defect features long spin lifetimes, with recorded values of $T_{1,spin}$ ranging from milliseconds at room temperature to seconds at 4K [216]. This is due to the main phonon-mediated mechanisms coupling the spin states being minimised at cryogenic temperatures. The spin dephasing time $T_{2,spin}$ depends significantly on the properties of the host crystal, ranging from microseconds in dense samples [219, 220] expected to contain many impurities to milliseconds for isotopically engineered diamond [221]. The coherence time is mainly limited by interactions with neighbouring defects such as substitutional nitrogen atoms in the diamond lattice [205].

The optically-induced spin dynamics also form the basis for an easily implemented method to read out the spin-state of the defect [222]. As mentioned previously, the defect emits fluorescence in a wide band when excited off-resonantly with an optical field. As the $m_s = \pm 1$ states in the excited triplet manifold have a high chance of relaxing to the singlet state instead of optically decaying to the triplet ground level,

they emit significantly less fluorescence than the zero spin state in both the ZPL and the phonon-sideband. This leads to a sizeable contrast of $\sim 30\%$ [222, 204] between the fluorescence levels detected from each spin state in single NVs. A simple, yet reliable scheme allowing optical readout of the spin state can thus be constructed via this effect, with the measurement time limited by the spin resetting effect mentioned above [223, 204]. While this method does also lead to fluorescence from the NV^0 state, this portion can be selectively filtered out due to a difference in the emission spectra [224].

At zero magnetic field, the $m_s = 0$ and $m_s = \pm 1$ ground states are split by 2.88 GHz, a frequency which is accessible to microwave fields. Microwave pulses can be applied to address and control the spin state of the ground level, forming a robust two-level system which can be used as a qubit for quantum information protocols [188]. The dependence of the ground state system to external magnetic fields has also led to the development of many magnetometry schemes employing the NV centre as a highly sensitive atom-sized probe [225, 196].

The defect can also be excited with light resonant with the NV^- zero-phonon line [226]. In this case, the dynamics are given by the transitions described in table 5.1. The selection rules are largely spin-preserving, leading to the $m_s = 0$ ground to excited transition forming a good approximation to a cycling transition.

5.4 Charge dynamics

The charge state of the NV centre is also heavily affected by optical fields, which can be used to cycle between the its negative and neutral states. Comprehensive insight into the charge state dynamics of the NV can be found in a study by Aslam *et al.* [224]. The ionisation process, triggering the conversion of NV^- to NV^0 requires an energy of 2.6 eV from the triplet ground state $^3A_2$, corresponding to optical excitation at 478 nm. The gap separating the excited triplet state of NV^- to the conduction band is much smaller, and hence ionisation can also be triggered by a two-photon process at longer wavelengths ($478\,\text{nm} \leq \lambda_{exc} \leq 637\,\text{nm}$). In this case, the first photon excites the system into the excited triplet state of NV^- and the subsequent photon causes the ionisation of the defect into the NV^0. The recombination process requires NV^0 to capture an electron from the valence band in order to revert to the negative charge state. This mechanism is conditional on NV^0 to be in an excited electronic configuration and thus occurs rarely when the system is at rest. As a result, the NV^0 was first studied as a metastable dark state of the defect [227] before being accurately identified [224]. The

recombination process can be stimulated via optical excitation of the neutral charge state at a wavelength shorter than its zero-phonon line at 575 nm. The mechanisms leading to optically-induced charge state conversion are summarised in Fig. 5.6.

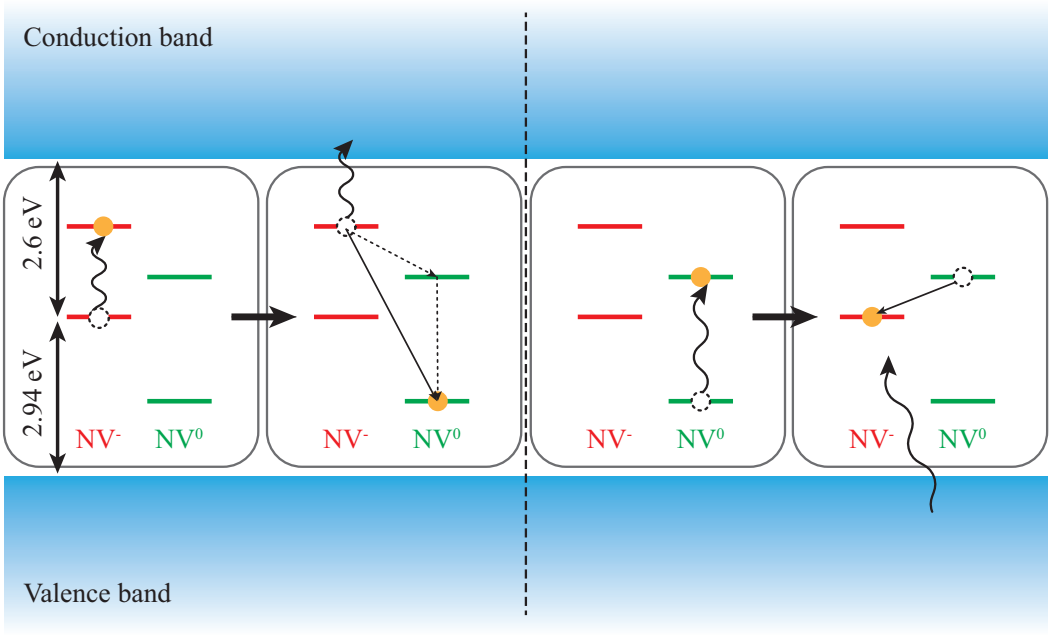

Fig. 5.6 : Optically-induced charge state conversion mechanisms in the NV centre. Ionisation is shown on the left: 1) a photon is absorbed on the NV^- ZPL at 637 nm, exciting the defect into its ^3E state. 2) A second photon absorbed at the same wavelength provides sufficient energy to promote an electron to the conduction band, ionising NV^- to NV^0. The recombination process is shown on the right: 3) a photon is absorbed on the NV^0 ZPL at 575 nm, exciting the defect. 4) In this configuration, and electron can be captured from the valence band, prompting the conversion back to NV^-.

Ionisation only requires enough energy to excite an electron into the conduction band, and is thus a relatively broadband process. This is also the case for the recombination mechanism which relies only on the optical excitation of the neutral charge state. Both processes occur at rates which depend on the excitation wavelength and power and following the absorption cross-section of each charge state. If the defect is illuminated at 532 nm, both mechanisms are enabled, leading to continuous cycling between the charge states with an average NV^- population of 70% (with the rest being in the neutral state), close to the optimum over all excitation wavelengths. This property can be used to reset the charge state of an ensemble of NV centers to a known equilibrium value. On the other hand, continuous excitation at wavelengths longer than 575 nm

leads to a much lower NV^- population $p_- \lesssim 10\%$ as the defect is trapped in the NV^0 state. The wavelength dependence of p_- is illustrated in Fig. 5.7.

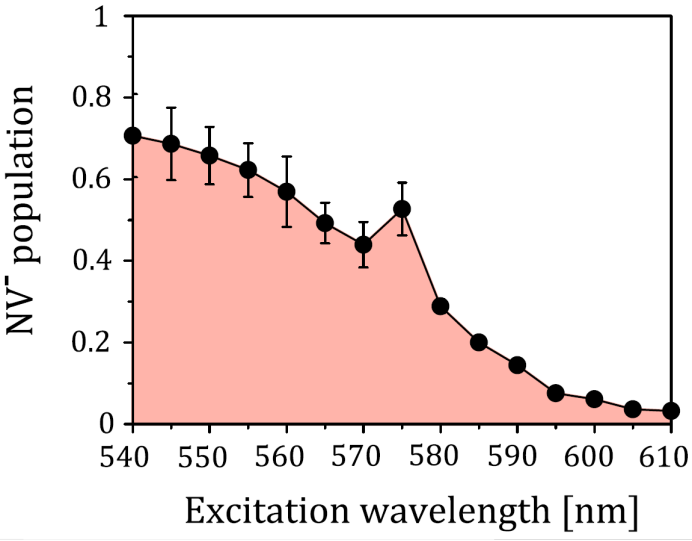

Fig. 5.7 : Probability of the defect of being in the negatively charged state under illumination at various wavelengths. The NV^- population is much lower for longer excitation wavelengths where the recombination process is suppressed. The peak at 575 nm is due to resonant addressing of the NV^0 ZPL leading increased excitation of the neutral charge state. Figure from Ref.[224]

Finally, at the wavelengths where optical ionisation of the defect is a two-photon process, the ionisation rate follows a quadratic dependence on the excitation intensity. This relation transitions to a linear regime as the excitation wavelength approaches 470 nm.

5.5 Summary

In this chapter, we have provided an overview of the optical properties of the NV centre and how they arise from the defect's electronic structure. The spin dynamics induced by optical excitation of its negatively charged state were established and linked to some commonly used experimental techniques. The system is particularly attractive as it can be initialised and readout using simple methods. Overall, these properties have consolidated the NV as a promising solid-state platform which has enabled many protocols from magnetometry [228] and remote entanglement [187] to an experimental demonstration of quantum thermodynamic signatures [229]. This short

review will underpin work presented further in this thesis which focuses on light-matter interactions with ensembles of NV centres.

Chapter 6

Spectral hole burning of an atomic frequency comb in ensembles of diamond NV centres

As we have seen in Chapter 2, the development of quantum memories is a crucial step towards building functional quantum networks. Within the many existing protocols for photonic quantum memories in atomic ensembles, the atomic frequency comb protocol (see section 2.3.3) stands out as especially promising. As it relies on inhomogeneous broadening as resource it provides an avenue for the realisation of photon storage in solid-state media where individual emitters can experience large shifts due to crystal fields in the host lattice. The AFC protocol has supported the storage and retrieval of single photons in ensembles of rare-earth ions doped into solid-state materials such as praseodymium-doped yttrium orthosilicate (Pr^{3+}:Y_2SiO_5) [164]. Most full implementations of the protocol rely on mapping light to a long-lived ground-state coherence. However, the performance of quantum memories based on rare-earth ensembles is often limited by the narrow splitting (∼MHz) between the hyperfine ground states of the ions. This in turn reduces the acceptance bandwidth of the memory, thereby setting a bound on the time-bandwidth product and restricting the choice of compatible single photon sources.

The nitrogen-vacancy (NV) colour centre in diamond (introduced in chapter 5) is a point defect in the diamond lattice and one of the most widely studied solid-state quantum emitters. Due to its large ($\sim 2.8\,\mathrm{GHz}$ at zero field) ground state splitting, it stands as an alternative candidate for the implementation of a quantum memory based on the atomic frequency comb protocol. Efficient spectral hole burning techniques

are required in order to prepare the spectral profile which the AFC technique relies on. There are relatively few studies of hole burning in ensembles of NV centers. Past implementations focus on shaping inhomogeneously broadened transitions by selectively pumping population in certain spin states [230]. This method is similar to the techniques currently employed in rare-earth ions [135], and is intrinsically limited by the ground state relaxation time of the emitter.

In this Chapter, we devise and investigate a novel approach to spectral hole burning in ensembles of NV centres. This method, based on ionisation of the negatively charge NV centre to its neutral charge state, is then implemented in order to to demonstrate the first realisation of an atomic frequency comb in this system. We first outline the technique and propose a road map towards an atomic frequency comb memory in NV ensembles. The experimental setup used in our experiments is then presented. This is followed by a characterisation of ionisation dynamics in the sample and results showing the AFC profile. All experiments in this chapter were performed by myself with the assistance of J. N. Becker and P. M. Ledingham.

6.1 Concept

We wish to implement the AFC protocol on the zero-phonon line of an ensemble of NV centres. In order to do so, the transition, which can be inhomogeneously broadened by hundreds of GHz, must be shaped in the spectral domain into series of regularly spaced peak characteristic of the atomic frequency comb. Then, a single photon absorbed resonantly on the transition can be mapped onto a collective excitation of the ensemble and is re-emitted via a rephasing echo at a later time defined by the properties of the comb (see section 2.3.3).

In most cases, the nitrogen-vacancy centre can be either negatively charged (NV^-) or electrically neutral (NV^0). The NV^- state can be converted to NV^0 via an ionisation process triggered by two-photon absorption at 637 nm (see section 5.4. This can be reversed by a recombination process requiring the excitation of the NV^0 state. As the zero-phonon line of the neutral state is located at 575 nm, neutrally charged centres appear 'dark' at the NV^- resonance frequency [224, 231]. Furthermore, as excitation of the NV^- ZPL does not excite the NV^0 state, the recombination process is typically suppressed. One possible approach to hole burning in NV^- centres can thus be to selectively ionise emitters at desired frequencies to another charge state. The ensemble would then be transparent at the frequencies where defects have been ionised and the

inhomogeneous line shaped arbitrarily. An advantage of this technique is that the hole lifetime would only be limited by the potentially slow charge dynamics of the ensemble. In this chapter, we demonstrate an implementation of this technique using a pulsed laser, consisting of a series of evenly spaced peaks in the spectral domain, applied on resonance with the NV centre zero-phonon line.

Absorption of a single photon on the transition and its retrieval via the subsequent rephasing echo does not constitute a full on-demand quantum memory . As the timing of the echo cannot be controlled, the protocol is closer to a photonic delay-line. Long-term storage of the excitation is typically achieved via a transfer to a long-lived ground state coherence [96]. This approach requires a transition to another metastable ground state as can be found in a lambda-type energy level structure. Optical transitions between spin states in the NV centre are forbidden by selection rules or at best only weakly allowed due to strain-induced spin mixing. Nevertheless, a lambda-structure can be obtained via that application of an external magnetic field splitting the $m_s = \pm 1$ hyperfine ground state states by up to several GHz [226]. Each of these states is linked to the excited state manifold by orthogonally polarised optical transitions and can thus be addressed separately. Initialisation of the ensemble into the one of the desired $m_s = \pm 1$ levels is achieved by harnessing the inter-system crossing of the NV to pump its population into the $m_s = 0$ spin state (see Chap. 5) and subsequently flipping the spin via the application of a resonant microwave π pulse [232].

6.2 Experimental setup

The experimental setup necessary in order to investigate the hole burning technique described above is composed of three main elements. We distinguish a stage where the laser fields required in the experiment are prepared, one where these beams interact with the ensemble of NV centres and finally a section where the light transmitted through the setup is collected and analysed. In this section we will provide some detail about each of these stages.

6.2.1 Light Sources

Only a single pulsed laser is necessary for this technique to be implemented. We use a Sirah Gropius dye laser system (see Chap. 4), this time replacing the laser gain medium by Rhodamine B. This allows the generation of a train of pulses of $\sim$4 GHz

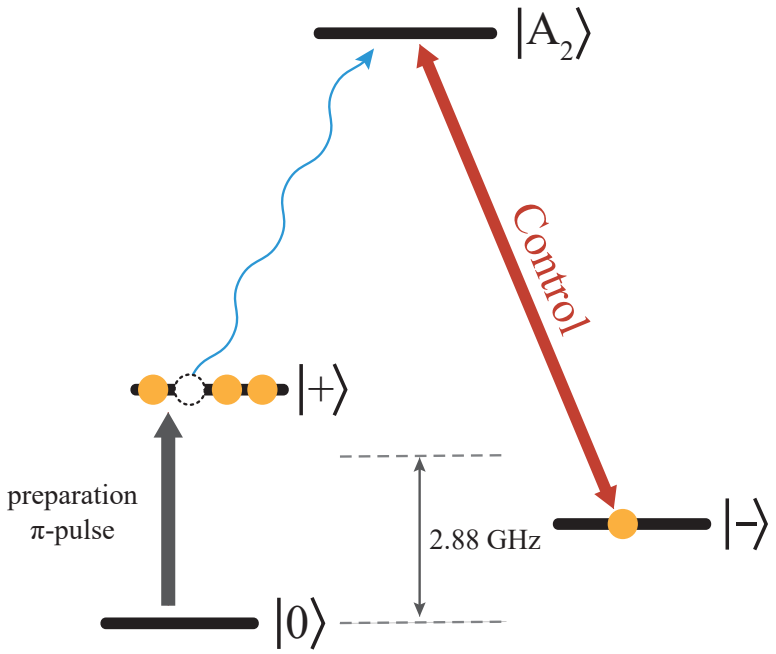

Fig. 6.1 : Diagram of an optically accessible lambda system in the NV centre obtained via the application of an external magnetic field to split the ±1 spin sub-levels.

bandwidth at a 80 MHz repetition rate with 200 mW mean optical power. The central wavelength is widely tunable from 600 nm to 650 nm, giving access to the NV^- ZPL at 637 nm. The spectrum of the pulse train is a frequency comb with peaks separated by 80 MHz, set by the repetition rate of the laser. As was the case with the Pr^{3+}:Y_2SiO_5 experiment, instability in the laser dye jet flow induces fast fluctuations of the laser cavity length and thus cause the laser frequency to jitter, here by ∼40 MHz on a 10 kHz timescale.

The system is tuned onto resonance with the NV centre zero-phonon line at 637 nm. We then separate the main laser output into a strong beam referred to as the 'burn' and a weak 'probe' field. As their names suggest, the burn beam will be responsible for triggering the hole burning process whereas the probe will be used to measure the spectrum of the inhomogeneous transition. The attenuated beam is sent through an acousto-optic modulator (AOM1 in Fig. 6.2) in double-pass configuration. The AOM is driven by an external radio-frequency (RF) driver which sets the modulation frequency. The frequency of the RF drive is modulated by an amplitude of 40 MHz at a rate of 10 kHz using an arbitrary waveform generator. This stage is used to rapidly sweep the beam in frequency at a fast rate in order to remove any existing frequency structure.

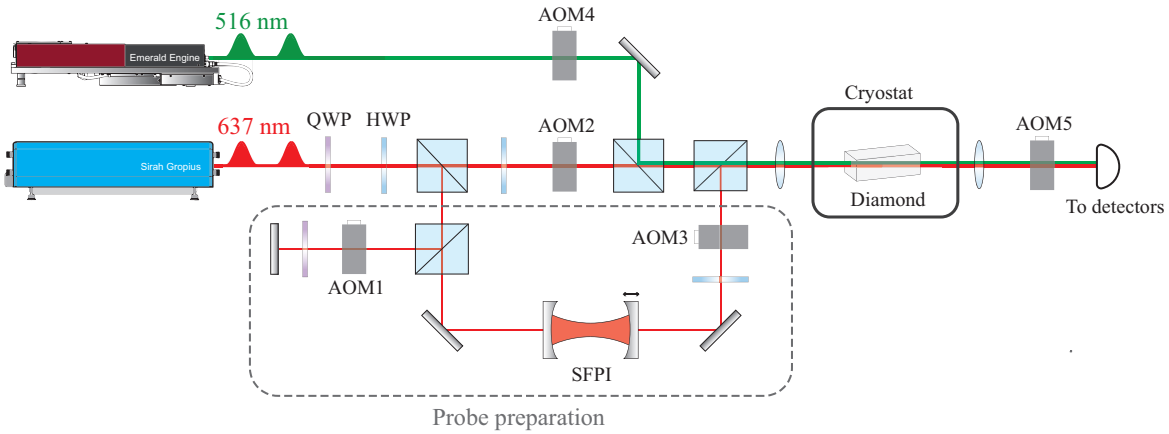

Fig. 6.2 : Setup used for the preparation and probing of an atomic frequency comb in a cryogenically cooled ensemble of NV centres.

Coming out of the AOM stage, the probe thus has a smooth Gaussian spectrum with a 3 GHz width and no distinct peaks or troughs. This profile is filtered down to a width of 1 GHz using a monolithic glass etalon and sent on to a scanning Fabry-Pérot interferometer (FPI, Thorlabs SA200-5B, with 1.5 GHz free spectral range and a finesse of 500). The FPI narrows the probe spectrum further down to a narrow Lorentzian with 7.5 MHz width which can then be scanned by changing the cavity length with a standard piezo driver controlled by the sawtooth signal provided by a Toptica SC110 high-voltage module. The output of this stage is a frequency-tuneable quasi-CW probe beam which can be used for absorption spectroscopy of the atomic transition. The probe is then recombined with the burn beam to which no optical processing is applied beyond polarisation cleaning and control.

The spin and charge states of the NV centre can be initialised via optical above-band excitation [173, 224]. This process is necessary in order to reset the state of the ensemble in between experimental sequences. We use a portion of the Emerald Engine output used to pump the dye laser in order to provide a bright source of light with approximately 40 mW at 516 nm. This so-called 'reset' beam is combined with the burn and probe beams and coupled into fibre before being sent on to the diamond sample. Fibre coupling is crucial for the experiment as it ensures spatial overlap of the burn and probe beams as well as cleaning their spatial modes into a clean Gaussian profile.

The fields can be individually switched on or off with a rise time of ~ 100 ns using AOMs setup in each beam path (AOM2, 3 and 4). The switching set up is controlled by a central delay generator (Stanford Instruments DG635) synchronised to the pulse

train via a trigger signal collected by picking off a small portion of the Emerald Engine output and measuring it with a fast silicon photodiode (Thorlabs DET10A, 1 ns rise time). The FPI scan is also synchronised to the experiment using this same signal.

6.2.2 Cryostat and sample

For this experiment, we use an electron-irradiated type Ib HPHT diamond with dimensions of $2 \times 2 \times 1\text{mm}^3$. The crystal was HPHT treated at 6 GPa and 1600°C after irradiation. The sample contains a high density of NV centres, estimated at ~ 1 ppm. Its facets were not re-polished after the irradiation and annealing process and thus appear quite rough to the eye. The absorption profile of the ensemble ZPL was probed by scanning the dye laser around resonance, revealing a very broad inhomogeneous line with $\Gamma_{\text{inh}} = 320\,\text{GHz}$ shown in Fig. 6.3. On resonance, the ensemble has a significant optical depth ($d = 8$) which is the main reason it was chosen for this study. The photoluminescence spectrum of the sample under illumination at 516 nm is also shown in Fig.5.4, showing the zero-phonon lines and phonon sidebands of both NV charge states. The NV^- ZPL appears as a dip instead of an emission peak due to high resonant re-absorption in the sample.

The NV centre ZPL experiences large homogeneous broadening at room temperature due to phonon-induced dephasing processes. In order to suppress these phenomena, the sample is cooled down to cryogenic temperatures (∼4 K) in a liquid Helium cryostat. We use a closed-cycle helium refrigerator (Oxford Instruments Optistat Dry BL4) with a cooling power of 0.2 W at 4K allowing a thermal stability of 0.1 K. The cold finger is cooled down by the expansion of helium contained within a closed circuit and recycled using a water-cooled compressor (Sumitomo HC-4). Silver paint is used to fix the diamond sample to a sample holder connected to the cold finger in order to ensure thermal contact. The cooling process causes significant vibrations of the cold head (estimated at $\sim 10\,\mu$m) at a rate of 1 Hz defined by the length of the compression cycle.

The sample can be optically accessed via uncoated windows. Light is focused to a waist of $\sim 20\,\mu$m using a $f = 50$ mm focal length plano-convex lens. The transmitted beam is then collimated using another identical lens and sent to the detection stage. As the sample facets are not polished, transmission through the cryostat is quite low ($\sim 10\%$) and the mode profile of the output beam is heavily deformed.

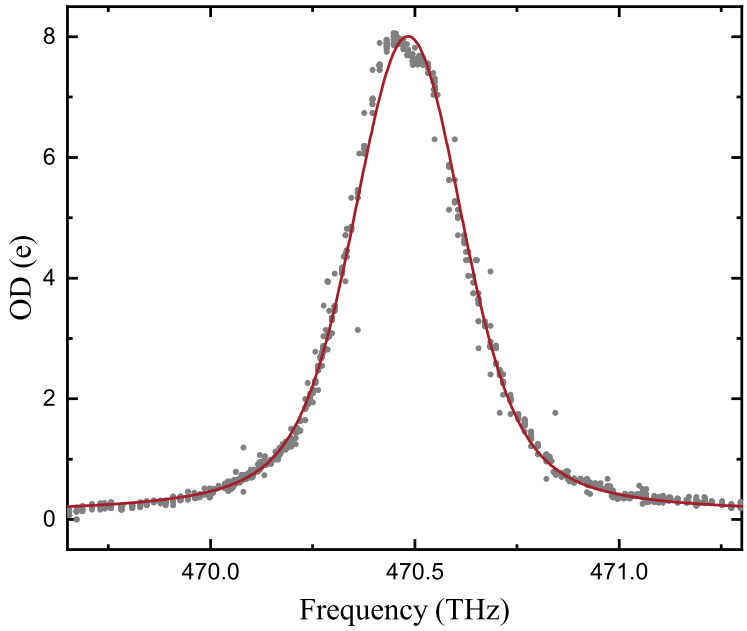

Fig. 6.3 : Absorption spectrum of the ensemble-broadened NV^- zero-phonon line, measured by measuring the transmission of a weak ($P < 1\,\mu W$) probe with width $\Delta\nu_{probe} \sim 4\,GHz$. We record a wide inhomogeneously broadened linewdith $\Gamma_{inh} = 320\,GHz$ with a high resonant optical depth $d = 8$.

6.2.3 Detection and measurement

An array of detectors capable of measuring optical signals at a range of different powers are required from this experiment. The burn and reset beams typically carry tens of milliwatts of power in order to pump the ensemble in a time-efficient way. while the probe beam is attenuated to a weak coherent state and the fluorescence emitted by the ensemble is at the single-photon level. Furthermore, detectors with a relatively fast response are necessary in order to keep up with laser repetition rate.

A silicon fixed-gain biased photodiode (Thorlabs DET10A with 350 MHz bandwidth) is used for measurements on the strong beams. The small area of the detector chip allows for a fast rise time of 1 ns. Of course, this is insufficient to resolve the shape of the pulses but other aspects of the experiment can be accurately monitored such as the rise time of the AOMs used for switching. On the other hand, the probe beam is much weaker and must be measured with a silicon avalanche photodiode (APD - Thorlabs APD110A).

Measurements of the probe with a higher signal-to-noise ratio were achieved by resorting to counting single photons. We use a silicon single-photon APD (SPCM - Excelitas AQRF) with an efficiency of $\sim 65\%$ at 637 nm and 150 Hz dark count rate. The SPCM outputs a digital signal in the form of TTL voltage pulses which are then treated with a fast counting electronics module (Swabian TimeTagger with 3 ps timing resolution and four channels) controlled via software written by myself (MATLAB integrated into Labview). The TimeTagger collects photon arrivals in a user-defined time-bin histogram with a wrap-around period given by an external trigger. This trigger signal can be synchronised to an integer multiple of the laser repetition rate via a delay generator, or to the scanning period of the FPI. The photon-counting setup is also used to measure fluorescence emission from the ensemble.

The single-photon APD chip is easily damaged by optical fields and must thus be protected from the strong beams used in the experiment. This is achieved via an AOM (AOM5) placed in the detection arm of the setup which time-filters the incoming optical signal in such a way that only the probe field is collected on the APD. However, the suppression efficiency of the AOMs used for switching is limited which leads to noise from leakage of the burn and reset beams onto the detector. The noise levels are not high enough to damage the APD itself, and a significant portion can be filtered out with microwave gates set up so as to block the TTL pulses produced by the detector outside of the detection window.

Optical signal analysis is done via two fibre-coupled grating spectrometers included in the setup. The first is a commercial Andor Shamrock device coupled to an Andor iXon CCD camera. Its resolution is limited to ~ 0.07nm but it boasts a wide range spanning the whole visible spectrum and into the NIR. Interfacing is done entirely via the Andor Solis software suite. We also use a home-designed system with a narrower resolution (~ 4.8GHz at 637 nm) built around a 0.5 m long monochromator (Digikrom DK480) in Czerny-Turner design. In this case, the grating (1200 lines/mm) angle is tuned manually so as to image the signal in frequency space onto a CCD camera. Finally, the central frequency of the laser in monitored using a HighFinesse Wavemeter (WS-6).

6.3 Spectral hole burning via ionisation

In order to efficiently shape the spectral density profile of the ensemble, the ionisation process must first be studied. The shape of the transition is given by how the atomic

population is distributed into its possible states. Hole burning is thus a transient process and determining the response of the ionisation rate to different burning powers is necessary in order to define an efficient atomic frequency comb preparation sequence.

6.3.1 Ionisation dynamics

In this section, we present the results of a preliminary investigation of photoionisation dynamics in NV centres. As mentioned in section 5.4, ionisation occurs as a two-photon mechanism under 637 nm illumination, and the recombination process is suppressed for excitation at wavelengths longer than 575 nm. Consequently, exposing an ensemble with an optical field resonant with the the NV^- zero-phonon line for a long-enough time will deplete the negative charge state population. This translates to an increase in the transmission of a resonant probe beam weak enough to not contribute to the process. Throughout the following, any such effect is associated with ionisation in the ensemble. Excitation with light at 516 nm will trigger both ionisation and recombination processes. This effectively cycles the relative charge state populations and resets the state of the system to an equilibrium defined by the associated rates.

We first investigate the ionisation process in the steady-state. The burning beam is applied until the point when the dynamics reach equilibrium and we record the transmission of the probe beam. For this measurement, the probe bypasses the spectral blurring AOM and the FPI so that the spectrum of the burn and probe match. Results are shown in Fig. 6.4, revealing a quadratic dependence on burning power attributed to the two-photon nature of the process. The charge state population ratios are reset via bright 516 illumination in between successive data points.

As a preliminary step, we investigate the amount of green laser power required to fully reset the ensemble between two experimental runs. A pulse sequence consisting of 10 μs of resonant excitation at 0.5 mW average power followed by 90μs at 516 nm is used. The transmission of the red beam is recorded using a single-photon APD. We accumulate counts over a period of one minute during which the pulse sequence is repeated many times.

The resonant transmission at the end of the ionising window is plotted for different values of reset powers in Fig. 6.5. As the 516 nm power increases, less transmitted counts are recorded indicating that the population of the negative charge state is successfully being reinitialised.

We then focus on the dynamics of the ionisation process in order to determine the necessary length and power of the burning pulse. We observe the response of the

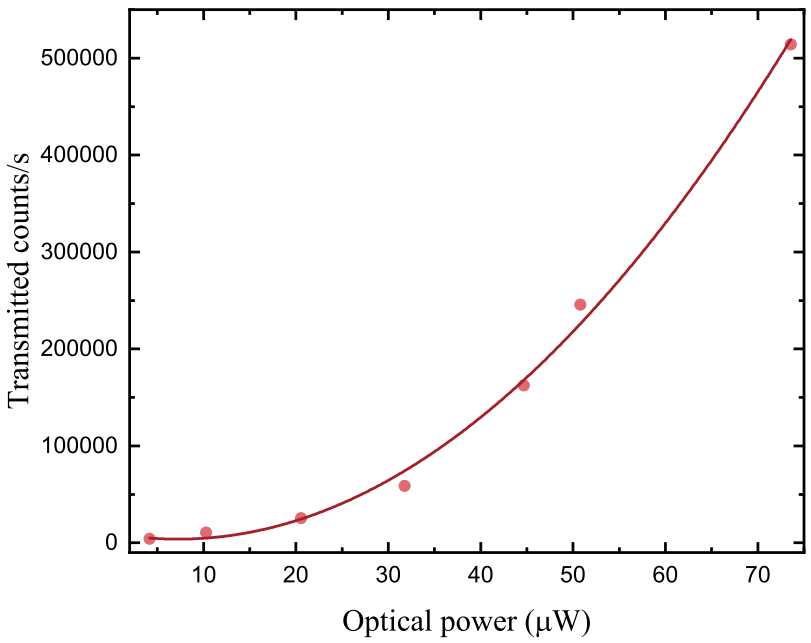

Fig. 6.4 : Steady-state transmission of the ensemble as a function of the burning power.

system to the same pulse sequence as was used previously, this time fixing the 516 nm power level to 13 mW and varying the power in the resonant beam. The associated traces, consisting of data accumulated over one minute, are shown in Fig. 6.6a. The temporal profile of the AOM rising edge measured before the cryostat is also included for reference.

When the AOM is gated on, the transmitted counts rise slower than expected from the switching mechanism alone. This indicates some time-dependent effect occurring in the ensemble which we attribute to the ionisation process. The counts plateau after $\sim 1 - 5\mu$s and the rise time is faster for higher resonant excitation powers. This provides a general idea of the time required to reach an equilibrium between the relative charge state populations. An exponential function is fitted to each of the rising edges and associated with a time constant. These are then plotted as a function of excitation power in Fig. 6.6b. The ionisation 'rate' is seen to saturate starting around 0.5 mW, for which the transmission through the ensemble becomes stable under two microseconds of exposure to the field. For all the measurements recorded in this section, the transmission of the sample remains remarkably stable in the absence of

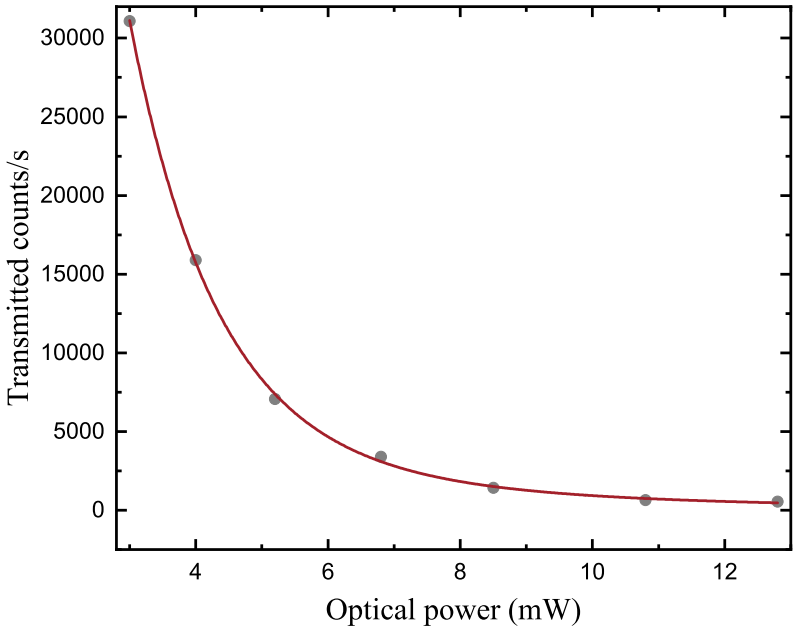

Fig. 6.5 : Transmission of the ensemble as a function of the optical power in the *reset* beam at 516 nm, accumulated over many pulse sequences. Approximately 10 mW are required in order to reinitialise the ensemble between successive ionising pulses.

illumination by optical fields, which is expected as the recombination process does not occur spontaneously.

This preliminary study allows us to scout out the parameter space in order to design an efficient spectral hole burning protocol. The ionisation process requires $\sim \mu$s burn times with ∼mW powers, which is compatible with the experimental setup available. An atomic frequency comb preparation sequence based on this data is presented and implemented in the following section.

6.3.2 Atomic frequency comb preparation

Confirming that the ionisation dynamics were favourable to use as a spectral hole burning technique, the preparation of an atomic frequency comb is attempted in the system. Traditionally, narrow transparency windows are burned into the inhomogeneously broadened transition by scanning a narrowband laser in discrete steps and thus pumping populations at specific frequencies into a shelving state. Here, a train of 3 GHz-wide pulses resonant with the transition at 637 nm is used as the burning

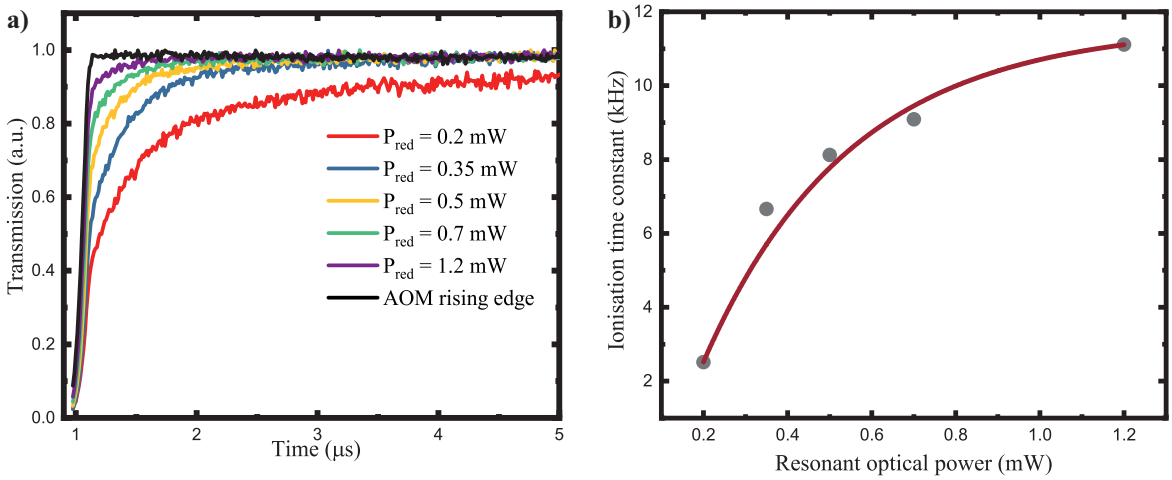

Fig. 6.6 : (a) Transmission of a resonant field as a function of time, shown for a range for optical powers. Traces are normalised so as to allow comparison of the rising edges. (b) Time constant of the rising edge plotted as a function of resonant optical power, showing diminishing returns beyond $\sim 0.5\,\mathrm{mW}$.

beam. The spectrum of a pulsed laser is a frequency comb with teeth spaced by the repetition rate and an envelope equal to the pulse bandwidth. Applying this laser directly onto the sample is thus expected to ionise NV^- centres only at the frequencies where the frequency comb has peaks, and thus imprint this comb-like structure onto the inhomogeneous spectral density profile of the ensemble.

The pulse sequence used for this experiment is shown in Fig. 6.7 and consists of the burn beam applied for $10\,\mu\mathrm{s}$, the probe for $20\,\mu\mathrm{s}$ followed by $70\,\mu\mathrm{s}$ during which the ensemble is excited with light at 516 nm in order to recycle the charge state populations. The experiment can thus be run at a 10 kHz repetition rate. Here, the probe bream is sent through the FPI setup described previously and effectively consists of a weak scannable narrowband signal capable of measuring the absorption spectrum of the ensemble with a resolution of 7.5 MHz. We collect the probe signal on a single-photon counting APD and arrange the counts in a time-of-arrival histogram with a wrap-around length defined by the FPI scanning frequency. Traces accumulated for 200 s are shown in Fig. 6.8 with and without application of the burn beam at 2 mW.

The spectrum of the bare probe beam is a smooth Gaussian profile as produced by the setup described previously. A faint amount of structure remains from the original laser spectrum due to the efficiency of the AOM depending on the modulation frequency. When the burn is applied, a clear comb-like structure appears in the absorption profile of the ensemble. To our knowledge, this constitutes the first realisation of an atomic

Fig. 6.7 : Pulse sequence used for the preparation and probing of the atomic frequency comb.

frequency comb in an ensemble of NV centres as well as the first demonstration of ionisation-based spectral hole burning in the system.

The measured comb contrast is limited to only $\sim 20\%$. This is due to a combination of drifts occurring during the long exposure time necessary for data collection and fast spectral jitter of the laser and the ensemble over the course of a single pulse sequence.

The width of the peaks in the dye laser spectrum are broadened by two distinct effects: 1) The central frequency of the comb jitters by $\sim 40\,\mathrm{MHz}$ on a kHz timescale leading to a shifting motion of the entire spectrum. 2) Changes in the carrier-envelope offset induce a breathing motion causing teeth at the extremities of the comb to shift more than teeth closer to the centre frequency. NV centres can experience dynamic shifts of their resonance frequency due to spectral diffusion. These shifts can reach tens of MHz [212] and are caused by fluctuations in the electromagnetic environment of the defect. The ionisation process involved in the AFC preparation is expected to be a significant source of such fluctuations. With an ideal laser system, the resolution of the holeburning process, and thus the achievable comb contrast is set by the homogeneous linewidth of the emitters, and generally limited by spectral diffusion.

In addition to these rapid spectral effects, the central frequency of the dye laser drifts at a rate of a few MHz per minute due to an unstable thermal environment. This shift accumulates over the integration period of the experiment leading to loss of visibility in the comb contrast. The exposure time of the experiment is set by the low signal-to-noise ratio of the probe measurement and is limited by the necessity to

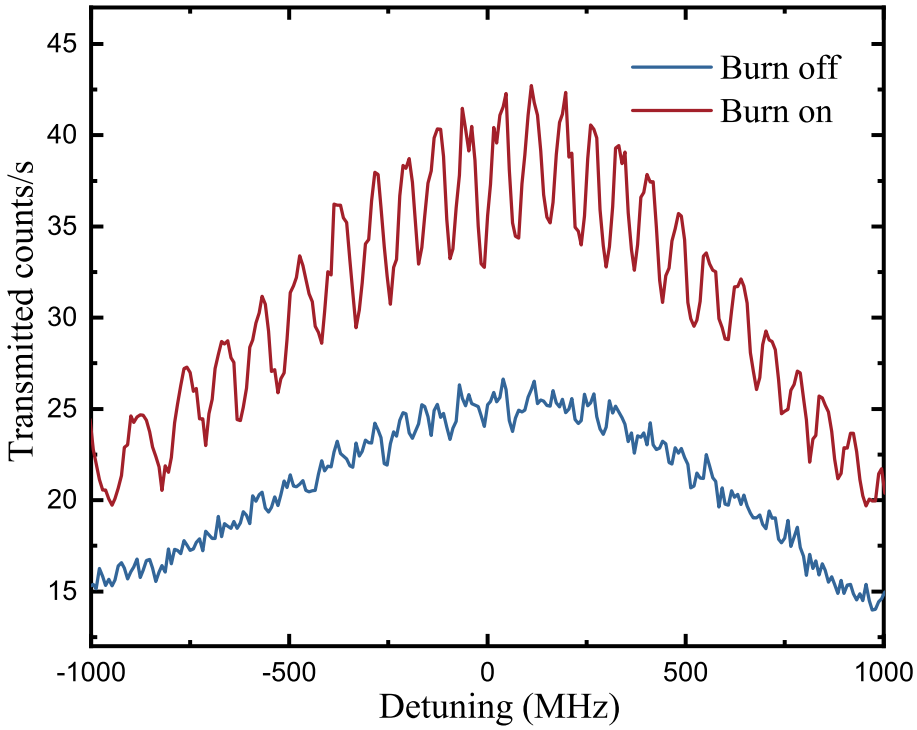

Fig. 6.8 : Spectrum of a weak resonant probe, with and without the application of the burn beam, showing the AFC structure. Burn power $P_B = 1\,\mathrm{mW}$, Reset power $P_R = 15\,\mathrm{mW}$, integration time $T_{\mathrm{int}} = 200\,\mathrm{s}$

keep the power as low as possible in order to not affect the comb profile. Furthermore, the insufficient extinction ratio of the AOMs used to switch the strong beams causes significant leakage noise easily collected by the single-photon detector. As the facets of the sample are not polished, the transmitted optical mode does not have a clean Gaussian profile leading to coupling losses into the detector fibre ($\sim 20\%$ coupling efficiency) and reducing the amplitude of the detected signal. The compression cycle causes the sample to vibrate by a magnitude larger than the focal spot. As a result, different sub-ensembles are illuminated at different points of the cycle which reduces the efficiency of the preparation process. Although this effect could be partially mitigated by using beams with wider foci, a higher optical power would be required which was not readily available at the time.

The experiment was severely limited by the issues described above which made optimising the comb preparation sequence impossible. Furthermore, although storage of single weak coherent pulses was attempted using a pulse-picking setup similar to that described in section 4.1.2, no rephasing echo could be observed. This is attributed once again to the low SNR of the experiment, in particular as a revival is expected after 12.5 ns - a timescale comparable to the NV^- excited state lifetime.

6.4 Summary and outlook

The observation of an AFC in the system is a promising result, especially since the experiment is far from being optimised. There are many potential avenues for improvement - for instance, the setup would already greatly benefit from a more stable thermal environment which would address the slow frequency drifts observed in the laser and lead to more precise measurements. The comb contrast itself is limited by the properties of the burning laser, which could be solved by actively stabilising the carrier-envelope offset of the pulse train as well as the laser cavity length.

Increasing the SNR of the experiment is critical for the optimisation of the preparation sequence as the measurements are severely hindered by the long integration times. The laser power is one of the main limiting factors here, as shorter burn and reset pulses would allow more time for probing the ensemble in a sequence. Furthermore, wider beams could then be used in order to mitigate effects linked vibrations in the cryostat.

In this chapter, a simple scheme for spectral hole burning in an ensemble of NV centres was devised and implemented. In this approach, population is pumped into the neutrally charged flavour of the defect which used as a long-lived shelving state. We investigated the required intensity and duration of the resonant pulses used to trigger the ionisation of the NV^- state. An AFC was then successfully prepared by directly pumping the ensemble with an optical frequency comb. While photon storage could not be demonstrated due to technical imperfections in the experiment, the results pave the way for the demonstration of an optical quantum memory in NV ensembles.

Chapter 7

Light-matter interaction in arrays of diamond NV centres

7.1 Introduction

The work presented in this thesis is centered around the investigation of solid-state atomic systems capable of providing a platform for efficient light-matter interactions, and in particular for the storage of quantum information. Previously, in Chap. 6, ensembles of NV centres in diamond were explored as an alternative to Pr^{3+}:Y_2SiO_5. In this chapter, we employ a parallel approach by theoretically investigating novel techniques for optically addressing solid-state quantum emitters.

The probability for a photon from a laser beam to interface resonantly with a single atom depends on the ratio of the atomic cross-section to the area of the beam, and is typically very low due to the diffraction limit. Indeed, typical interaction probabilities are limited to approximately 0.05 [233, 33] for neutral atoms or 0.01 [234] for trapped ions even with strong focusing.

Conventional avenues for enhancing atom-photon coupling strengths involve resorting to either cavities or atomic ensembles. Atomic ensembles [37] have been the main focus of the experiments presented in this thesis. In such systems, the interaction strength is related to the optical depth which scales linearly with the number of atoms. Divergence in the laser beam causes the average interaction probability per atom in an ensemble to be much lower than that which can achieved with a single emitter caught in a tight focus. It is also worth noting that the larger the ensemble, the harder it is to saturate and thus the more linear its response to light becomes.

Instead of allowing a photon to interact with many atoms, another approach is to make the photon pass through the atom many times. This can be achieved with an optical cavity, for example by trapping an atom between two mirrors and forcing light to bounce back and forth until the interaction happens [235]. The study of such systems constitutes the field of cavity quantum electrodynamics (QED). Here, the interaction probability is intuitively multiplied by the number of times the photon passes across the atom before it exits the cavity. This probability can approach unity for certain systems, reaching the so-called strong-coupling regime desired for many technological applications [31]. However, the realisation of these devices is also technically challenging [34, 236] which limits their scalability and thus their use beyond proof of principle demonstrations.

In order to produce a compact device allowing the reliable storage or manipulation of optical quantum information, a plethora of solid-state platforms have been explored employing both of these approaches. These range from relatively well understood colour centres in diamond [237, 238] and quantum dots [239] to more recently developed systems such as quantum emitters embedded in two-dimensional materials such as hexagonal boron nitride [240]. Solid-state systems naturally lend themselves to interfacing with micro- or nano-scale structures, prompting much enthusiasm for the development of reproducible designs consisting of single quantum emitters coupled to micro-cavities. While much progress has been made on this front in recent years yielding impressive results [241], many challenges remain due to insufficient coupling strengths and non-deterministic fabrication methods.

Nevertheless, the confinement of light to extremely small mode areas provided by nanophotonic structures offers a powerful way forwards. In this chapter, we consider a promising approach relying on atomic emitters coupled to photonic waveguides, often referred to as waveguide QED [242]. This broad formalism encompasses platforms ranging from neutral atoms trapped in the evanescent field of a nanofibre [35] to solid-state crystal defects interacting with a nanophotonic waveguide [185]. The efficiency of the interaction between a single emitter and the waveguide field is typically quantified using the ratio Γ_{1D}/Γ' of the atom's decay rate into the waveguide Γ_{1D} to that into other electromagnetic modes Γ' as shown in Fig. 7.1. This figure of merit depends strongly on the matching of the guided mode to the atomic dipole pattern and varies widely according to the particular implementation of the system, from $\Gamma_{1D}/\Gamma' \sim 0.03$ [243] in tapered optical fibres to $\Gamma_{1D}/\Gamma' \sim 1$ when using photonic crystal waveguides [244]. Unlike cavity QED, the atoms can couple to a continuum of guided electromagnetic

modes in this case. In practice this means that the requirements for this system are potentially less stringent as it is no longer necessary to match the narrow bandwidth of a cavity to an atomic emitter's resonance.

Atomic ensembles can also be interfaced with by using photonic nanostructures. Unlike conventional setups using focused Gaussian beams, light confinement can be maintained over the length of the ensemble, leading to a substantially enhanced optical depth. This was demonstrated experimentally by coupling an optical nanofibre to an ensemble of cold Rubidium atoms to obtain a sixtyfold increase in optical depth with respect to the case of a free space atomic cloud [35]. This is a promising result despite the interaction strength being limited to $\Gamma_{1D}/\Gamma' \sim 0.04$ and the experimental setup remaining fairly complex. The development of a monolithic version of such a system in the solid state is an exciting prospect and would eliminate the need to trap atoms in free space.

When an atomic ensemble is coupled to a waveguide, the optical depth typically scales linearly with the number of atoms, as is the case in free space. The scaling assumes that the atoms in the ensemble are independent, and thus that each additional atom represents one more chance for an absorption or emission event to occur. This is reasonable in a disordered ensemble, as there is no fixed phase relationship between the waves emitted by each atom and interference phenomena are suppressed. However, in the case of arrays of atoms with well-defined spatial distributions, as shown in Fig. 7.1 the assumption of independent emission breaks down. This implies that the performance of protocols based on light-matter interactions may scale differently in array-based systems with respect to conventional ensembles. Recent theoretical work supports this claim [245, 246], suggesting that improvements in quantum memory efficiencies could be expected.

In this chapter, we theoretically investigate the relevance of this novel type of system within the greater landscape of solid-state devices for quantum light-matter interaction. Inspired by promising technological advances [247], we will focus on arrays of diamond NV centres coupled to a nanophotonic waveguide. In the first section a physical model is introduced describing the response of atomic arrays interacting with a guided electromagnetic mode. We also discuss a few solutions pertaining to simple cases of the model. Following this, we apply this formalism to NV centres, considering an interesting use case concerning the design of robust optical cavities using atomic arrays. Throughout this study, we focus on the experimental imperfections associated with such systems and aim to provide as realistic an analysis as possible bearing in mind

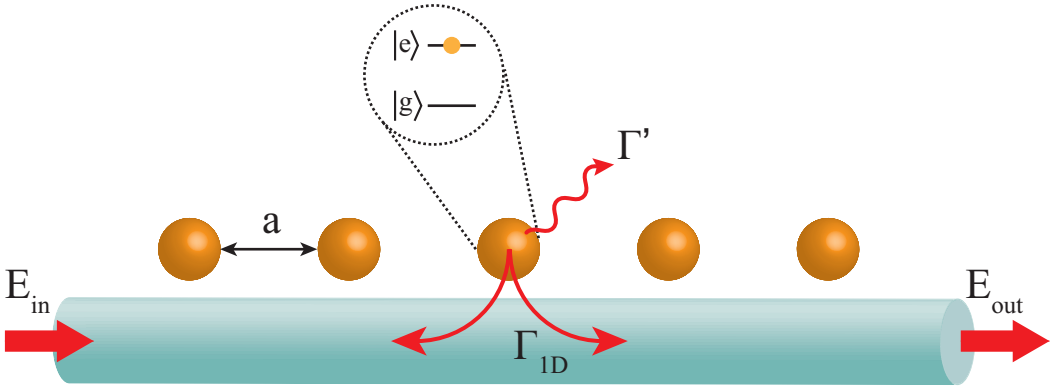

Fig. 7.1 : Schematic of an array of atoms interacting with a one-dimensional waveguide. Emission into the guided mode is characterised by a rate Γ_{1D} and emission into free space by Γ'. E_{in} and E_{out} refer to input and output fields.

current technological capabilities. The theoretical formalisms presented in sections 7.2 and 7.3 are reviewed from existing literature, in particular Refs. [248–251]. In section 7.4, we present the results of simulations adapting these models to the case of NV centres, performed by myself under the supervision of J.N. Becker and J. Nunn, with input from P. M. Ledingham.

7.2 Waveguide QED with arrays of two-level atoms

In this section, we introduce a framework describing the physics of atom-photon interactions in the vicinity of an optical waveguide. Light interacting with an atomic ensemble is often modelled using the well-known Maxwell-Bloch equations [252]. In such a formalism, the exact positions of each atom are not taken into account and the ensemble is treated as a medium with a smooth density distribution. In this way, and by further assuming that the atoms do not interact with each other, large systems containing trillions of emitters can be simulated efficiently. Unfortunately, due to these assumptions, the Maxwell-Bloch formalism is also incapable of accurately modelling interference phenomena in atomic arrays. In this section we present a well-developed alternative approach which does take into account the degrees of freedom of each individual atom and its interaction with a guided electromagnetic mode. Most of the material in this section is derived from existing literature [248–250], and our aim is to outline the fundamental underpinnings of the model as well as to shed some light on the results and how to apply them.

7.2.1 Outline of the model - input-output relations

We consider an ensemble of identical two-level atoms with ground states $|g\rangle$ and excited states $|e\rangle$ separated by an optical transition with frequency ω_0. This ensemble is coupled to a one-dimensional dielectric waveguide. The full Hamiltonian of the system is composed of three terms: H_{at} describing the energy levels of the atoms, H_{ph} associated with the photons freely propagating along the waveguide and H_{int} accounts for the interaction between the atoms and the photons. It can be written explicitly as

$$\begin{aligned} \text{H} &= H_{at} + H_{ph} + H_{int} \\ &= \sum_j \hbar\omega_0 \sigma_{ee}^j + \int dk \hbar\omega_k a_k^\dagger a_k + \sum_j \int dk \hbar g_k (\sigma_{eg} a_k e^{ikx_j} + \text{h.c.}), \end{aligned} \tag{7.1}$$

where $\sigma_{eg}^j = |e_j\rangle \langle g_j|$ is the atomic operator for atom j at position x_j and a_k the annihilation operator for the propagating mode with wavevector k and frequency ω_k. The atom-field coupling amplitude is given by $g_k = \sqrt{\frac{d_{eg}^2 \omega_k}{4\pi\epsilon_0 \hbar A}}$ with d_{eg} the magnitude of the dipole matrix element associated with the atomic transition and A_m is the effective mode area.

The state of each atom is encoded with the density operator ρ_S which evolves according to the master equation

$$\dot{\rho_S} = \frac{1}{i\hbar}[H, \rho_S] + L[\rho_S], \tag{7.2}$$

where the Lindblad terms are

$$L[\rho_S] = -\frac{\Gamma'}{2} \sum_j (\sigma_{eg}^j \sigma_{ge}^j \rho_S + \rho_S \sigma_{eg}^j \sigma_{ge}^j - 2\sigma_{ge}^j \rho_S \sigma_{eg}^j), \tag{7.3}$$

Γ' being the decay rate of the atoms into free space. The dispersion of the waveguide is assumed to be linear in the vicinity of ω_0, which consitutes the region of interest. The guided mode frequency can then be approximated as $\omega_k \approx v_g|k|$, where v_g is the group velocity of light in the medium.

By separating the guided portion of the field into right- and left-propagating modes (designated by R and L respectively) and defining the Fourier transform of the field operators as

$$a_{k_{R(L)}} = \frac{1}{\sqrt{2_\pi}} \int dx e^{-ikx} a_{R(L)}(x), \tag{7.4}$$

the Hamiltonian can be translated to the real space to yield [248]

$$\begin{aligned} H/\hbar &= \sum_j \omega_0 \sigma_{ee}^j + \int dx \left(-iv_g a_R^\dagger \frac{\partial}{\partial x} a_R(x) + iv_g a_L^\dagger(x) \frac{\partial}{\partial x} a_L(x) \right) \\ &+ \sqrt{2\pi} g \int dx \sum_j \delta(x - x_j) \left(a_R^\dagger(x) \sigma_{ge}^j + \sigma_{eg}^j a_R + a_L^\dagger(x) \sigma_{ge}^j + \sigma_{eg}^j a_L \right). \end{aligned} \tag{7.5}$$

The real-space field operators then represent the creation or annihilation of a photon propagating to the right or left.

The Heisenberg equations of motion can then be obtained from the relevant commutators and read

$$\dot{\sigma}_{ge}^j = -i\omega_a \sigma_{ge}^j + i\sqrt{2\pi} g (\sigma_{gg}^j - \sigma_{ee}^j)(a_R(x_j) + a_L(x_j)) \tag{7.6}$$

for the atomic coherences and

$$\left(\frac{1}{v_g} \frac{\partial}{\partial t} + \frac{\partial}{\partial x} \right) a_R(x,t) = \frac{i\sqrt{2\pi} g}{v_g} \sum_j \delta(x - x_j) \sigma_{ge}^j \tag{7.7a}$$

$$\left(\frac{1}{v_g} \frac{\partial}{\partial t} - \frac{\partial}{\partial x} \right) a_L(x,t) = \frac{i\sqrt{2\pi} g}{v_g} \sum_j \delta(x - x_j) \sigma_{ge}^j \tag{7.7b}$$

for the waveguide modes. Integrating Eqs. 7.7a) and 7.7b leads to the general solution for the field operators given by

$$a_R(x,t) = a_{R,in}(x - v_g t) - \frac{i\sqrt{2\pi} g}{v_g} \sum_j \theta(x - x_j) \sigma_{ge}^j \left(t - \frac{x - x_j}{v_g} \right) \tag{7.8a}$$

$$a_L(x,t) = a_{L,in}(x + v_g t) - \frac{i\sqrt{2\pi} g}{v_g} \sum_j \theta(x_j - x) \sigma_{ge}^j \left(t + \frac{x - x_j}{v_g} \right), \tag{7.8b}$$

where $\theta(x)$ is the Heaviside step function. Here, the term $a_{R,in}$ refers to the portion of the field which propagates through the waveguide without interacting with any of the atoms. The second term represents the component of the field scattered by each atom.

Then, we define a variable rotating at a frequency ω_L, $\tilde{\sigma}_{ge}^j = \sigma_{ge}^j e^{i\omega_L t}$, which is assumed to have a slow-varying envelope so that $\tilde{\sigma}_{ge}^j(t - x/v_g) \approx \tilde{\sigma}_{ge}^j(t) e^{i\omega_0 t x/v_g}$. The solutions 7.8a and 7.8b can be substituted into Eq. 7.4 in order to obtain an equation

of motion for the atomic coherences in the rotating frame,

$$\dot{\tilde{\sigma}}^j_{ge} = i\Delta\tilde{\sigma}^j_{ge} + i\sqrt{2\pi}g(\tilde{\sigma}^j_{ee} - \tilde{\sigma}^j_{gg})a_{\rm tot}(x_j) + \frac{\Gamma_{\rm 1D}}{2}(\tilde{\sigma}^j_{ee} - \tilde{\sigma}^j_{gg})\sum_l \tilde{\sigma}^l_{ge}e^{ik|x_j - x_l|}, \tag{7.9}$$

where $\Gamma_{\rm 1D} = \frac{4\pi g^2}{v_g}$ is the emission rate of a single atom into the guided mode, $\Delta = \omega_L - \omega_0$ and $a_{\rm tot}(x,t) = a_{\rm R,in}(x - v_g t) + a_{\rm L,in}(x + v_g t)$.

Additionally, the slow-varying rotating variables can be substituted into Eqs. 7.8 leading to an input-output relation [253] for the fields,

$$a_R(x) = a_{R,in}(x) - i\sqrt{\frac{\Gamma_{\rm 1D}}{2v_g}}\sum_j \tilde{\sigma}^j_{ge}(t)e^{ik(x-x_j)} \tag{7.10a}$$

$$a_L(x) = a_{L,in}(x) - i\sqrt{\frac{\Gamma_{\rm 1D}}{2v_g}}\sum_j \tilde{\sigma}^j_{ge}(t)e^{-ik(x-x_j)}, \tag{7.10b}$$

which can then be used in order to compute the optical transmission of the full system.

7.2.2 Effective Hamiltonian

The evolution of the atomic coherences in Eq. 7.9 is described only in terms of the atomic degrees of freedom. These dynamics can be obtained equivalently through another master equation for a reduced density matrix ρ which does not explicitly include the field:

$$\dot{\rho} = \frac{1}{i\hbar}[H_{tot}, \rho] + L_{wg}[\rho] + L_{ng}[\rho]. \tag{7.11}$$

If the atoms are driven by an external field with frequency ω_L and amplitude $\mathcal{E}$, the Hamiltonian for this model is given by

$$\mathrm{H}_{\rm tot}/\hbar = \sum_j \left[-\Delta\tilde{\sigma}^j_{ee} - \Omega(\tilde{\sigma}^j_{eg}e^{ikx_j} + \mathrm{h.c.})\right] + \frac{\Gamma_{\rm 1D}}{2}\sum_{j,l}\sin(k|x_j - x_l|)\tilde{\sigma}^j_{eg}\tilde{\sigma}^l_{ge}. \tag{7.12}$$

The terms in the first sum represent the bare Hamiltonians for each atom and their individual interaction with the external field characterised by a Rabi frequency $\Omega = \sqrt{2\pi}g\mathcal{E}$. The second summation accounts for the dipole-dipole interaction resulting from coherent photon exchanges between different atoms (labeled j and l). Dissipation in the system is modelled via a Lindbladian composed of two parts, the first being

given by

$$\mathrm{L}_{wg}[\rho] = -\frac{\Gamma_{1\mathrm{D}}}{2}\sum_{\mathrm{j,l}}\cos(k|x_j - x_l|)(\tilde{\sigma}^j_{eg}\tilde{\sigma}^l_{ge}\rho + \rho\tilde{\sigma}^j_{eg}\tilde{\sigma}^l_{ge} - 2\tilde{\sigma}^l_{ge}\rho\tilde{\sigma}^j_{eg}) \tag{7.13}$$

and describes atomic decay into the guided mode. The terms where $j = l$ reduce to the independent decay of each atom into the waveguide. All the other terms account for collective dissipative effects, where the decay of one atom affects that of another, and can lead to phenomena such as superradiance or subradiance [254].

The second portion of the Lindbladian is similar as that described in Eq. 7.3,

$$L_{ng}[\rho] = -\frac{\Gamma'}{2}\sum_j(\tilde{\sigma}^j_{eg}\tilde{\sigma}^j_{ge}\rho + \rho\tilde{\sigma}^j_{eg}\tilde{\sigma}^j_{ge} - 2\tilde{\sigma}^j_{ge}\rho\tilde{\sigma}^j_{eg}), \tag{7.14}$$

and describes loss of an atomic excitation to any other channel, such as non-guided modes of the field or non-radiative decay. Throughout this chapter we assume that no cooperative effects can be mediated by these channels, i.e. that an atom cannot be excited by a photon emitted into a non-guided mode.

The atomic model described here produces the same equations of motion for the coherences as shown in Eq. 7.9, with the addition of dissipation into non-guided modes which was included phenomenologically. However, if we limit ourselves to a regime where the atoms are weakly saturated ($\langle\sigma_{ee}\rangle \sim 0$), this formalism can be faithfully rewritten in terms of an effective non-Hermitian Hamiltonian [249]. Then, the dynamics of the system can be obtained by solving the Schrödinger equation for the time-evolving atomic wavefunction $|\psi(t)\rangle = c_g(t)\,|g\rangle^{\otimes N} + \sum_j c^j_e(t)\,|e_j\rangle$, with $|e_j\rangle = \tilde{\sigma}^j_{eg}\,|g\rangle^{\otimes N}$. This offers a practical advantage as solving the master equation for the full density matrix of more than a few tens of atoms is a demanding task. This effective Hamiltonian is given by

$$\begin{aligned}\mathrm{H}_{\mathrm{eff}}/\hbar &= \mathrm{H}_{\mathrm{indep}} + \mathrm{H}_{\mathrm{coop}} \\ &= -\sum_j\left[(\Delta + i\frac{\Gamma'}{2})\tilde{\sigma}^j_{ee} + \Omega(\tilde{\sigma}^j_{eg}e^{ikx_j} + \mathrm{h.c.})\right] - i\frac{\Gamma_{1\mathrm{D}}}{2}\sum_{j,l}e^{ik|x_j - x_l|}\tilde{\sigma}^j_{eg}\tilde{\sigma}^l_{ge}.\end{aligned} \tag{7.15}$$

and accounts for all phenomena in the system (with the exception of quantum jumps) while only requiring computation of the wavefunction.

The Hermitian part of the Hamiltonian leads to coherent phenomena, while losses in the system are due to its non-Hermitian components. The atoms interact via an

effective light-mediated dipole-dipole coupling carried by the waveguide field. Both coherent and dissipative collective effects are encoded within the second term, $\mathrm{H}_{\mathrm{coop}}$. The magnitude of these effects are inherently tied together by the coupling to the waveguide $\Gamma_{1\mathrm{D}}$. As a result, any change in the energy-level splitting due to coherent collective coupling to the waveguide goes hand in hand with an associated broadening of the linewidth.

As losses in the waveguide are neglected, the dipole-dipole coupling only evolves sinusoidally with the distance between two atoms ($\sim e^{ik|x_j-x_l|}\tilde{\sigma}^j_{eg}\tilde{\sigma}^l_{ge}$) leading to an interaction with effectively infinite range also observed in experiments, such as that in Ref. [254]. This assumption is justified as, provided that the total length of the system is short enough, absorption and scattering in most realistic waveguides can indeed be ignored [35, 255]. In general, the behaviour of the ensemble is highly dependent on the atomic spacing (the 'lattice constant' of the array), which will be expanded upon in the following section.

Finally, the output field properties can be calculated using the input-output relations given in Eq. 7.10 [253]. The system is driven by a weak right-travelling probe field introduced from a position $x < x_1$. The transmitted field a_{trans} is then defined as the right-travelling field at a position beyond the last atom, and the reflected field a_{ref} as any left-travelling field at a position before the first atom; these are given by

$$a_{trans}(x) = \mathcal{E}e^{ikx} - i\sqrt{\frac{\Gamma_{1\mathrm{D}}}{2v_g}}\sum_j \tilde{\sigma}^j_{ge}(t)e^{ik(x-x_j)} \tag{7.16a}$$

$$a_{ref}(x) = i\sqrt{\frac{\Gamma_{1\mathrm{D}}}{2v_g}}\sum_j \tilde{\sigma}^j_{ge}(t)e^{-ik(x-x_j)}. \tag{7.16b}$$

The transmission coefficient T can be obtained by first computing the steady-state wavefunction of the driven system $|\psi_{ss}\rangle$ and then evaluating

$$T = |t|^2 = \frac{\langle\psi_{ss}|\, a^\dagger_{trans}(x)a_{trans}(x)\,|\psi_{ss}\rangle}{\mathcal{E}^2} \tag{7.17}$$

for $x > x_N$. A similar expression can also be found for the reflection coefficient R.

From Eq. 7.9, the equation of motion for the expectation values of the coherences $s^j_{ge} = \langle\tilde{\sigma}^j_{ge}\rangle$ is given by

$$\dot{s}^j_{ge} = \left(i\Delta - \frac{\Gamma_{1\mathrm{D}}}{2}\right)s^j_{ge} - i\Omega e^{ikx_j} - \frac{\Gamma_{1\mathrm{D}}}{2}\sum_l s^l_{ge}e^{ik|x_j-x_l|} \tag{7.18}$$

as $\langle\tilde{\sigma}_m^j\tilde{\sigma}_n^l\rangle \approx \langle\tilde{\sigma}_m^j\rangle\langle\tilde{\sigma}_n^l\rangle$ and $\langle\tilde{\sigma}_{gg}^j\rangle \approx 1$ in the weakly saturated limit. This equation can then be solved in the steady state in order to calculate the reflection and transmission coefficients.

7.2.3 Application to simple examples

In this section, we shed some light on the behaviour of the system through a few simple examples where only one or two atoms are coupled to the waveguide. This treatment will then be expanded to consider the case of an array of N atoms.

Waveguide coupled to a single atom or defect

The case where a single atomic emitter is coupled to the waveguide is interesting in order to build an intuition for the system. As before, the atom is driven by an external probe field and decays into the guided and unguided modes of the field at rates given by Γ_{1D} and Γ' respectively.

Following Eqs. 7.16 and 7.18, the transmission of a system with a single atom on resonance is

$$\begin{aligned} T &= \frac{1}{\mathcal{E}^2}\left(\mathcal{E} - i\sqrt{\frac{\Gamma_{1D}}{2v_g}}s_{ge}\right)^2 \\ &= \left(\frac{\Gamma'}{\Gamma' + \Gamma_{1D}}\right)^2, \end{aligned} \tag{7.19}$$

which agrees with the general intuition that the transmission through the system should decrease with increasing coupling to the waveguide. This expression can be applied to an experimental example, where a single germanium-vacancy defect in diamond is coupled to a nanophotonic waveguide [185]. The emission into the waveguide is measured to be $\Gamma_{1D}/\Gamma' \geq 0.1$ by collecting fluorescence while the tranmission through the waveguide in the presence of the defect is recorded at $T = 0.82 \pm 1\%$ corrected for waveguide losses. This is in strong agreement with the corresponding value of $T = 0.826$ obtained via Eq. 7.19.

Analogously, the reflection coefficient is given by

$$R = \left(\frac{\Gamma_{1D}}{\Gamma_{1D} + \Gamma'}\right)^2, \tag{7.20}$$

suggesting that high reflection probabilities could be obtained for $\Gamma_{1D} > \Gamma'$.

Waveguide coupled to two atoms

When more than a single atom is considered, dipole-dipole interaction between the emitters becomes relevant. From Eq. 7.15, it is apparent that the interaction depends on the phase $\varphi = k|x_j - x_l|$ accumulated by the light emitted by an atom when it is re-absorbed by another. The spacing between the emitters is a critical parameter which defines the properties of the system as a whole. We will distinguish two cases, on one hand where the lattice constant d is an even multiple of $\lambda/4$ and $\varphi = \pi$ and on the other where d is an odd multiple of $\lambda/4$ and $\varphi = \pi/2$.

If $k|x_j - x_l| = \pi$, only the dissipative part of the coupling between the atoms remains. The effective Hamiltonian can be diagonalised to reveal the presence of a single eigenmode with an increased decay rate $\Gamma = \Gamma' + 2\Gamma_{1D}$. This aligns well with the intuition that when the light emitted by both atoms is in phase, constructive interference occurs and superradiant decay should be observed. This enhanced decay is accompanied by an equivalent increase of the linewidth of the system.

When $k|x_j - x_l| = \pi/2$, it is the dissipative component of the atom-atom interaction that vanishes. The Hamiltonian then supports two eigenmodes in the form of symmetric and antisymmetric wavefunctions. The coherent dipole-dipole interaction splits the dressed states by $\pm\Gamma_{1D}$, although these cannot be distinguished experimentally as the splitting is narrower than their linewidth given by $\Gamma = \Gamma' + \Gamma_{1D}$. The linewidth profile is the sum of two Lorentzians shifted with respect to one another, leading to a lower reflection coefficient on resonance compared to the $\varphi = \pi$ case. This can be understood as the reflected fields from both atoms are out of phase and interfere destructively.

The reflection coefficients for each case are plotted in Fig. 7.2 for each case along with the single atom-case shown for reference. In Fig. 7.2a, the superradiance-induced linewidth enhancement is apparent while one can see that the reflection on resonance is reduced in 7.2b due to destructive interference between emission from both atoms.

7.2.4 Waveguide coupled to an array of many atoms

In general, the effective Hamiltonian can be diagonalised in the one-excitation manifold as $\mathrm{H}_{\mathrm{eff}} |\psi_\xi\rangle = \sum_\xi \lambda_\xi |\psi_\xi\rangle$, where $|\psi_\xi\rangle = c_\xi^j |e_j\rangle$. However, as $\mathrm{H}_{\mathrm{eff}}$ is non-Hermitian the vectors $|\psi_\xi\rangle$ are collective modes of the atomic array, but not standard quantum mechanical states. This means that they do not follow the typical orthogonality

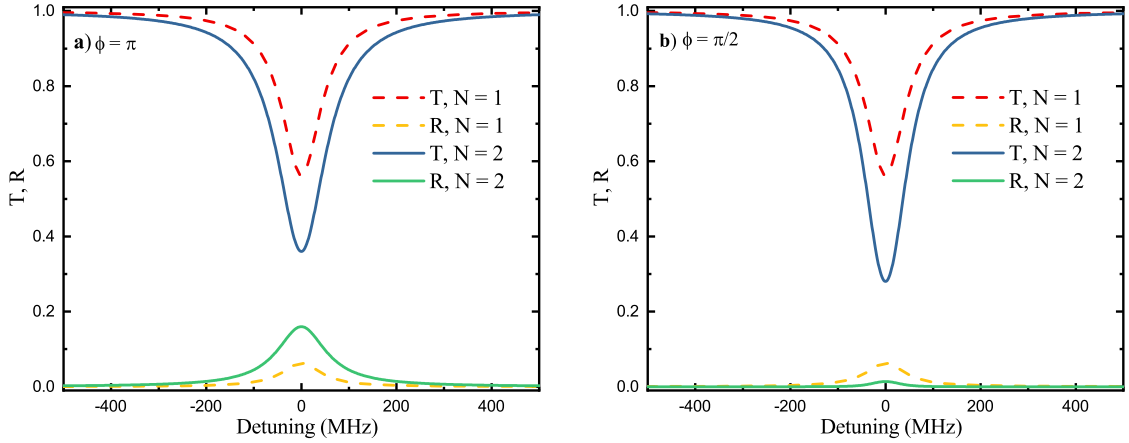

Fig. 7.2 Transmission and reflection spectra of arrays of two atoms for $\varphi = \pi$ (a) and $\varphi = \pi/2$ coupled to an optical waveguide with $\Gamma_{1D} = 0.25\Gamma_0 = \Gamma'/3$. Single atom spectra are included in dotted lines for reference.

relations such as $\langle\psi_\xi|\psi_{\xi'}\rangle = \delta_{\xi,\xi'}$. Nevertheless, they provide an intuition for the spatial profile of the excitation along the array and are useful in order to calculate the optical properties of the system. The eigenvalues λ_ξ are complex-valued, where the real part is the frequency shift associated with the mode ξ and $2\mathrm{Im}(\lambda_\xi) = \Gamma_{\xi,1D}$, its the decay rate into the waveguide mode.

In a system which contains a number of atoms N greater than two, the eigenstates supported by the Hamiltonian result from a mixture of both coherent and dissipative couplings. As a result, it is difficult to find a general analytical expression for them except when $\varphi = \pi$ where the coherent coupling vanishes for all N. In this particular case, only a single superradiant eigenstate is supported in the array. The spectral properties of the ensemble then follow a Lorentzian profile with a linewidth $\Gamma = \Gamma' + N\Gamma_{1D}$, while the transmission and reflection coefficients on resonance are

$$T = \frac{\Gamma'^2}{(\Gamma' + N\Gamma_{1D})^2}, \qquad R = \frac{(N\Gamma_{1D})^2}{(\Gamma' + N\Gamma_{1D})^2}. \tag{7.21}$$

In this configuration, the coupling of the ensemble to the waveguide increases by a factor of N. An implication of this result is that even if each atom interacts fairly weakly with the waveguide, an atomic array can be made to strongly reflect incoming photons by increasing the number of emitters. This was demonstrated by Corzo *et al.* [256] in an impressive experiment where a reflectance of up to 75% was observed in chain of $N = 2000$ atoms coupled to an optical nanofibre with coupling values of only

$\Gamma_{1D} \leq 0.01$ [256]. Beyond supporting existing models of waveguide QED, this result suggests that systems based on collective effects in atomic arrays can be developed with existing technologies.

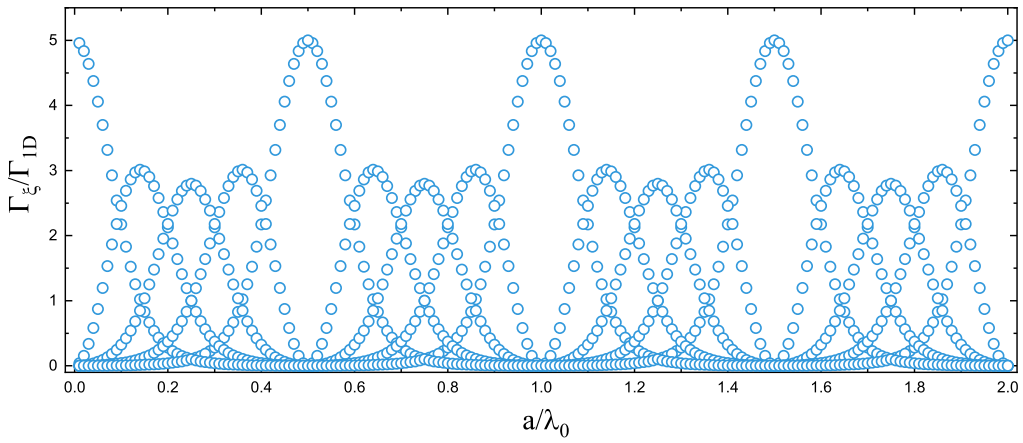

Fig. 7.3 : Normalised decay rates of the collective modes in an array of 5 emitters coupled to an optical waveguide, shown as a function of the array lattice constant a in units of the emitters' resonant wavelength.

The system becomes more complex when the lattice constant of the array is not an integer multiple of $\lambda/2$, and in general the equations of motion have to be solved numerically. The normalised decay rates $\Gamma_{\xi,1D}/\Gamma_0$ are plotted for a chain of five atoms as a function of the atomic separation in Fig. 7.3, showing the periodicity of the system. In general, the array supports a collection of superradiant and subradiant modes except when $d = m\lambda/2$ for integer m, where only a single bright mode exists.

The resonant transmittance and reflectance are shown in Fig. 7.4 versus atomic separation, this time for $N = 40$ and $\Gamma_{1D} = 0.1\Gamma'$. The transmission for the case where the atoms do not interact with each other, given by

$$T_{\text{indep}} = \left| \frac{\Delta + i\Gamma'/2}{\Delta + i(\Gamma' + \Gamma_{1D})/2} \right|^{2N} \tag{7.22}$$

is also included for comparison.

The reflection coefficient is seen to peak at $\varphi = \pi$ as expected. It is also negligible for non-interacting atoms and hence was not plotted. The transmission is minimised at $\varphi = \pi/2$ but remains relatively stable for all spacings as long as a is not in the vicinity of a multiple of $\lambda/2$.

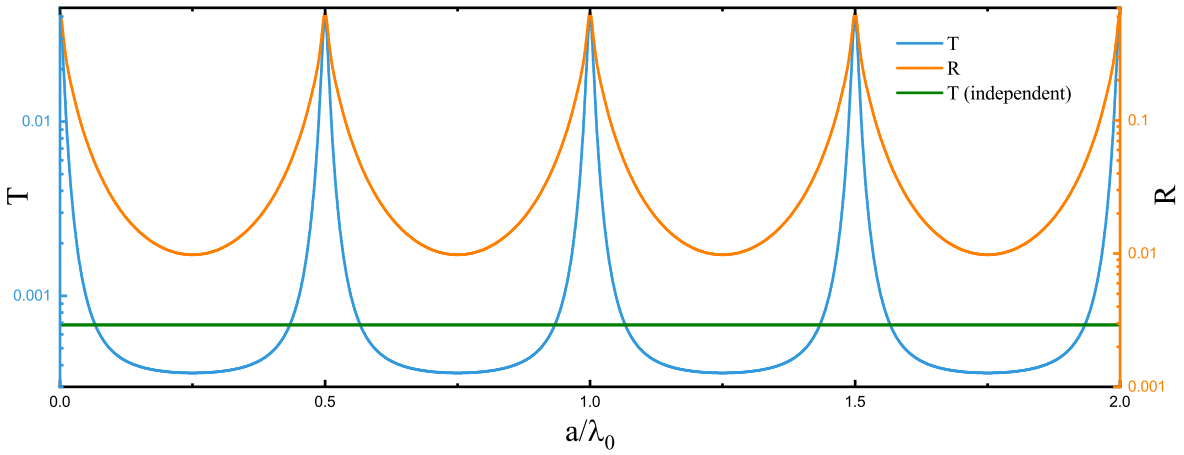

Fig. 7.4 : Transmission and reflection coefficients of an array of 40 atoms as a function of the spacing a between individual emitters in units of their resonance wavelength. The transmission of a disordered array is also included in green for reference.

If the coupling of each atom to the waveguide is very weak (i.e. when $\Gamma_{1D} \ll \Gamma'$), the interaction between the atoms in the array can be neglected. In this limit, the emitters are effectively independent and the transmittance can be approximated to the profile given in Eq. 7.22. This equation can be expanded in a power series which can be shown to reduce in the first order to the Beer-Lambert law with an optical depth $OD = 2N\Gamma_{1D}/\Gamma'$. This regime is however quite limited and breaks down for realistic values of Γ_{1D}/Γ' as shown in Fig. 7.5 for $N = 40$.

7.3 Alternative formalism based on Green's functions

The model outlined in section 7.2 is limited to scalar interactions between an array of atoms and a one-dimensional waveguide. In order to capture the physics of more realistic systems, it may also become necessary to take into account effects not included in a 1D formalism, such as atomic dipole orientations and the dielectric surroundings of the emitters. In this section, we will briefly describe a more general framework pioneered by Welsch *et al.* [251] which uses the electromagnetic Green's function in order to provide a more detailed description of the field surrounding the atoms. In what follows, only the necessary aspects of the formalism will be presented, but the full

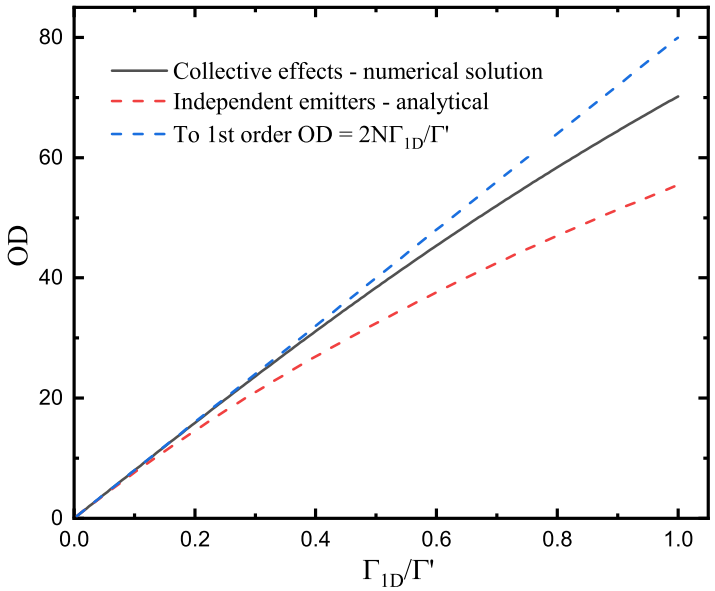

Fig. 7.5 : Optical depth of an array of 40 atoms, calculated numerically and analytically according to two different approximations, as a function of emitter-waveguide coupling.

derivation can be found along with further details in the doctoral thesis of Jonathan Hood [257] and works by Asenjo-Garcia *et al.* [258].

The general idea behind the model is similar to what was described previously, an array of regularly spaced atoms at well defined positions $\mathbf{r}_i$ interact by exchanging photons via the electromagnetic field. Integrating out the field as was done in section 7.2 leads to a master equation characterised by the following Hamiltonian,

$$\mathrm{H} = -\hbar\Delta \sum_i \sigma^i_{ee} - \sum_i \left[\mathbf{d}_i \cdot \mathbf{E}_p^- \sigma^i_{ge} + \mathbf{d}_i^* \cdot \mathbf{E}_p^+ \sigma^i_{eg}\right] - \hbar \sum_{ij} J^{ij} \sigma^i_{eg} \sigma^j_{ge} \tag{7.23}$$

and Lindblad operators,

$$\mathrm{L}[\rho_A] = \sum_{ij} \frac{\Gamma^{ij}}{2} (2\sigma^i_{ge}\rho_A\sigma^j_{eg} - \sigma^i_{eg}\sigma^j_{ge}\rho_A - \rho_A\sigma^i_{eg}\sigma^j_{ge}) \tag{7.24}$$

where $\mathbf{E}_p = \mathbf{E}_p^+ + \mathbf{E}_p^-$ represents the left and right-travelling components of a probe field with frequency ω_L and the dipole matrix element of the transition $\mathbf{d}_i$ for atom i is now a vector quantity. The properties of the interaction between the atoms are given by the coefficients Γ_{ij} and J^{ij} given by

$$J^{ij} = \frac{\mu_0 \omega_L^2}{\hbar} \mathbf{d}_i^* \cdot \mathrm{Re}\ \mathbf{G}(\mathbf{r}_i, \mathbf{r}_j, \omega_L) \cdot \mathbf{d}_j \tag{7.25a}$$

$$\Gamma^{ij} = \frac{2\mu_0 \omega_L^2}{\hbar} \mathbf{d}_i^* \cdot \mathrm{Im}\ \mathbf{G}(\mathbf{r}_i, \mathbf{r}_j, \omega_L) \cdot \mathbf{d}_j. \tag{7.25b}$$

Here, $\mathbf{G}(\mathbf{r}, \mathbf{r}', \omega)$ refers to the electromagnetic Green's function and describes the field at a point $\mathbf{r}$ due to a dipole placed at $\mathbf{r}'$ oscillating at a frequency ω. It is a dyadic tensor and the general solution of the classical electromagnetic wave equation [259],

$$\nabla \times \nabla \times \mathbf{G}(\mathbf{r}, \mathbf{r}', \omega) - \frac{\omega^2}{c^2} \epsilon(\mathbf{r}, \omega) \mathbf{G}(\mathbf{r}, \mathbf{r}', \omega) = \delta(\mathbf{r} - \mathbf{r}') \mathbb{1}, \tag{7.26}$$

where $\epsilon(\mathbf{r}, \omega)$ is the relative permittivity of the medium. In practice, $\mathbf{G}$ can be encoded in a 3×3 matrix $G_{\alpha\beta}$ at each position $\mathbf{r}$, the elements of which design the field component project along a direction α emitted by a source placed at $\mathbf{r}'$ and oriented in a direction β with $\{\alpha, \beta\} = \{x, y, z\}$. As such, if all the atoms are oriented towards $\hat{\mathbf{x}}$, only the G_{xx} part of the Green's function is relevant. The use of the classical Green's function is justified in this system as the quantum fields produced by two-levels atoms generally propagate in the same way as classical fields in dielectric media.

In the weak-saturation limit of the atoms composing the array, the master equation defined in Eqs. 7.23 and 7.24 can be equivalently recast into a non-Hermitian Hamiltonian as was done in Eq. 7.15. This effective Hamiltonian is given by

$$\mathrm{H_{eff}} = -\hbar\Delta \sum_i \sigma_{ee}^i - \hbar \sum_i (\Omega e^{ikx_i} \sigma_{eg}^i + \mathrm{h.c.}) - \mu_0 \omega_0^2 \sum_{ij} \mathbf{d}^* \cdot \mathbf{G}(\mathbf{r}_i, \mathbf{r}_j, \omega_L) \cdot \mathbf{d} \tag{7.27}$$

The atomic states are then captured entirely within the atomic wavefunction and calculating the evolution of the full density matrix ρ_A is not required.

The field at each point in space can be reconstructed given the atomic states via the following input-ouput relation

$$\mathbf{E}_{out}(\mathbf{r}) = \mathbf{E}_p(\mathbf{r}) + \mu_0 \omega_L^2 \sum_j \mathbf{G}(\mathbf{r}, \mathbf{r}_i, \omega_L) \cdot \mathbf{d} \sigma_{ge}^j, \tag{7.28}$$

which is analogous to Eq. 7.10. As before, the total field is given be the sum of the probe field and the field scattered by the atoms. The way light propagates in space is encoded in the Green's function.

The power of this formalism is that it does not require any assumption to be made about the dielectric environment of the array. Even if an analytical expression for the Green's function is not readily available for an arbitrary waveguide or cavity geometry, it can often be approximated numerically using finite-difference time-domain (FDTD) simulation software. Note that the equations above reduce to the model described in section 7.2 by setting the Green's function to that of a one-dimensional waveguide.

7.4 Collective effects in arrays of NV centres

In this section, we investigate theoretically if collective effects can enable efficient light-matter interactions with ordered ensembles of solid-state quantum emitters. We focus on the case of colour centers in diamond, as it was recently demonstrated by that arrays of NV centers could be generated with high yield and great accuracy using femtosecond-laser writing techniques [260].

In section 7.2.4, we have seen that an array of two-level atoms spaced by a multiple of $\lambda/2$ coupled to a photonic waveguide could act as a highly reflective mirror. Expanding upon this idea, theoretical results [261] have shown that two such arrays could be combined in order to confine the electromagnetic field in a small region at the centre as with a conventional optical resonator. Moreover, a single defect emitter placed in this region, equidistant from both 'mirrors' as shown in Fig. 7.6b, then exhibits dynamics equivalent to conventional cavity QED, with parameters defined by the properties of the the array. Here, we will focus elucidating the physics of this system in the particular case of when the emitters are NV centers.

This type of geometry is appealing for two main reasons. Firstly, as will be touched upon in section 7.4.3, the regime in which this system evolves is somewhat distinct from what can be attained with dielectric cavities which makes it interesting on a fundamental level. Arrays composed of neutral atoms trapped in the vicinity of a nanofibre, the position of each emitter is defined by the very regular interference pattern generated by two trapping lasers counter-propagating along the waveguide. As a result, creating ordered ensembles with a central 'impurity' atom is potentially challenging. In contrast, laser writing allows the creation of NV centres in arbitrary geometries hence bypassing any kind of restriction stemming form the need to trap individual atoms. Furthermore, although many experiments have demonstrated the interaction of a single NV centre and an optical cavity, attaining the regime of strong coupling has proven a difficult task. In theory, the mirror finesse required in order

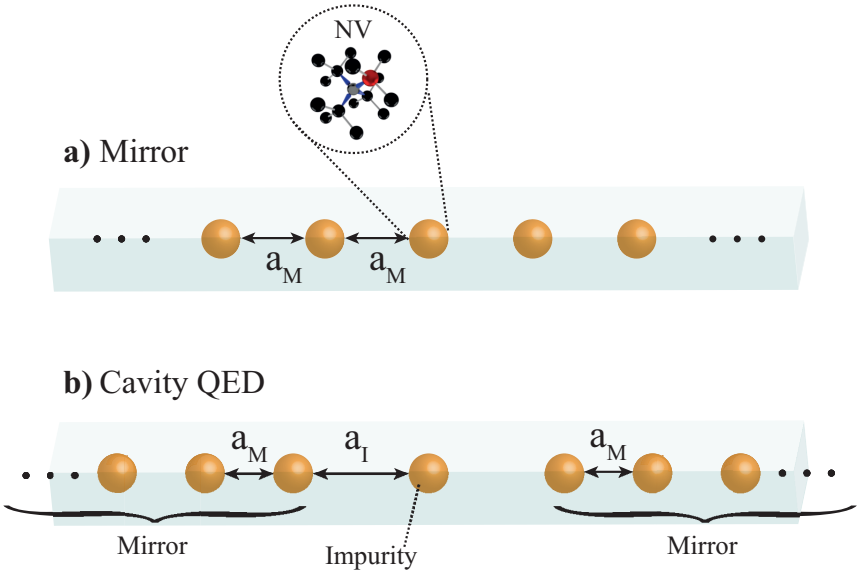

Fig. 7.6 : Schematic of an array of NV centres interacting with a one-dimensional waveguide intwo different configurations: a) 'Bragg mirror' configuration where all the defects are equally separated by a_M, a multiple of $\lambda/2$. b) 'Cavity QED' configuration where a single 'impurity' defect is placed between two mirror arrays. The distance between the impurity to each mirror is $a_I = 3\lambda/4$. The two atomic mirrors form a cavity which enhances the coupling of the impurity defect to the guided mode.

to reach such a regime is much lower in an array-based cavity than in conventional realisations due to collective effects [261]. This result alone makes such a system at least worthy of investigation.

In the following, we will first outline the methods employed in order to accurately simulate the physics of ordered ensembles of NV centres. An array with half-wavelength lattice period (termed 'mirror configuration') will be studied as a initial step before moving on to the full cavity geometry.

7.4.1 Model and simulation methods

Fundamentally, the model we use to simulate arrays of NV centres follows the physics elucidated in section 7.2: we consider an ensemble of emitters with discrete positions which can interact with each other via the guided mode of a photonic waveguide. We make use of two slightly different models. The first is a simpler one-dimensional model described in section 7.2, while the second is the Greens functions formalism of section 7.3 which allows fully three-dimensional simulations. The computational cost of the 3D model limits the size of the system to $N \sim 50 - 100$ emitters and hence we restrict

its use to the study of phenomena which require a three-dimensional representation of the electromagnetic field.

Each colour centre emits into the waveguide at a rate Γ_{1D}, and the subsequent exchange of photons between them influences their quantum state. This interaction leads to the emergence of collective modes spanning the full length of the array which can be excited via an external probe beam. We focus on the zero-phonon line (ZPL) of the NV centres (see Chap. 5), in particular on the optical transition between the $m_s = 0$ spin states of the ground $^3A_2$ and excited ^3E manifolds. In general, the conditions of the system assume a low-strain environment so that spin-mixing in the excited states is negligible. The diamond sample is also cryogenically cooled to 4K so that dephasing effects related to phonon scattering can generally be ignored.

The NV center differs markedly from the ideal two-level system considered in the model described in section 7.2, due to both its electronic structure and the surrounding diamond lattice. The transition between the $m_s = 0$ spin states is not a true cycling transition as the excited state exhibits strong decay into the vibronic manifold of the ground state. The Debye-Waller factor, defined as the part of the total emission from the excited state going into the ZPL is only $\mathrm{DW}_{NV} \sim 0.04$ [262, 211]. Most of the light emitted on the transition is emitted into the phonon sideband and any associated coherence is lost. The excited state of the NV center also decays into the excited singlet $^1A_1$ state via an intersystem crossing. Although the triplet excited state preferentially decays back into the $m_s = 0$ ground state, the zero-phonon line of the NV centre is not a true cycling transition. In this model, all emission paths outside of the ZPL are treated as losses and factored into Γ'. In general, the total decay of an emitter coupled to the waveguide is given by $\Gamma_{tot} = \Gamma_{1D} + \Gamma'$, where Γ' encompasses the emission into the phonon sideband, the portion of the light emitted into the ZPL but lost to non-guided modes, and that lost through non-radiative pathways.

The environment of the NV center also strongly influences its optical properties. Each defect experiences a slightly different environment due to local strain variations in the diamond lattice. As a result, their resonance frequencies can be slightly shifted from one another leading to inhomogeneous broadening. Until now, all of the emitters were assumed to be aligned to each other with dipoles emitting optimally into a pseudo-1D waveguide. As discussed in Chap.5, the NV centre can be generated randomly in any one out of four possible orientations within the diamond lattice. Although preferentially oriented ensembles of defects have been successfully fabricated [263], the great majority of available samples contain randomly oriented emitters. Bearing

this in mind, we investigate both existing systems in order to quantify the benefits of preferentially ordered defects. Furthermore, each centre radiates light following a spatial profile defined by two optical dipoles orthogonal to each other. Fully capturing the interaction of each of these dipoles with the field carried by the waveguide requires a three-dimensional description of the system. To this end, we resort to the formalism outlined in section 7.3 based on Greens functions which allows a vectorial description of the fields and dipoles.

Light propagation in the vicinity of a photonic waveguide is rarely as ideal as that described in section 7.2. A more accurate treatment can be obtained by using FDTD methods [264]. In this way, the electromagnetic field can be fully solved for a waveguide with arbitrary geometry and dielectric properties. Throughout this chapter, we consider a simple diamond waveguide with a rectangular profile surrounded by vacuum. Commercial software (Lumerical MODE Solutions) is employed in order to compute the eigenmodes supported by the structure. Its dimensions are subsequently set to 110x260 nm in order to generate a single-mode waveguide with the field concentrated in the centre, as shown in Fig. 7.7.

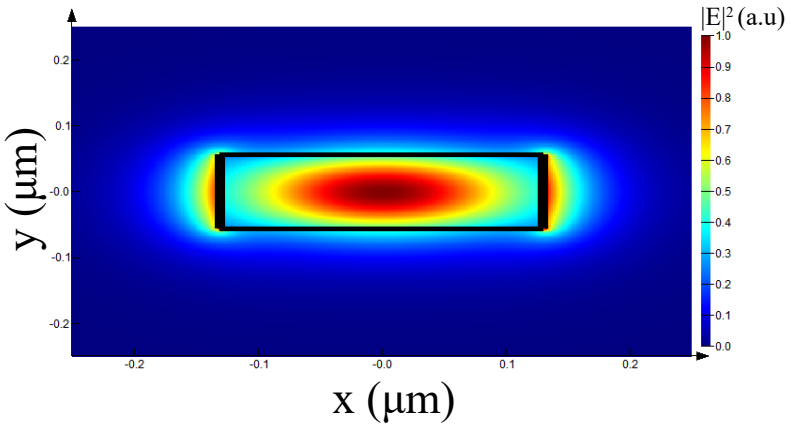

Fig. 7.7 : Transverse profile of the electric field mode guided by the dielectric waveguide used in this section. The structure has a cross-section of dimensions 110x260 nm.

The full Green's function **G** of the system is collected by calculating the value of the electromagnetic field at every point along the waveguide using Lumerical FDTD solutions. As it is necessary to calculate how the field radiated by each emitter propagates along the waveguide, the Green's function is solved independently for each emitter by placing dipoles at the position of each defect in the array. The FDTD simulation also provides a value for the emitter-waveguide coupling. This allows an

estimate of $\Gamma_{1D,NV} = 0.65\Gamma_{ZPL}$ where $\Gamma_{ZPL} = 0.04\Gamma_0$ refers to the fraction of the light emitted into the ZPL. In this chapter, we define $\Gamma_{1D} = \Gamma_{1D,NV}$ unless stated otherwise. The coordinate system is defined as $\hat{\mathbf{x}}$ pointing along the waveguide axis, the $\hat{\mathbf{y}} - \hat{\mathbf{z}}$ plane being transversal to the waveguide and the $\hat{\mathbf{z}}$ being the positive vertical direction. Finally, as colour centres in the array are regularly spaced, we can use the term 'array length' to refer to the number of emitters N.

Given the Green's function, the effective Hamiltonian of the system in the weakly saturated regime can be reconstructed according to Eq. 7.27. We then solve the Schrödinger-like equation in order to obtain the atomic wavefunction in the steady state. All the field properties, including the optical transmission and reflection of the system can finally be recovered using Eq. 7.28.

In practice, it is computationally challenging to calculate $\mathbf{G}$ for an array of more than $N \sim 100$, limiting the scope of the model. For larger simulations, we resort to the use of the more numerically accessible one-dimensional model, which qualitatively captures the behaviour of the system. An alternative approach is to find a set of parameters (N, $\Gamma_1 D$) that exhibits the same behaviour as a large array while being easier to simulate.

7.4.2 Array in 'mirror' configuration

We first choose to investigate an array of NV centres spaced by a multiple of $\lambda_{ZPL}/2$, where λ_{ZPL} is the zero-phonon line wavelength in diamond ($n = 2.417$). In this configuration, an array of atoms has been shown to strongly reflect an incoming probe beam [256]. This case is of particular interest as it constitutes a simple system which can exhibit a clear, experimentally observable signature of the emergence of collective effects. Furthermore, theoretical predictions can be compared with existing experimental realisations using arrays of neutral atoms [256]. An atomic mirror is also a fundamental building block of the an array arranged in a cavity QED configuration. It is thus naturally instructive to understand its optical properties before considering the cavity geometry.

We consider each of the potential aspects of the system which constitute a departure from an ideal one-dimensional array two-level systems, such as positional disorder, inhomogeneous broadening, or NV orientation. As mentioned in section 7.2.4, in the ideal case, the spectrum of the array follows a lorentzian lineshape with a width of $\Gamma' + N\Gamma_{1D}$ peaking on resonance at $(N\Gamma_{1D})^2/(\Gamma' + N\Gamma_{1D})^2$. Spectra and peak reflectivities for a range of parameters are shown for reference in Fig. 7.8.

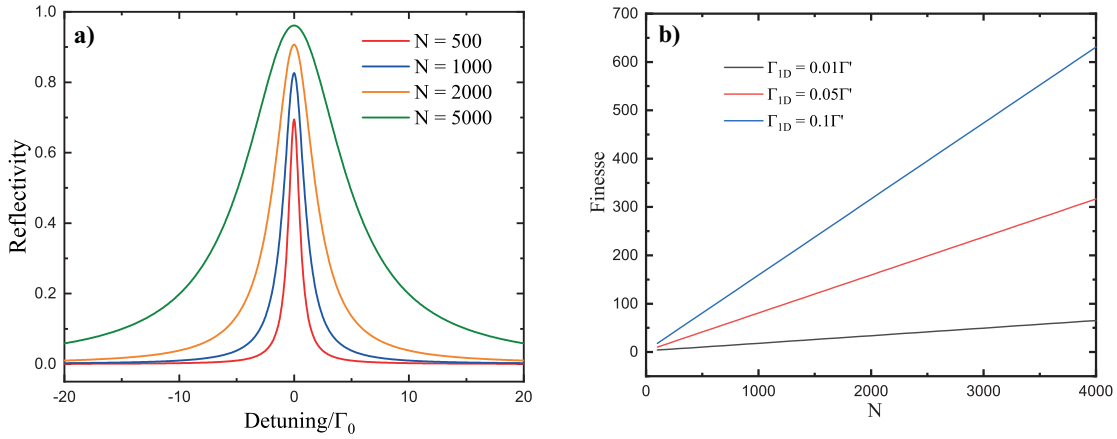

Fig. 7.8 : (a) Reflection spectra for a range of arrays with different emitter numbers. We use $\Gamma_{1D} = \Gamma_{1D,NV}$. (b) Finesse of a cavity with mirrors composed of atomic arrays of N emitters, for a range of waveguide coupling values.

The system can indeed be highly reflective for relatively modest ensemble sizes and waveguide couplings. Furthermore, weak waveguide coupling can to a certain extent be compensated by longer arrays. In the following, each of the imperfections which can occur in an array of NV centers will be treated separately in order to obtain insight into the behaviour of the system.

Fig. 7.9 shows the effect of vacancies in the array. These can occur in the case of an error in the NV centre creation process. This can be addressed via methods with a high chance of generating defects such as laser-writing, boasting yields of up to 99% [260]. Nevertheless, any NV centre which is not resonant with the zero-phonon line frequency due to being in the singlet system or a different charge state will not interact with other emitters in the array and thus also treated as a vacancy.

In practice, missing defects are simulated by associating each site in the array with a finite probability of being vacant. The behaviour of a system with N emitters and N_{vac} vacancies is identical to that of a regular array with $N - N_{vac}$ emitters. Hence, one can accurately account for missing defects by simply generating larger ensembles. This behaviour only holds for arrays in a mirror configuration as all of the emitters are placed at nodes of the field.

We then consider the impact of inhomogeneous broadening on an ideal array of atoms. The zero-phonon line frequency of each defect can be shifted by more than its homogeneous linewidth ($\Gamma_{\text{hom}} = \Gamma_0 \sim 100\,\text{MHz}$ for the NV centre [173]) depending on its electromagnetic environment. In this model, we shift the resonance of each emitter by a random value sampled from a Gaussian distribution with a width Γ_{inh}. Spectra

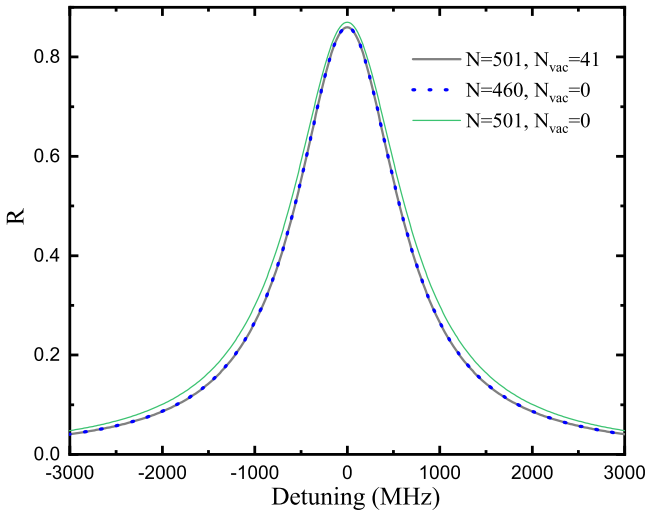

Fig. 7.9 : Reflection spectrum of an array with 501 sites out of which $N_{vac} = 41$ are vacant, showing perfect overlap with that of another array with the same number total of emitters ($N = 460$) but no vacancies.

and peak reflectivities are plotted in Fig. 7.10 for a range of parameters averaged over 10 sampling runs.

As could be expected, the performance of the mirror strongly deteriorates under the influence of inhomogeneous broadening, leading to reduced reflection and distorted lineshapes. Indeed, the reflectivity is seen to drop by almost a third when the centres are distributed over the homogeneous linewidth of a single emitter. Employing larger ensembles can help to mitigate this effect by increasing the peak reflectivity and broadening the ensemble. In order to observe collective effects, NV centres should be generated while causing as little damage to the diamond lattice as possible so that the broadening of the ensemble is minimised. The choice of material is also paramount as impurities in the crystal also lead to a wider inhomogeneous linewidth.

When using methods such as laser writing or implantation masks [265] to create arrays of NV centres, positional errors are necessarily involved. These can arise due to the nature of the mask or the diffraction limit associated with the focusing of the writing laser. Furthermore, defects can also diffuse spatially during the thermal annealing process necessary to create NV centres after nitrogen implantation. We separate the case where the disorder is along the array axis (δx) from that of transverse irregularities (δy and δz). The position of each defect is given by $x_i + \delta x_i$ where δx_i is

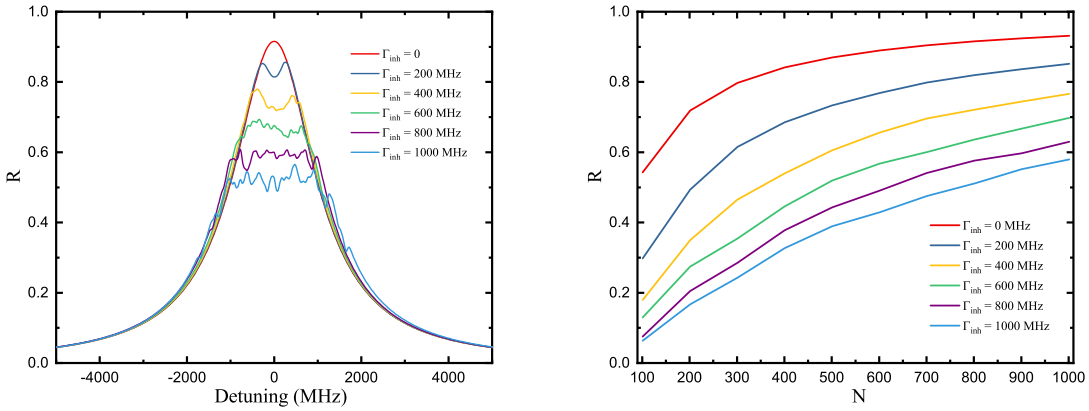

Fig. 7.10 : (a) Reflection spectra for array of $N = 1000$ NV centres, shown for a range of inhomogeneously broadened linewidths. (b) Peak reflectivity as function of array length for various values of Γ_{inh}, averaged over 10 samples.

sampled randomly according to a Gaussian distribution with width Δx. The optical response of the array is shown in Fig. 7.11 for different values of disorder.

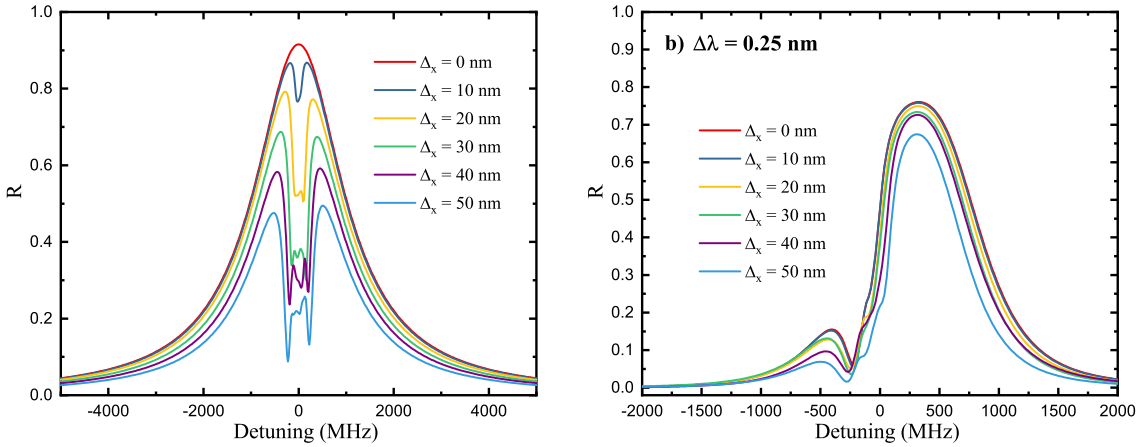

Fig. 7.11 : Reflection spectra for arrays of $N = 1000$ atoms with different values of Δx, shown for a lattice detuning of (a)$\Delta\lambda \sim 0\,\text{nm}$ and (b) $\Delta\lambda \sim 0.25\,\text{nm}$

The error margin allowed in the position of the emitters along the array is quite narrow (this is accentuated by the high refractive index of diamond), with the reflectivity dropping by $\sim 50\%$ for $\Delta x = \lambda_{\text{ZPL}}/10$. This is to be expected as in the limit of large irregularities, the behaviour of the system tends to that of a conventional atomic ensemble. The decrease in performance is difficult to counteract by increasing N, as

even a large ensemble of disordered atoms does not typically reflect light. However, detuning the lattice period by a small value $\Delta\lambda \sim 0.25\,\text{nm}$, i.e. using a system where the lattice period is $a = \lambda/2 + \Delta\lambda$ can alleviate the effects of axial disorder. This phenomenon has also been observed experimentally with trapped atoms, for example in Ref. [256]. Results for this configuration are shown in figures 7.11(b) and 7.12, where the spectrum is shown shifted from resonance, but does not exhibit the central dip present when $\Delta_\lambda = 0$. Crucially, the peak reflectivity is much less affected by the disorder. However, controlling the array fabrication methods to a degree of precision such that this effect can be harnessed is a challenging task.

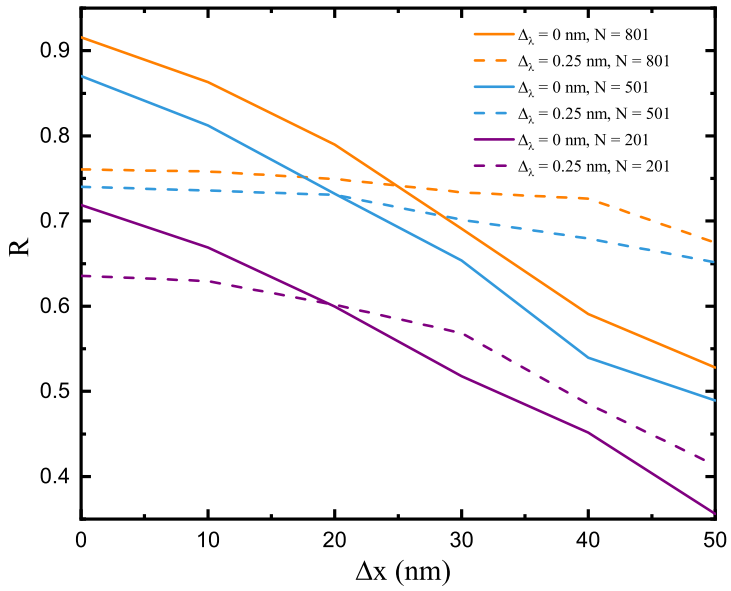

Fig. 7.12 : Peak reflectivities for a range of values of N as a function of array disorder, showing the cases where $\Delta\lambda \sim 0\,\text{nm}$ in solid lines and $\Delta\lambda \sim 0.25\,\text{nm}$ in dotted lines.

On the other hand, disorder transverse to the array axis is seen to be much less critical as long as the emitters remain within the guided mode profile. Defects placed further away from the mode centroid experience a reduced coupling while translates directly to a decrease in Γ_{1D}. The behaviour of the array is fundamentally unchanged, and hence the lineshape remains Lorentzian.

Finally, we consider an array composed of defects with no preferential orientation. As mentioned in Chap.5, the NV centre can be oriented in one of four possible different directions defined by the structure of the diamond lattice. Each of these orientations forms an angle of 70.5deg with the three others. We randomly define the orientation of

each emitter in the array and simulate its interaction with the waveguide field according to Eqs. 7.27 and 7.28. In our FDTD simulations, the waveguide is also seen to weakly guide the x and z components of the field. We can choose to define the waveguide axis with respect to the diamond lattice in such a way that for one orientation, one of the two dipoles of the NV is aligned to either one of the x, y or z directions in the waveguide frame. The spectrum of the array is shown in reflection for each of these possibilities in Fig. 7.14.

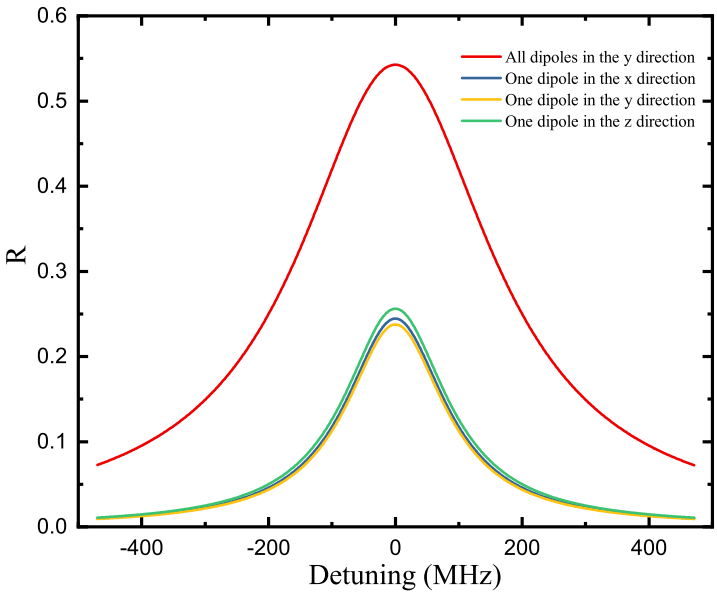

Fig. 7.13 : Reflection spectra of arrays where the defects are randomly oriented contrasted with the case of a sample with preferentially oriented emitters. Here, we use $N = 100$.

When the NV dipole is not ideally oriented, it does not couple as efficiently to the waveguide mode. This reduced coupling causes an unwanted drop in reflectivity, minimised when one dipole is oriented in the y direction. This result confirms the intuition that using arrays with defects oriented parallel to each other is greatly beneficial to the observation of collective effects. For completeness, results including both axial positional disorder and inhomogeneous are provided in Fig. 7.13.

The signature of collective effects in the system, in the form of a strongly reflective peak close to resonance, seems relatively resilient to the imperfections studied here. Recent experimental results quote a positional accuracy of ~ 33 nm by using laser-writing techniques, for which a clear signal can still be expected. Arrays with

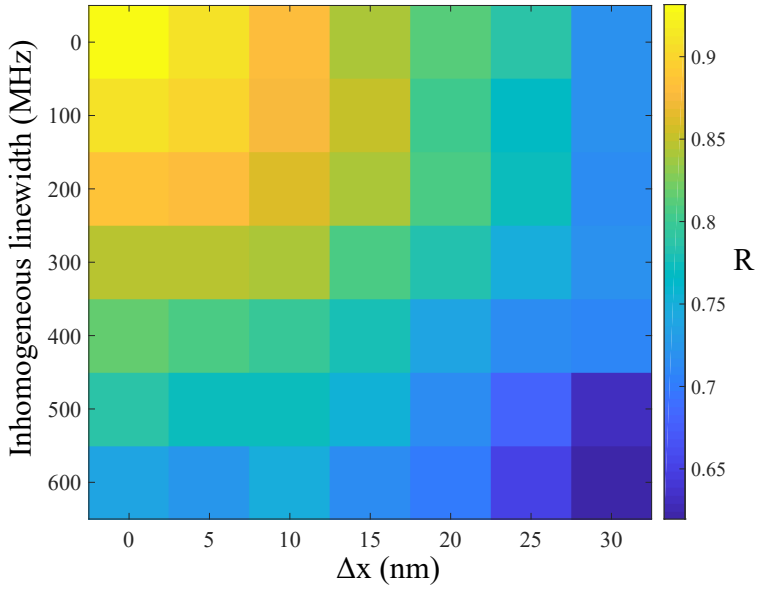

Fig. 7.14 : Peak reflectivity of array systems including both axial positional disorder and inhomogeneous broadening. Here, we use $N = 1000$.

detuned lattice constants provide an elegant way of accounting for positional disorder and worth investigating further, although the approach would be easier to implement in trapped atom arrays. In general, transverse disorder and the lattice filling factor have relatively little influence on the physics of the system thereby alleviating some of the implementation challenges. Ensembles of NV centres typically exhibit inhomogeneously broadened lines with $\Gamma_{\text{inh}} > 1\text{GHz}$, which represents the largest obstacle to an experimental realisation of this system. This issue can be mitigated by increasing the number of defects, but it is still crucial to obtain a sample with linewidths as narrow as possible.

7.4.3 Cavity QED with arrays of NV centres

A cavity can be formed around a single emitter by placing it in between two reflective arrays, somewhat analogously to using Bragg reflectors. The physics of such a system, where the spacing between the central 'impurity' emitter and the mirrors is given by $a_I = \frac{3}{4}\lambda$ (see Fig. 7.6b), is accurately described by the Jaynes-Cummings model [261].

Although array-based cavities do behave according to cavity QED, the nature of the system leads to a different parameter regime to that accessible with standard dielectric cavities. In particular, a field excitation contained within the cavity is also an

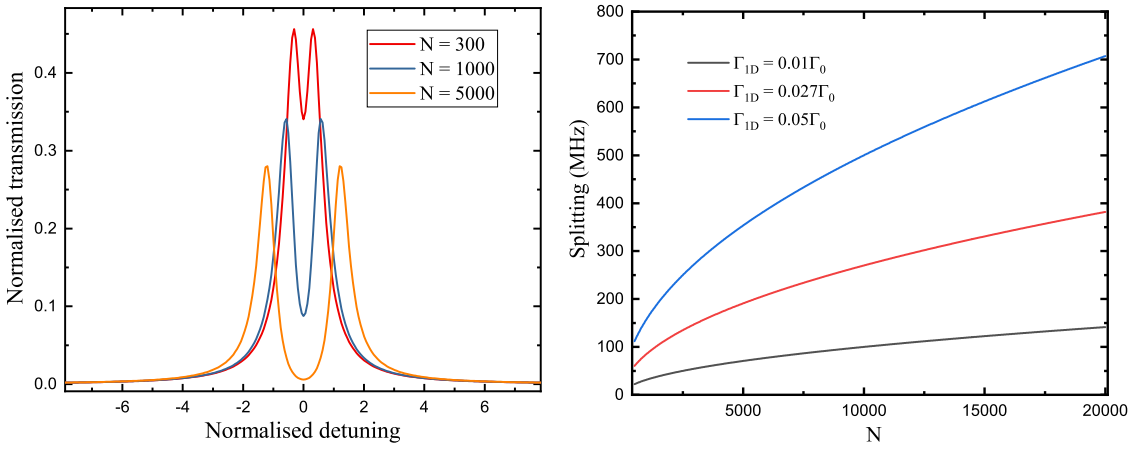

Fig. 7.15 : (a) Spectra for arrays in the cavity configuration, showing the normal mode splitting characteristic of the strong-coupling regime of cavity QED. Here, $\Gamma_{1D} = \Gamma_{1D,NV}$. (b) Normal mode splitting as a function of emitter number, for a range of values of Γ_{1D}.

atomic excitation of the mirror array. This excitation is thus lost at the *atomic* decay rate. Furthermore, due to destructive interference between the emission from the two mirror arrays, a cavity excitation cannot be emitted into the waveguide mode and its decay rate is thus given by $\kappa = \Gamma'$. The central emitter can emit into both guided and unguided modes of the field and as a result its decay rate is given by $\Gamma_I = \Gamma_{1D} + \Gamma'$. This leads to a very particular regime where the energy and coherence are maintained longer within the cavity than in the central atom. Figures of merit associated with cavity QED can then be defined in terms of the array parameters. For example, the interaction of the 'atom' with the 'cavity' is quantified by $g = \sqrt{N}\Gamma_{1D}$. Similarly, the cooperativity is given by

$$C = \frac{g^2}{\kappa\Gamma_I} = \frac{N\Gamma_{1D}^2}{\Gamma'(\Gamma' + \Gamma_{1D})}. \tag{7.29}$$

As a side note, the particular parameter regime these array-based CQED systems evolve in preclude any Purcell enhancement due to the particularly long lifetime of a cavity excitation.

Transmission spectra are shown in Fig. 7.15a for an ideal 1D array, revealing twin peaks corresponding to the eigenstates of the dressed atom-cavity system. The splitting is well approximated by $N\Gamma_{1D}$, and can be observed even with low waveguide coupling. Indeed, as the cavity excitation is so long-lived, reaching the strong-coupling regime where $g > \kappa, \Gamma_I$ is achievable even with relatively low finesse. This intuition

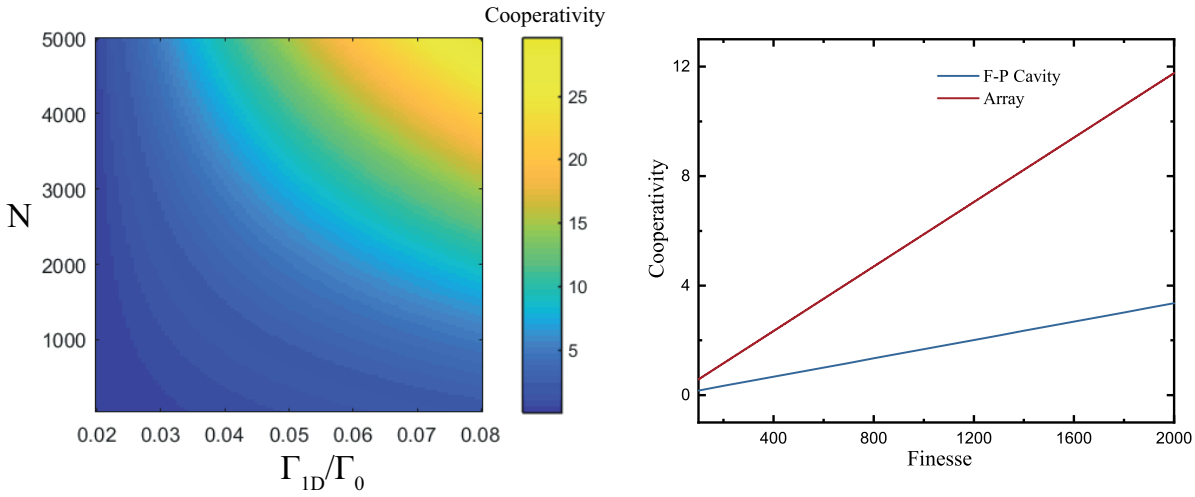

Fig. 7.16 : (a) Cooperativity of the impurity-cavity system as a funcion of the number of emitters and waveguide coupling. (b) Cooperativity of an array-based CQED system as a function of mirror finesse calculated for $\Gamma_{1D} = \Gamma_{1D,NV}$. Equivalent values for an NV centre coupled to a dielectric cavity are included for reference, inspired from Ref. [262]. An indication of the parameters required for an array to reach a certain finesse value can be found in Fig. 7.8.

is supported by results in Fig. 7.16a, where cooperativity and normal mode splitting values are plotted as a function of the main array parameters. In this parameter regime, where $\kappa \lesssim \gamma$ and $g \gtrsim \kappa, \gamma$, strong coupling can be attained for lower cavity finesses than conventional dielectric cavities which typically exhibit high values of κ. This is illustrated in Fig. 7.16b, comparing the cooperativity of an array-based CQED system with that of an NV centre placed inside a dielectric microcavity.

Due to computational restrictions, the array size we could accurately simulate is limited to $N \sim 10^3$. For these short arrays and realistic couplings $\Gamma_{1D} \leq 0.03\Gamma_0$, the system sits outside of the strong coupling regime. Consequently, we instead choose to qualitatively investigate systems with values of g and C equivalent to an array of $N = 10^4$ and $\Gamma_{1D} \leq 0.027\Gamma_0$ by using another array with $N = 517$ and $\Gamma_{1D} \leq 3\Gamma_{1D,NV}$.

One advantage of the model used here is that the dynamics of each atom can be solved for. The excited state population $P_e(t)$ of the central defect is plotted as a function of time in Fig. 7.17 for a collection of Γ_{1D} values with constant Γ', given $P_e(0) = 1$. Rabi oscillations at a rate of $\Gamma_{1D}\sqrt{N}$ are clearly visible for higher values of waveguide coupling and a clear signature of energy exchange between the cavity and the central emitter. The excitation decays following an exponential envelope with a constant equal to $\Gamma' + \Gamma_{1D}$. For all the results presented in this section, only the

central 'impurity' emitter is weakly driven with an optical field inserted transversally to the waveguide axis.

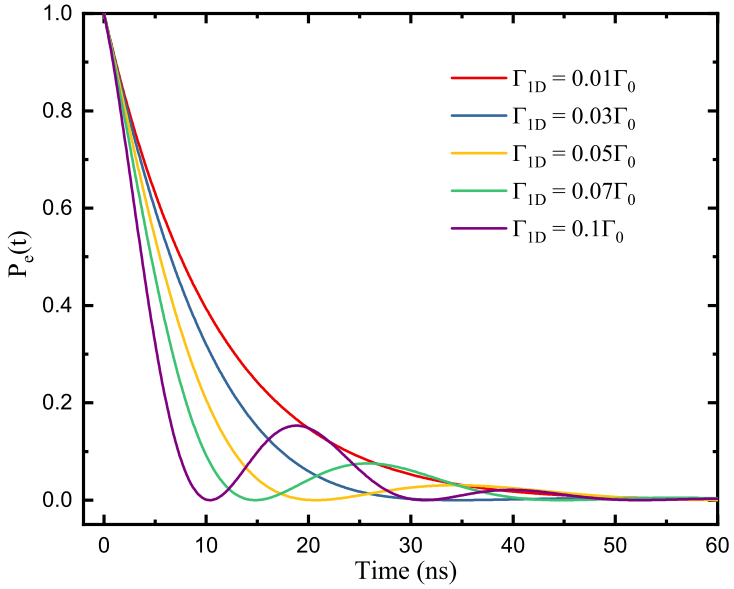

Fig. 7.17 : Population of an initially excited impurity emitter as a function of time, shown for a range of values of Γ_{1D}, keeping Γ' constant. Rabi oscillations can be observed, showing the coherent transfer of the excitation to a spin-wave distributed over the mirror atoms.

In order to investigate the feasibility of reaching strong coupling using an array of NV centres, we once again consider the impact of potential imperfections in the system. Spectra are provided in Fig. 7.18a for a range of inhomogeneous linewidths.

Since inhomogeneous broadening leads to lower mirror reflectivity, it can be expected that the cavity finesse will also drop. This naturally leads to a blurring out of the features characteristic of efficient emitter-cavity coupling - and indeed, the spectrum reverts entirely to a single peak for inhomogeneous linewidths $\Gamma_{\text{inh}} \geq 6.5\Gamma_0$. This issue can be addressed by using longer arrays, provided that the central atom remains close enough to resonance. As in conventional cavity QED, detuning between the 'atom' and the resonator places the system in the dispersive regime, where the state of the two sub-systems are less correlated. The excited state population is also shown in Fig. 7.18b for an initially excited central emitter. The damping on the oscillations

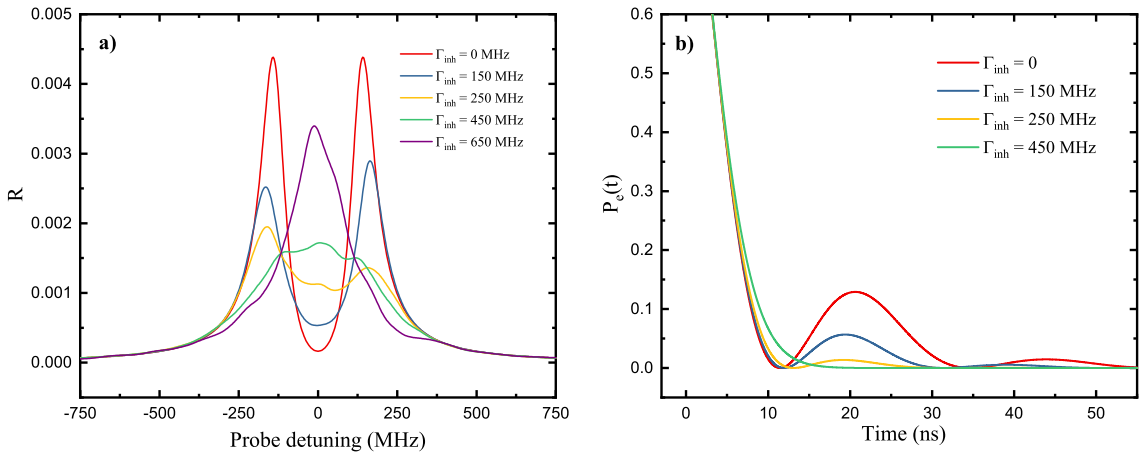

Fig. 7.18 : (a) Spectra and (b) population dynamics of an array in cavity configuration, shown for a range of inhomogeneous linewidths ($N = 517$, $\Gamma_{1D} = 3\Gamma_{1D,NV}$).

increases with Γ_{inh} until they disappear altogether in what can be interpreted as the system leaving the strong-coupling regime.

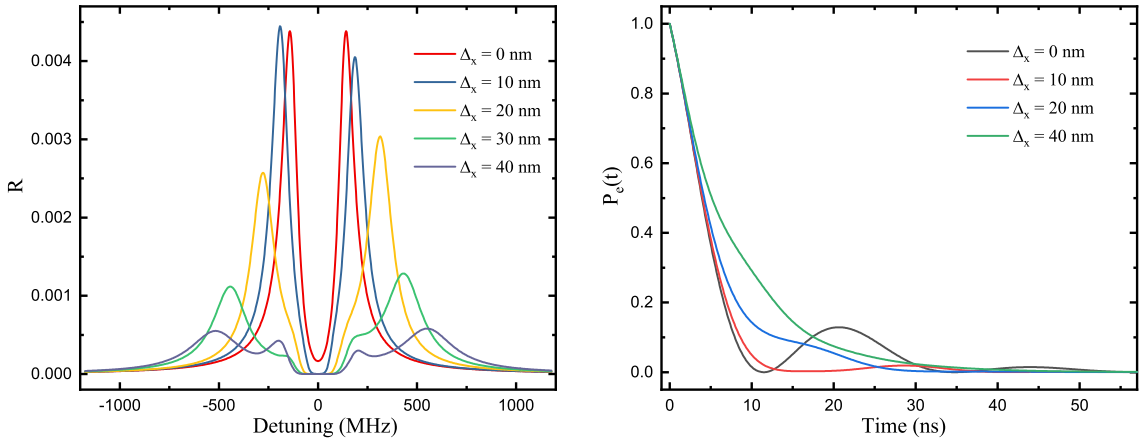

Fig. 7.19 : (a) Spectra and (b) population dynamics of an array in cavity configuration, shown for a range of values of axial positional disorder Δ_x. ($N = 517$, $\Gamma_{1D} = 3\Gamma_{1D,NV}$).

Positional errors are examined in Fig. 7.19. Although the double peak structure remains visible until relatively high values of Δx, Rabi oscillations are quickly suppressed as shown in Fig. 7.19b. The confinement of the electromagnetic field between the two mirror arrays is entirely dependent on the emitters in such a way that an 'impurity' region arises. In the mirror configuration, the lack of interference due to the

mispositioning of an atom could be, to some extent, covered for by another emitter correctly placed further down the array due to the periodicity of the system. Here, if the defects in the central region are disordered the nature of the atom-cavity system itself rapidly breaks down. In the presence of axial disorder in the lattice, the central emitter couples unequally to different atoms in the mirror array. As a result, an initial excitation is distributed to the many collective modes of the array, decaying rapidly and causing the suppression of Rabi oscillations.

Unfortunately, only a few tens of NV centres can be simulated using the three-dimensional model necessary in order to consider off-axis disorder. Strong coupling cannot be observed with realistic values of Γ_{1D} in such short arrays. Nevertheless, we can obtain an insight into the effects induced by 3D imperfections by artificially increasing the emitter-waveguide coupling. We then choose Γ_{1D} such that the cooperativity of the system matches that of an array of $N = 10^5$ atoms with $\Gamma_{1D,NV}$. Such parameters are used in figures 7.20 and 7.21.

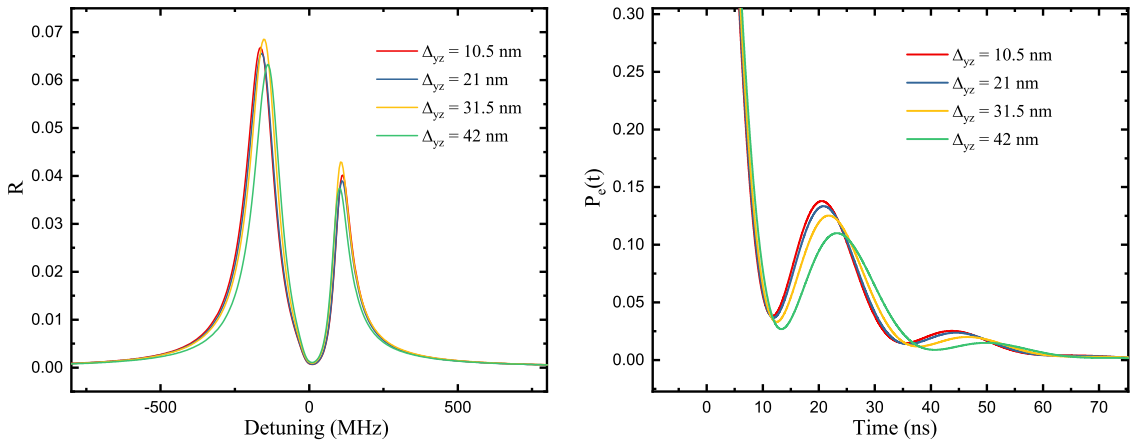

Fig. 7.20 : (a) Spectra and (b) population dynamics of an array in cavity configuration, shown for a range of values of transverse positional disorder Δ_{yz}. ($N = 41$, $\Gamma_{1D} = 11\Gamma_{1D,NV}$).

Increasing the value of Δy and Δz straightforwardly reduces the mode splitting, as can be expected from the reduced coupling of the defects to the waveguide. An equivalent decrease in the Rabi oscillation frequency can be seen in Fig. 7.20b. In general, positional disorder in the plane transverse to the waveguide axis is significantly less critical than axial positional errors, which is consistent with the observations made on the mirror configuration.

Similar behaviour can be observed when the centres are randomly oriented. As was done previously, the pointing of each defect is randomly selected out of the four possible orientations it can take. Sub-optimally oriented dipoles interact less efficiently with the guided mode, leading to a lower atom-cavity coupling. The dynamics of the system are also investigated in Fig. 7.21b, showing similar results for all possibilities. In all cases, the coupling is significantly lower than if all the defects were optimally aligned.

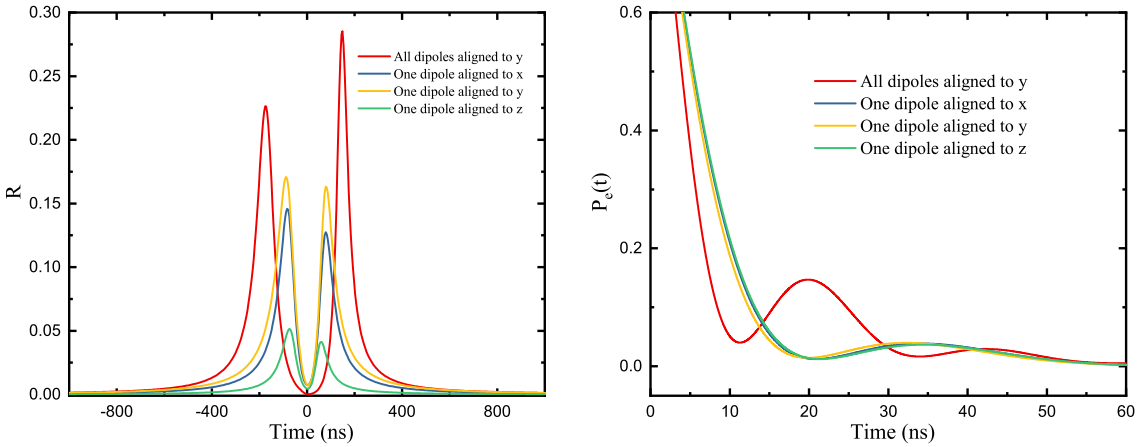

Fig. 7.21 : (a) Spectra and (b) population dynamics of an array in cavity configuration where the defects are randomly oriented contrasted with the case of a sample with preferentially oriented emitters. ($N = 41$, $\Gamma_{1D} = 11\Gamma_{1D,NV}$).

Overall, building an efficient atom-cavity system has more stringent requirements on the array parameters than simply observing Bragg-like reflection effects. As most of the light emission from the NV centre is intrinsically lost to incoherent sideband emission, it is critical that the waveguide coupling of each emitter to the waveguide be as high as possible. In particular the system is not particularly robust to inhomogeneous broadening and values of $\Gamma_{inh} \leq 500$MHz are necessary in order to expect high atom-cavity couplings. This issue can be mitigated to some extent by Stark-shift tuning the zero-phonon line of individual centres with local electric fields [266]. Such an approach would however represent a fabrication challenge, as currently state of the art integrated platforms make use of 2 μm-wide electrodes [267].

Positional accuracy of each defect must be defined to less than 20 nm in the axial direction, which represents another technical challenge. Yet, the necessary regime is perhaps more accessible than one could think due to the outstanding performance

of laser-writing techniques. Indeed, the accuracy of $\Delta_x \sim 33\,\text{nm}$ demonstrated by Chen *et al.* [260] suggests the required values for this protocol could be reached with moderate technical advancements. Alternatively, NV creation techniques using AFM implantation have also demonstrated remarkable accuracies although the yield is not as easily controlled [268, 269]. As the system is fairly robust to transverse positional disorder, improvements on the spatial accuracy of fabrication techniques are only required in a single dimension. Results suggest that using an array where all the of NV centres are aligned parallel to each other is highly desirable. In this case, the defects should be oriented so as to point into the array axis - their dipoles will then be aligned perpendicularly to the waveguide and hence couple optimally to the guided mode. Preferentially oriented arrays have been demonstrated by feeding back onto the laser-writing process using the NV fluorescence signal [260].

7.5 Conclusion

A versatile formalism capable of capturing complex collective interactions in arrays of quantum emitters coupled to dielectric structures was presented. This model was adapted to investigate the imperfections relevant to the case of chains of NV centres in diamond. Two possible array geometries are chosen for study. In the first, the system behaves similarly to a Bragg reflector. This effect is shown to be quite robust, providing a reliable signal for the presence of collective effects in the array. Simulation results suggest that these effects could indeed be observed in an experimental setting.

Looking towards the development of efficient quantum light-matter interactions in reproducible solid-state devices, we then investigate a configuration where a single 'impurity' defect is placed between two reflective arrays. The physics of this system accurately follows the Jaynes-Cummings model for Cavity QED, with the impurity emitter coupling to a cavity composed of the two reflective arrays. Theory suggests that the strong coupling regime can be reached in such an array with relatively low cavity finesse. While the technical requirements necessary in order to observe collective effects are arguably higher than for the mirror array, they can be attained given moderate technological improvements.

Although we have shed some light on the rich physics of light-matter interactions in atomic arrays, much remains unexplored. In particular, only two configurations have been studied but ensembles with different lattice spacings also show promise for other protocols such as quantum memories [270]. Furthermore, the system we

have chosen to explore is limited by the optical properties of the NV centre. An interesting avenue for further research would be to investigate arrays of group-IV defects in diamond (such as the silicon and germanium vacancies) which exhibit much higher Debye-Waller factors as well as narrower inhomogeneous linewidths. There is also much scope for investigating the interaction of solid-state defects with more complex dielectric structures such as photonic crystals. For instance, a recent study has shown that strong nonlinearities could be observed if an emitter is placed close to the band-edge of a photonic crystal waveguide [271]. We have thus laid the groundwork allowing the simulation of a wide range of physical systems in order to assist in the development of the next generation of quantum optical solid-state platforms.

Chapter 8

Conclusion and outlook

8.1 Summary

Throughout the course of this work, we investigated new approaches to quantum light-matter interactions in solid-state platforms. The first portion of the thesis concerns the development of quantum memories in atomic ensembles and in particular the atomic frequency comb protocol which is particularly suited to inhomogeneously broadened system. Although AFC protocols have been successfully demonstrated in the solid-state, most implementations are limited in bandwidth due to their reliance on the individual hyperfine states of rare-earth ions such as Pr^{3+}:Y_2SiO_5. In Chapter 4, we reported the first realisation of a broadband atomic frequency comb in Pr^{3+}:Y_2SiO_5, prepared via the direct application of an optical frequency comb generated by an ultrafast laser. The quality of the AFC preparation was evaluated by implementing the storage and retrieval of GHz-wide classical pulses. Maximal efficiencies of $\eta \sim 20\%$ were recorded, constituting a strong proof-of-principle demonstration.

As the spectral hole burning regime prevents access to traditional spin-wave storage, another approach to on-demand readout is put forward, which relies on two-photon absorption. By combining the AFC protocol with the ORCA protocol, read-out of the memory depends on the satisfaction of a phase-matching condition reliant on the application of a control field. This field can be switched on or off at will, enacting an on-demand quantum memory operation. Chapter 4 includes initial results towards the realisation of the ORCA protocol in Pr^{3+}:Y_2SiO_5. Two-photon transitions in the $^3H_4 \leftrightarrow ^3F_3 \leftrightarrow ^1D_2$ ladder system are investigated spectroscopically. We observe absorption on the upper transition conditioned on the presence of an optical field on the lower transition, as well as detuned two-photon transitions. This confirms the

observation of a key mechanism for the implementation of the ORCA protocol in this system.

A broadband atomic frequency comb can also be built by resorting to a storage medium with a wider ground state splitting. In Chapter 6, we followed this intuition and investigated AFC preparation techniques in ensembles of diamond NV centres. A novel approach to spectral hole burning was investigated, relying on manipulation of the charge state of the defect. Optical ionisation of NV centres was investigated, and the dynamics were favourable to the implementation of spectral hole burning techniques. A preparation sequence was designed, based on the direct application of a pulsed laser as in Chapter 4. Using this method, we reported the first demonstration of an atomic frequency comb in this system.

When designing any hybrid quantum light-matter interface, one of the most important aspects is the efficiency of the interaction process. The numbers approach embodied by atomic ensembles is attractive, but also limited by the low probability a single photon has of interacting with each emitter. In Chapter 7, we consider the greater picture and investigate solid-state atomic arrays, an interesting system which promises to open the way for new light-matter interaction protocols. We theoretically investigated collective effects in arrays of diamond nitrogen-vacancy centres coupled to photonic waveguides. The optical properties of atomic arrays were shown to diverge heavily from that of disordered ensembles. Depending on its geometry, an array of NV centres exhibits high reflectivity, which then can be used to build a monolithic optical cavity around a single defect. We studied the robustness of collective effects under various realistic imperfections, concluding that atomic arrays are a promising approach to implementing cavity QED protocols with NV centres.

Through these results, our hope is that we have successfully introduced novel avenues for research towards the development of light-matter interactions in the solid state. This work can be built upon in many directions, some of which will be touched upon in the following section.

8.2 Outlook

In this final section, we will describe avenues for further research, from technical improvements to potential new directions.

8.2.1 Increased broadband AFC efficiencies in Pr^{3+}:Y_2SiO_5

The results presented in Chapter 4 showcase the power of an ultrafast laser for spectral hole burning. However, the experiment in its current state is far from being optimised. The properties of the atomic frequency comb, and thus the efficiency of the storage and retrieval processes, are limited by three main factors. First and foremost is the quality of the optical frequency comb generated by the burning laser. Due to fluctuations in the dye jet profile as well as its thermal environment, the laser spectrum is unstable which leads to a broadening of its features as well as a slow drift in centre frequency. As a result, the transparency windows burnt into the atomic ensemble are wider than the hyperfine state splitting, thereby reducing the AFC contrast. This effect can be solved by actively stabilising the laser system, which would go a long way towards the optimisation of the comb profile.

The AFC efficiency is also limited by the optical depth of the Pr^{3+}:Y_2SiO_5 crystal. This issue will be addressed by using stoichiometric samples with higher ion densities or photonic structures such as waveguides or cavities allowing for more efficient light-matter interaction.

A final limiting factor is the movement of the cryostat system caused by the compression cycle. The presence of these vibrations means that different sub-ensembles are spatially addressed at different times, according to a cycle which does not match that of the experiment. One approach to solving this, inspired by Gundogan *et al.*[164], is to synchronise the pulse sequences to the vibrations of the cryostat. This can be done by building a Michelson interferometer where one mirror is attached to the cold finger, allowing the collection of an optical signal in phase with the cryostat cycle which can then be converted into a TTL signal used to trigger the experiment.

8.2.2 An ORCA quantum memory in Pr^{3+}:Y_2SiO_5

As was detailed previously, the issue of spin-wave storage will be addressed by combining the AFC and ORCA quantum memory protocols. This exciting approach has the benefit of also being telecom-compatible through the $^3H_4 \leftrightarrow ^3F_3$ at 1550 nm. Initial characterisation work of the relevant two-photon transition recorded relatively low absorption contrasts in a continuous-wave setup. Further measurements are required to determine if this is due to weak oscillator strengths or to fast decay of the $^3F_3$ level limiting its steady-state population. We plan to shortly shift towards a pulsed setup allowing for dynamic spectroscopy of the system. Pulsed light will be provided at

995 nm by a Ti:Sapphire laser and at 1550 nm by modulating the EDFA intput with an EOM. Using this setup, the decay rates of the relevant states could be measured with rephasing spectroscopy techniques [130, 131]. The higher peak power provided by pulsed excitation will also lead to higher absorption contrasts. This setup is also necessary for the implementation of the ORCA memory, which constitutes the next step towards the realisation of the full storage protocol.

8.2.3 AFC light storage in nitrogen-vacancy centres

The broadband atomic frequency comb in Chapter 6 was prepared using a technique similar to that implemented in Pr^{3+}:Y_2SiO_5. The experiment would greatly benefit from the improvements to the laser and cryostat systems described above. The implementation of the AFC protocol in NV centres first requires an investigation of comb profiles as a function of burning frequency, time and power. This could not be achieved at the time due to the low signal-to-noise ratio of the experiment. The SNR was limited many factors, the first being optical power in the burn and reset beams setting an upper bound on the probing window within a given pulse sequence. Increased power for off-resonant excitation of the ensemble can be obtained by using another laser specifically for this purpose instead of diverting power from the system used to pump the dye laser. The most significant noise source was leakage of the AOMs used for optical switching, which will be reduced in further experiments via additional temporal filtering with cascaded modulators. Using a diamond sample with polished facets will also be a requirement going forward, as the signal collection efficiency was heavily limited by distortion of the optical mode. We also aim to account for cryostat vibrations via the interferometric setup mentioned previously.

When atomic frequency combs with higher contrasts can be successfully prepared, we can re-attempt the storage and retrieval of classical pulses on the zero-phonon line of the ensemble. Applying the spectral hole burning technique with a pulse train with a faster repetition rate would also make for easier observation of rephasing echoes. Currently, the AFC structure has peaks separated by 80 MHz, meaning that we expect an echo 12.5 ns after the read-in pulse is absorbed. This delay is comparable to the excited state lifetime of the NV centre recorded at 12 ns [272]. This limits the achievable rephasing efficiencies and can be solved by preparing an AFC with a larger peak spacing.

Once AFC rephasing echoes have been observed in the system, the full protocol including spin-wave storage can be implemented. This requires the preparation of a

lambda-system in ensembles of NV centres, which can be achieved via the application of an external magnetic field [226, 232].

8.2.4 Collective effects in arrays of solid-state defects

In Chapter 7, we presented theoretical results concerning light-matter interactions in arrays of nitrogen-vacancy centre. This study is by no means exhaustive, and the rich physical landscape of collective effects in atomic arrays is still far from fully explored. We focused on a particular use case, where atomic mirrors are harnessed to demonstrate strong-coupling between a cavity field and a single NV centre. A potential avenue for further research includes applying such a system to schemes relying on strong coupling to achieve high-fidelity readout of the NV centre spin state [273]. Furthermore, cavity QED systems which do not quite reach the strong-coupling regime are also of interest for quantum information processing applications. For example, this includes cavity-induced funnelling of emission into the zero-phonon line of the NV centre, thereby increasing its Debye-Waller factor [213]. Another potential application is cavity-assisted Raman single-photon generation. The photons emitted on the zero-phonon line of NV centres have low indistinguishability properties due to dynamic effects such a spectral diffusion. A cavity detuned from one arm of a lambda-system prepared in the NV ensemble can assist the emission of single photons conditioned on the application of an optical control field detuned the same amount from the second transition. The properties of the single photons emitted in this way are determined by those of the control field, leading cleaner emission and greater flexibility [274].

Another configuration, where the emitters resonant with a wavelength λ are separated by an odd multiple of $\lambda/4$ has only been mentioned in passing in our work. In this case, the absorption of the system is maximised which is of interest for many applications. However, the enhancement in absorption scales unfavourably with the waveguide coupling, which is relatively low in NV centres due to their weak ZPL emission. Using systems with a higher Debye-Waller factors such as silicon-vacancy centres represents another avenue for research. In future work, we plan on modelling the case of group-IV colour centres in diamond which have already been integrated with nanophotonic devices to great effect [275].

NV centres were chosen as technology to fabricate arrays of defects already exists through laser writing and AFM implantation techniques. This opens up the way for an experimental investigation of the schemes investigated in Chapter 7. The first step in this direction would be to observe high reflection coefficients induced by cooperative

effects in these arrays. The results could then be compared with existing realisations with trapped neutral atoms [256] in order to evaluate the performance of the system.

Finally, as the model we used relies on the system being weakly saturated, its optical response is mostly linear in nature. By resorting to a more general formalism capable of taking into account multi-excitation states, a new range of interesting phenomena could undoubtedly be uncovered as hinted by initial studies by Asenjo-Garcia *et al.* [245]. In particular, we have given little attention to the photon statistics of the light emitted by the array throughout our investigations. The second order correlation function $g^{(2)}$ of the output field for a system supporting more than one excitation could lead to potentially interesting observations. Our model also implicitly assumes that emitters cannot interact via light emitted into free space. This additional interaction channel, which becomes prevalent when the distance between atoms is less a quarter of their resonance wavelength, is certainly worth investigating in further work.

References

[1] T. D. Ladd, F. Jelezko, R. Laflamme, Y. Nakamura, C. Monroe, and J. L. O'Brien, "Quantum computers," *Nature*, vol. 464, no. 7285, pp. 45–53, 2010.

[2] N. Gisin, G. Ribordy, W. Tittel, and H. Zbinden, "Quantum cryptography," *Reviews of modern physics*, vol. 74, no. 1, p. 145, 2002.

[3] C. L. Degen, F. Reinhard, and P. Cappellaro, "Quantum sensing," *Reviews of modern physics*, vol. 89, no. 3, p. 035002, 2017.

[4] R. P. Feynman, "Simulating physics with computers," *Int. J. Theor. Phys*, vol. 21, no. 6/7, 1982.

[5] M. Lewenstein, A. Sanpera, and V. Ahufinger, *Ultracold Atoms in Optical Lattices: Simulating quantum many-body systems*. Oxford University Press, 2012.

[6] B. Schumacher, "Quantum coding," *Physical Review A*, vol. 51, no. 4, p. 2738, 1995.

[7] D. Deutsch, "Quantum theory, the church–turing principle and the universal quantum computer," *Proceedings of the Royal Society of London. A. Mathematical and Physical Sciences*, vol. 400, no. 1818, pp. 97–117, 1985.

[8] P. W. Shor, "Polynomial-time algorithms for prime factorization and discrete logarithms on a quantum computer," *SIAM review*, vol. 41, no. 2, pp. 303–332, 1999.

[9] D. J. Moylett, N. Linden, and A. Montanaro, "Quantum speedup of the traveling-salesman problem for bounded-degree graphs," *Physical Review A*, vol. 95, no. 3, p. 032323, 2017.

[10] L. K. Grover, "A fast quantum mechanical algorithm for database search," in *Proceedings of the twenty-eighth annual ACM symposium on Theory of computing*, pp. 212–219, 1996.

[11] C. H. Bennett, G. Brassard, and A. K. Ekert, "Quantum cryptography," *Scientific American*, vol. 267, no. 4, pp. 50–57, 1992.

[12] F. Arute, K. Arya, R. Babbush, D. Bacon, J. C. Bardin, R. Barends, R. Biswas, S. Boixo, F. G. Brandao, D. A. Buell, *et al.*, "Quantum supremacy using a programmable superconducting processor," *Nature*, vol. 574, no. 7779, pp. 505–510, 2019.

[13] S. Slussarenko and G. J. Pryde, "Photonic quantum information processing: A concise review," *Applied Physics Reviews*, vol. 6, no. 4, 2019.

[14] K. R. Brown, J. Kim, and C. Monroe, "Co-designing a scalable quantum computer with trapped atomic ions," *npj Quantum Information*, vol. 2, no. 1, pp. 1–10, 2016.

[15] P. Neumann, R. Kolesov, B. Naydenov, J. Beck, F. Rempp, M. Steiner, V. Jacques, G. Balasubramanian, M. Markham, D. Twitchen, *et al.*, "Quantum register based on coupled electron spins in a room-temperature solid," *Nature Physics*, vol. 6, no. 4, pp. 249–253, 2010.

[16] F. A. Zwanenburg, A. S. Dzurak, A. Morello, M. Y. Simmons, L. C. Hollenberg, G. Klimeck, S. Rogge, S. N. Coppersmith, and M. A. Eriksson, "Silicon quantum electronics," *Reviews of modern physics*, vol. 85, no. 3, p. 961, 2013.

[17] D. P. DiVincenzo, "The physical implementation of quantum computation," *Fortschritte der Physik: Progress of Physics*, vol. 48, no. 9-11, pp. 771–783, 2000.

[18] G. Kurizki, P. Bertet, Y. Kubo, K. Mølmer, D. Petrosyan, P. Rabl, and J. Schmiedmayer, "Quantum technologies with hybrid systems," *Proceedings of the National Academy of Sciences of the United States of America*, vol. 112, no. 13, pp. 3866–3873, 2015.

[19] Z.-L. Xiang, S. Ashhab, J. You, and F. Nori, "Hybrid quantum circuits: Superconducting circuits interacting with other quantum systems," *Reviews of Modern Physics*, vol. 85, no. 2, p. 623, 2013.

[20] H. J. Kimble, "The quantum internet," *Nature*, vol. 453, no. 7198, pp. 1023–1030, 2008.

[21] D. Cuomo, M. Caleffi, and A. S. Cacciapuoti, "Towards a distributed quantum computing ecosystem," *arXiv preprint arXiv:2002.11808*, 2020.

[22] L.-M. Duan and C. Monroe, "Robust probabilistic quantum information processing with atoms, photons, and atomic ensembles," *Advances in Atomic, Molecular, and Optical Physics*, vol. 55, pp. 419–463, 2008.

[23] C. Monroe and J. Kim, "Scaling the ion trap quantum processor," *Science*, vol. 339, no. 6124, pp. 1164–1169, 2013.

[24] J. Wang, F. Sciarrino, A. Laing, and M. G. Thompson, "Integrated photonic quantum technologies," *Nature Photonics*, pp. 1–12, 2019.

[25] L. Li, T. Schröder, E. H. Chen, M. Walsh, I. Bayn, J. Goldstein, O. Gaathon, M. E. Trusheim, M. Lu, J. Mower, M. Cotlet, M. L. Markham, D. J. Twitchen, and D. Englund, "Coherent spin control of a nanocavity-enhanced qubit in diamond," *Nature Communications*, vol. 6, 2015.

[26] L. Stephenson, D. Nadlinger, B. Nichol, S. An, P. Drmota, T. Ballance, K. Thirumalai, J. Goodwin, D. Lucas, and C. Ballance, "High-rate, high-fidelity entanglement of qubits across an elementary quantum network," *Physical Review Letters*, vol. 124, no. 11, p. 110501, 2020.

[27] J. P. Dowling, J. Franson, H. Lee, and G. J. Milburn, "Towards scalable linear-optical quantum computers," in *Experimental Aspects of Quantum Computing*, pp. 205–213, Springer, 2005.

[28] A. I. Lvovsky, B. C. Sanders, and W. Tittel, "Optical quantum memory," *Nature Photonics*, vol. 3, no. 12, pp. 706–714, 2009.

[29] J. Nunn, N. K. Langford, W. S. Kolthammer, T. F. Champion, M. R. Sprague, P. S. Michelberger, X. M. Jin, D. G. England, and I. A. Walmsley, "Enhancing multiphoton rates with quantum memories," *Physical Review Letters*, vol. 110, no. 13, pp. 1–5, 2013.

[30] N. Sangouard, C. Simon, H. De Riedmatten, and N. Gisin, "Quantum repeaters based on atomic ensembles and linear optics," *Reviews of Modern Physics*, vol. 83, no. 1, pp. 33–80, 2011.

[31] A. Reiserer and G. Rempe, "Cavity-based quantum networks with single atoms and optical photons," *Reviews of Modern Physics*, vol. 87, no. 4, pp. 1379–1418, 2015.

[32] K. Heshami, D. G. England, P. C. Humphreys, P. J. Bustard, V. M. Acosta, J. Nunn, and B. J. Sussman, "Quantum memories: emerging applications and recent advances," *Journal of modern optics*, vol. 63, no. 20, pp. 2005–2028, 2016.

[33] M. K. Tey, Z. Chen, S. A. Aljunid, B. Chng, F. Huber, G. Maslennikov, and C. Kurtsiefer, "Strong interaction between light and a single trapped atom without the need for a cavity," *Nature Physics*, vol. 4, no. 12, pp. 924–927, 2008.

[34] S. Ritter, C. Nölleke, C. Hahn, A. Reiserer, A. Neuzner, M. Uphoff, M. Mücke, E. Figueroa, J. Bochmann, and G. Rempe, "An elementary quantum network of single atoms in optical cavities," *Nature*, vol. 484, no. 7393, pp. 195–200, 2012.

[35] E. Vetsch, D. Reitz, G. Sagué, R. Schmidt, S. T. Dawkins, and A. Rauschenbeutel, "Optical interface created by laser-cooled atoms trapped in the evanescent field surrounding an optical nanofiber," *Physical Review Letters*, vol. 104, no. 20, pp. 1–4, 2010.

[36] H. P. Specht, C. Nölleke, A. Reiserer, M. Uphoff, E. Figueroa, S. Ritter, and G. Rempe, "A single-atom quantum memory," *Nature*, vol. 473, no. 7346, pp. 190–193, 2011.

[37] K. Hammerer, A. S. Sørensen, and E. S. Polzik, "Quantum interface between light and atomic ensembles," *Reviews of Modern Physics*, vol. 82, no. 2, pp. 1041–1093, 2010.

[38] T. Chanelière, D. Matsukevich, S. Jenkins, S.-Y. Lan, T. Kennedy, and A. Kuzmich, "Storage and retrieval of single photons transmitted between remote quantum memories," *Nature*, vol. 438, no. 7069, pp. 833–836, 2005.

[39] A. W. Elshaari, W. Pernice, K. Srinivasan, O. Benson, and V. Zwiller, "Hybrid integrated quantum photonic circuits," *Nature Photonics*, vol. 14, no. 5, pp. 285–298, 2020.

[40] M. J. Burek, C. Meuwly, R. E. Evans, M. K. Bhaskar, A. Sipahigil, S. Meesala, B. MacHielse, D. D. Sukachev, C. T. Nguyen, J. L. Pacheco, E. Bielejec, M. D. Lukin, and M. Lončar, "Fiber-coupled diamond quantum nanophotonic interface," *Physical Review Applied*, vol. 8, no. 2, pp. 1–10, 2017.

[41] P. Lodahl, "Quantum-dot based photonic quantum networks," *Quantum Science and Technology*, vol. 3, no. 1, p. 013001, 2017.

[42] R. J. Mears, L. Reekie, I. Jauncey, and D. N. Payne, "Low-noise erbium-doped fibre amplifier operating at 1.54 μm," *Electronics Letters*, vol. 23, no. 19, pp. 1026–1028, 1987.

[43] A. Javadi, I. Söllner, M. Arcari, S. L. Hansen, L. Midolo, S. Mahmoodian, G. Kiršansk, T. Pregnolato, E. H. Lee, J. D. Song, S. Stobbe, and P. Lodahl, "Single-photon non-linear optics with a quantum dot in a waveguide," *Nature Communications*, vol. 6, pp. 6–10, 2015.

[44] A. Sipahigil, R. E. Evans, D. D. Sukachev, M. J. Burek, J. Borregaard, M. K. Bhaskar, C. T. Nguyen, J. L. Pacheco, H. A. Atikian, C. Meuwly, R. M. Camacho, F. Jelezko, E. Bielejec, H. Park, M. Lončar, and M. D. Lukin, "An integrated diamond nanophotonics platform for quantum-optical networks," *Science*, vol. 354, no. 6314, pp. 847–850, 2016.

[45] R. L. Ahlefeldt, M. J. Pearce, M. R. Hush, and M. J. Sellars, "Quantum processing with ensembles of rare-earth ions in a stoichiometric crystal," *Physical Review A*, vol. 101, no. 1, pp. 1–11, 2020.

[46] A. Seri, A. Lenhard, D. Rieländer, M. Gündoğan, P. M. Ledingham, M. Mazzera, and H. de Riedmatten, "Quantum correlations between single telecom photons and a multimode on-demand solid-state quantum memory," *Physical Review X*, vol. 7, no. 2, p. 021028, 2017.

[47] D. D. Sukachev, A. Sipahigil, C. T. Nguyen, M. K. Bhaskar, R. E. Evans, F. Jelezko, and M. D. Lukin, "Silicon-Vacancy Spin Qubit in Diamond: A Quantum Memory Exceeding 10 ms with Single-Shot State Readout," *Physical Review Letters*, vol. 119, no. 22, pp. 1–5, 2017.

[48] A. Myerson, D. Szwer, S. Webster, D. Allcock, M. Curtis, G. Imreh, J. Sherman, D. Stacey, A. Steane, and D. Lucas, "High-fidelity readout of trapped-ion qubits," *Physical Review Letters*, vol. 100, no. 20, p. 200502, 2008.

[49] W. Tittel, M. Afzelius, T. Chaneliere, R. L. Cone, S. Kröll, S. A. Moiseev, and M. Sellars, "Photon-echo quantum memory in solid state systems," *Laser & Photonics Reviews*, vol. 4, no. 2, pp. 244–267, 2010.

[50] I. Marcikic, H. De Riedmatten, W. Tittel, H. Zbinden, M. Legré, and N. Gisin, "Distribution of time-bin entangled qubits over 50 km of optical fiber," *Physical Review Letters*, vol. 93, no. 18, p. 180502, 2004.

[51] A. Crespi, R. Ramponi, R. Osellame, L. Sansoni, I. Bongioanni, F. Sciarrino, G. Vallone, and P. Mataloni, "Integrated photonic quantum gates for polarization qubits," *Nature communications*, vol. 2, no. 1, pp. 1–6, 2011.

[52] D. Giovannini, E. Nagali, L. Marrucci, and F. Sciarrino, "Resilience of orbital-angular-momentum photonic qubits and effects on hybrid entanglement," *Physical Review A*, vol. 83, no. 4, p. 042338, 2011.

[53] B. Brecht, A. Eckstein, R. Ricken, V. Quiring, H. Suche, L. Sansoni, and C. Silberhorn, "Demonstration of coherent time-frequency schmidt mode selection using dispersion-engineered frequency conversion," *Physical Review A*, vol. 90, no. 3, p. 030302, 2014.

[54] L. Olislager, J. Cussey, A. T. Nguyen, P. Emplit, S. Massar, J.-M. Merolla, and K. P. Huy, "Frequency-bin entangled photons," *Physical Review A*, vol. 82, no. 1, p. 013804, 2010.

[55] J. Yin, Y. Cao, Y.-H. Li, S.-K. Liao, L. Zhang, J.-G. Ren, W.-Q. Cai, W.-Y. Liu, B. Li, H. Dai, *et al.*, "Satellite-based entanglement distribution over 1200 kilometers," *Science*, vol. 356, no. 6343, pp. 1140–1144, 2017.

[56] S.-K. Liao, W.-Q. Cai, W.-Y. Liu, L. Zhang, Y. Li, J.-G. Ren, J. Yin, Q. Shen, Y. Cao, Z.-P. Li, *et al.*, "Satellite-to-ground quantum key distribution," *Nature*, vol. 549, no. 7670, pp. 43–47, 2017.

[57] T. Rudolph, "Why i am optimistic about the silicon-photonic route to quantum computing," *APL Photonics*, vol. 2, no. 3, p. 030901, 2017.

[58] P. Kok, W. J. Munro, K. Nemoto, T. C. Ralph, J. P. Dowling, and G. J. Milburn, "Linear optical quantum computing with photonic qubits," *Reviews of Modern Physics*, vol. 79, no. 1, p. 135, 2007.

[59] E. Knill, R. Laflamme, and G. J. Milburn, "A scheme for efficient quantum computation with linear optics," *nature*, vol. 409, no. 6816, pp. 46–52, 2001.

[60] T. Ralph, A. White, W. Munro, and G. Milburn, "Simple scheme for efficient linear optics quantum gates," *Physical Review A*, vol. 65, no. 1, p. 012314, 2001.

[61] J. L. O'Brien, G. J. Pryde, A. G. White, T. C. Ralph, and D. Branning, "Demonstration of an all-optical quantum controlled-not gate," *Nature*, vol. 426, no. 6964, pp. 264–267, 2003.

[62] T. Jennewein, M. Barbieri, and A. G. White, "Single-photon device requirements for operating linear optics quantum computing outside the post-selection basis," *Journal of Modern Optics*, vol. 58, no. 3-4, pp. 276–287, 2011.

[63] Y. Li, P. C. Humphreys, G. J. Mendoza, and S. C. Benjamin, "Resource costs for fault-tolerant linear optical quantum computing," *Physical Review X*, vol. 5, no. 4, p. 041007, 2015.

[64] X.-L. Wang, Y.-H. Luo, H.-L. Huang, M.-C. Chen, Z.-E. Su, C. Liu, C. Chen, W. Li, Y.-Q. Fang, X. Jiang, *et al.*, "18-qubit entanglement with six photons' three degrees of freedom," *Physical review letters*, vol. 120, no. 26, p. 260502, 2018.

[65] M. Bock, A. Lenhard, C. Chunnilall, and C. Becher, "Highly efficient heralded single-photon source for telecom wavelengths based on a ppln waveguide," *Optics express*, vol. 24, no. 21, pp. 23992–24001, 2016.

[66] S. Fasel, O. Alibart, S. Tanzilli, P. Baldi, A. Beveratos, N. Gisin, and H. Zbinden, "High-quality asynchronous heralded single-photon source at telecom wavelength," *New Journal of Physics*, vol. 6, pp. 1–11, 2004.

[67] M. M. Weston, H. M. Chrzanowski, S. Wollmann, A. Boston, J. Ho, L. K. Shalm, V. B. Verma, M. S. Allman, S. W. Nam, R. B. Patel, S. Slussarenko, and G. J. Pryde, "Efficient and pure femtosecond-pulse-length source of polarization-entangled photons," *Optics Express*, vol. 24, no. 10, p. 10869, 2016.

[68] S. Ramelow, A. Mech, M. Giustina, S. Gröblacher, W. Wieczorek, J. Beyer, A. Lita, B. Calkins, T. Gerrits, S. W. Nam, A. Zeilinger, and R. Ursin, "Highly efficient heralding of entangled single photons," *Optics Express*, vol. 21, no. 6, p. 6707, 2013.

[69] A. Christ and C. Silberhorn, "Limits on the deterministic creation of pure single-photon states using parametric down-conversion," *Physical Review A - Atomic, Molecular, and Optical Physics*, vol. 85, no. 2, pp. 1–6, 2012.

[70] P. S. Michelberger, T. F. Champion, M. R. Sprague, K. T. Kaczmarek, M. Barbieri, X. M. Jin, D. G. England, W. S. Kolthammer, D. J. Saunders, J. Nunn, and I. A. Walmsley, "Interfacing GHz-bandwidth heralded single photons with a warm vapour Raman memory," *New Journal of Physics*, vol. 17, 2015.

[71] R. Mottola, G. Buser, C. Müller, T. Kroh, A. Ahlrichs, S. Ramelow, O. Benson, P. Treutlein, and J. Wolters, "An efficient, tunable, and robust source of narrowband photon pairs at the 87 rb d1 line," *Optics Express*, vol. 28, no. 3, pp. 3159–3170, 2020.

[72] J. Fekete, D. Rieländer, M. Cristiani, and H. de Riedmatten, "Ultranarrow-band photon-pair source compatible with solid state quantum memories and telecommunication networks," *Physical review letters*, vol. 110, no. 22, p. 220502, 2013.

[73] M. Rambach, A. Nikolova, T. J. Weinhold, and A. G. White, "Sub-megahertz linewidth single photon source," *APL Photonics*, vol. 1, no. 9, p. 096101, 2016.

[74] L. Zhang, Y. J. Yu, L. G. Chen, Y. Luo, B. Yang, F. F. Kong, G. Chen, Y. Zhang, Q. Zhang, Y. Luo, J. L. Yang, Z. C. Dong, and J. G. Hou, "Electrically driven single-photon emission from an isolated single molecule," *Nature Communications*, vol. 8, no. 1, pp. 1–7, 2017.

[75] B. Rodiek, M. Lopez, H. Hofer, G. Porrovecchio, M. Smid, X.-L. Chu, S. Gotzinger, V. Sandoghdar, S. Lindner, C. Becher, and S. Kuck, "Experimental realization of an absolute single-photon source based on a single nitrogen vacancy center in a nanodiamond," *Optica*, vol. 4, no. 1, p. 71, 2017.

[76] P. B. Nisbet-Jones, J. Dilley, D. Ljunggren, and A. Kuhn, "Highly efficient source for indistinguishable single photons of controlled shape," *New Journal of Physics*, vol. 13, no. 10, p. 103036, 2011.

[77] P. Senellart, G. Solomon, and A. White, "High-performance semiconductor quantum-dot single-photon sources," *Nature Nanotechnology*, vol. 12, no. 11, pp. 1026–1039, 2017.

[78] N. Somaschi, V. Giesz, L. De Santis, J. C. Loredo, M. P. Almeida, G. Hornecker, S. L. Portalupi, T. Grange, C. Antón, J. Demory, C. Gómez, I. Sagnes, N. D. Lanzillotti-Kimura, A. Lemaítre, A. Auffeves, A. G. White, L. Lanco, and P. Senellart, "Near-optimal single-photon sources in the solid state," *Nature Photonics*, vol. 10, no. 5, pp. 340–345, 2016.

[79] J. Iles-Smith, D. P. McCutcheon, A. Nazir, and J. Mørk, "Phonon scattering inhibits simultaneous near-unity efficiency and indistinguishability in semiconductor single-photon sources," *Nature Photonics*, vol. 11, no. 8, pp. 521–526, 2017.

[80] N. Tomm, A. Javadi, N. O. Antoniadis, D. Najer, M. C. Löbl, A. R. Korsch, R. Schott, S. R. Valentin, A. D. Wieck, A. Ludwig, *et al.*, "A bright and fast source of coherent single photons," *arXiv preprint arXiv:2007.12654*, 2020.

[81] S. Thomas, M. Billard, N. Coste, S. Wein, H. Ollivier, O. Krebs, L. Tazaïrt, A. Harouri, A. Lemaitre, I. Sagnes, *et al.*, "Efficient source of indistinguishable single-photons based on phonon-assisted excitation," *arXiv preprint arXiv:2007.04330*, 2020.

[82] W. K. Wootters and W. H. Zurek, "A single quantum cannot be cloned," *Nature*, vol. 299, no. 5886, pp. 802–803, 1982.

[83] C. H. Bennett and G. Brassard, "Quantum cryptography: Public key distribution and coin tossing," *arXiv preprint arXiv:2003.06557*, 2020.

[84] B. Zhu, H. Zhang, P. Borel, T. Geisler, R. Jensen, M. Stegmaier, B. Palsdottir, D. Peckham, R. Lingle, D. Vaidya, *et al.*, "200km repeater length transmission of real-time processed 21.2 tb/s (106× 200gb/s) over 1200km fibre," in *45th European Conference on Optical Communication (ECOC 2019)*, pp. 1–3, IET, 2019.

[85] D. Dieks, "Physics letters," *Nature*, vol. 194, no. 4833, p. 1021, 1962.

[86] M. Zukowski, A. Zeilinger, M. A. Horne, and A. K. Ekert, ""Event-ready-detectors" Bell experiment via entanglement swapping," *Physical Review Letters*, vol. 71, no. 26, pp. 4287–4290, 1993.

[87] H. J. Briegel, W. Dür, J. I. Cirac, and P. Zoller, "Quantum repeaters: The role of imperfect local operations in quantum communication," *Physical Review Letters*, vol. 81, no. 26, pp. 5932–5935, 1998.

[88] H.-S. Zhong, Y. Li, W. Li, L.-C. Peng, Z.-E. Su, Y. Hu, Y.-M. He, X. Ding, W. Zhang, H. Li, *et al.*, "12-photon entanglement and scalable scattershot boson sampling with optimal entangled-photon pairs from parametric down-conversion," *Physical review letters*, vol. 121, no. 25, p. 250505, 2018.

[89] H. Wang, J. Qin, X. Ding, M.-C. Chen, S. Chen, X. You, Y.-M. He, X. Jiang, L. You, Z. Wang, *et al.*, "Boson sampling with 20 input photons and a 60-mode interferometer in a 1 0 14-dimensional hilbert space," *Physical review letters*, vol. 123, no. 25, p. 250503, 2019.

[90] S. Gao, O. Lazo-Arjona, B. Brecht, K. T. Kaczmarek, S. E. Thomas, J. Nunn, P. M. Ledingham, D. J. Saunders, and I. A. Walmsley, "Optimal Coherent Filtering for Single Noisy Photons," *Physical Review Letters*, vol. 123, no. 21, p. 213604, 2019.

[91] F. Bussières, N. Sangouard, M. Afzelius, H. De Riedmatten, C. Simon, and W. Tittel, "Prospective applications of optical quantum memories," *Journal of Modern Optics*, vol. 60, no. 18, pp. 1519–1537, 2013.

[92] R. Jozsa, "Fidelity for mixed quantum states," *Journal of Modern Optics*, vol. 41, no. 12, pp. 2315–2323, 1994.

[93] S. Massar and S. Popescu, "Optimal extraction of information from finite quantum ensembles," *Physical Review Letters*, vol. 74, no. 8, pp. 1259–1263, 1995.

[94] A. Grodecka-Grad, E. Zeuthen, and A. S. Sørensen, "High-capacity spatial multimode quantum memories based on atomic ensembles," *Physical Review Letters*, vol. 109, no. 13, 2012.

[95] N. Sinclair, E. Saglamyurek, H. Mallahzadeh, J. A. Slater, M. George, R. Ricken, M. P. Hedges, D. Oblak, C. Simon, W. Sohler, and W. Tittel, "Spectral multiplexing for scalable quantum photonics using an atomic frequency comb quantum memory and feed-forward control," *Physical Review Letters*, vol. 113, no. 5, pp. 1–5, 2014.

[96] M. Afzelius, C. Simon, H. De Riedmatten, and N. Gisin, "Multimode quantum memory based on atomic frequency combs," *Physical Review A - Atomic, Molecular, and Optical Physics*, vol. 79, no. 5, pp. 1–9, 2009.

[97] J. Nunn, I. A. Walmsley, M. G. Raymer, K. Surmacz, F. C. Waldermann, Z. Wang, and D. Jaksch, "Mapping broadband single-photon wave packets into an atomic memory," *Physical Review A - Atomic, Molecular, and Optical Physics*, vol. 75, no. 1, pp. 1–4, 2007.

[98] Z. Zheng, O. Mishina, N. Treps, and C. Fabre, "Atomic quantum memory for multimode frequency combs," *Physical Review A - Atomic, Molecular, and Optical Physics*, vol. 91, no. 3, pp. 1–5, 2015.

[99] N. Sangouard, C. Simon, M. Afzelius, and N. Gisin, "Analysis of a quantum memory for photons based on controlled reversible inhomogeneous broadening," *Physical Review A - Atomic, Molecular, and Optical Physics*, vol. 75, no. 3, pp. 1–8, 2007.

[100] S. Zaske, A. Lenhard, C. A. Keßler, J. Kettler, C. Hepp, C. Arend, R. Albrecht, W. M. Schulz, M. Jetter, P. Michler, and C. Becher, "Visible-to-telecom quantum frequency conversion of light from a single quantum emitter," *Physical Review Letters*, vol. 109, no. 14, pp. 1–5, 2012.

[101] T. A. Wright, R. J. Francis-Jones, C. B. Gawith, J. N. Becker, P. M. Ledingham, P. G. Smith, J. Nunn, P. J. Mosley, B. Brecht, and I. A. Walmsley, "Two-Way Photonic Interface for Linking the Sr+ Transition at 422 nm to the Telecommunication C Band," *Physical Review Applied*, vol. 10, no. 4, p. 1, 2018.

[102] C. Simon, M. Afzelius, J. Appel, A. B. de La Giroday, S. Dewhurst, N. Gisin, C. Hu, F. Jelezko, S. Kröll, J. Müller, *et al.*, "Quantum memories," *The European Physical Journal D*, vol. 58, no. 1, pp. 1–22, 2010.

[103] F. Kaneda, F. Xu, J. Chapman, and P. G. Kwiat, "Quantum-memory-assisted multi-photon generation for efficient quantum information processing," *Optica*, vol. 4, no. 9, p. 1034, 2017.

[104] Y. Wang, M. Um, J. Zhang, S. An, M. Lyu, J. N. Zhang, L. M. Duan, D. Yum, and K. Kim, "Single-qubit quantum memory exceeding ten-minute coherence time," *Nature Photonics*, vol. 11, no. 10, pp. 646–650, 2017.

[105] K. Tsurumoto, R. Kuroiwa, H. Kano, Y. Sekiguchi, and H. Kosaka, "Quantum teleportation-based state transfer of photon polarization into a carbon spin in diamond," *Communications Physics*, vol. 2, no. 1, pp. 1–6, 2019.

[106] K. T. Kaczmarek, P. M. Ledingham, B. Brecht, S. E. Thomas, G. S. Thekkadath, O. Lazo-Arjona, J. H. Munns, E. Poem, A. Feizpour, D. J. Saunders, J. Nunn, and I. A. Walmsley, "High-speed noise-free optical quantum memory," *Physical Review A*, vol. 97, no. 4, pp. 1–10, 2018.

[107] P. Vernaz-Gris, K. Huang, M. Cao, A. S. Sheremet, and J. Laurat, "Highly-efficient quantum memory for polarization qubits in a spatially-multiplexed cold atomic ensemble," *Nature Communications*, vol. 9, no. 1, pp. 1–6, 2018.

[108] M. P. Hedges, J. J. Longdell, Y. Li, and M. J. Sellars, "Efficient quantum memory for light," *Nature*, vol. 465, no. 7301, pp. 1052–1056, 2010.

[109] J. J. Longdell, E. Fraval, M. J. Sellars, and N. B. Manson, "Stopped light with storage times greater than one second using electromagnetically induced transparency in a solid," *Physical Review Letters*, vol. 95, no. 6, pp. 2–5, 2005.

[110] Y. Wang, J. Li, S. Zhang, K. Su, Y. Zhou, K. Liao, S. Du, H. Yan, and S. L. Zhu, "Efficient quantum memory for single-photon polarization qubits," *Nature Photonics*, vol. 13, no. 5, pp. 346–351, 2019.

[111] K.-J. Boller, A. Imamoğlu, and S. E. Harris, "Observation of electromagnetically induced transparency," *Physical Review Letters*, vol. 66, no. 20, p. 2593, 1991.

[112] A. V. Gorshkov, A. André, M. Fleischhauer, A. S. Sørensen, and M. D. Lukin, "Universal approach to optimal photon storage in atomic media," *Physical review letters*, vol. 98, no. 12, p. 123601, 2007.

[113] A. Kozhekin, K. Mølmer, and E. Polzik, "Quantum memory for light," *Physical Review A - Atomic, Molecular, and Optical Physics*, vol. 62, no. 3, pp. 1–5, 2000.

[114] M. Fleischhauer and M. D. Lukin, "Dark-state polaritons in electromagnetically induced transparency," *Physical Review Letters*, vol. 84, no. 22, pp. 5094–5097, 2000.

[115] D. F. Phillips, A. Fleischhauer, A. Mair, R. L. Walsworth, and M. D. Lukin, "Storage of light in atomic vapor," *Physical Review Letters*, vol. 86, no. 5, pp. 783–786, 2001.

[116] Chien˜Liu, Zachary˜Dutton, Cyrus˜H.˜Behroozi, and Lene˜Vestergaard˜Hau, "Observation of coherent optical information storage in an atomic medium using halted light pulses," *Nature*, vol. 409, no. 6819, pp. 490–493, 2001.

[117] A. V. Turukhin, V. S. Sudarshanam, M. S. Shahriar, J. A. Musser, B. S. Ham, and P. R. Hemmer, "Observation of ultraslow and stored light pulses in a solid," *Physical Review Letters*, vol. 88, no. 2, pp. 1–4, 2002.

[118] Y. O. Dudin, L. Li, and A. Kuzmich, "Light storage on the time scale of a minute," *Physical Review A - Atomic, Molecular, and Optical Physics*, vol. 87, no. 3, pp. 1–4, 2013.

[119] G. Heinze, C. Hubrich, and T. Halfmann, "Stopped light and image storage by electromagnetically induced transparency up to the regime of one minute," *Physical Review Letters*, vol. 111, no. 3, pp. 1–5, 2013.

[120] K. F. Reim, J. Nunn, V. O. Lorenz, B. J. Sussman, K. C. Lee, N. K. Langford, D. Jaksch, and I. A. Walmsley, "Towards high-speed optical quantum memories," *Nature Photonics*, vol. 4, no. 4, pp. 218–221, 2010.

[121] K. A. Fisher, D. G. England, J. P. W. MacLean, P. J. Bustard, K. J. Resch, and B. J. Sussman, "Frequency and bandwidth conversion of single photons in a room-temperature diamond quantum memory," *Nature Communications*, vol. 7, pp. 5–10, 2016.

[122] J. Guo, X. Feng, P. Yang, Z. Yu, L. Chen, C.-H. Yuan, and W. Zhang, "High-performance raman quantum memory with optimal control in room temperature atoms," *Nature communications*, vol. 10, no. 1, pp. 1–6, 2019.

[123] D. G. England, K. A. Fisher, J.-P. W. MacLean, P. J. Bustard, R. Lausten, K. J. Resch, and B. J. Sussman, "Storage and retrieval of thz-bandwidth single photons using a room-temperature diamond quantum memory," *Physical review letters*, vol. 114, no. 5, p. 053602, 2015.

[124] J. Nunn, J. H. Munns, S. Thomas, K. T. Kaczmarek, C. Qiu, A. Feizpour, E. Poem, B. Brecht, D. J. Saunders, P. M. Ledingham, D. V. Reddy, M. G. Raymer, and I. A. Walmsley, "Theory of noise suppression in Λ -type quantum memories by means of a cavity," *Physical Review A*, vol. 96, no. 1, pp. 1–12, 2017.

[125] S. E. Thomas, J. H. Munns, K. T. Kaczmarek, C. Qiu, B. Brecht, A. Feizpour, P. M. Ledingham, I. A. Walmsley, J. Nunn, and D. J. Saunders, "High efficiency Raman memory by suppressing radiation trapping," *New Journal of Physics*, vol. 19, no. 6, 2017.

[126] D. Saunders, J. Munns, T. Champion, C. Qiu, K. Kaczmarek, E. Poem, P. Ledingham, I. Walmsley, and J. Nunn, "Cavity-enhanced room-temperature broadband raman memory," *Physical Review Letters*, vol. 116, no. 9, p. 090501, 2016.

[127] S. E. Thomas, T. M. Hird, J. H. Munns, B. Brecht, D. J. Saunders, J. Nunn, I. A. Walmsley, and P. M. Ledingham, "Raman quantum memory with built-in suppression of four-wave-mixing noise," *Physical Review A*, vol. 100, no. 3, p. 033801, 2019.

[128] E. Poem, R. Finkelstein, O. Michel, O. Lahad, and O. Firstenberg, "Fast, noise-free memory for photon synchronization at room temperature," *Asia Communications and Photonics Conference, ACP*, vol. 2018-October, pp. 1–7, 2018.

[129] S. A. Moiseev and S. Kröll, "Complete reconstruction of the quantum state of a single-photon wave packet absorbed by a doppler-broadened transition," *Physical Review Letters*, vol. 87, no. 17, pp. 17–20, 2001.

[130] E. L. Hahn, "Spin echoes," *Physical Review*, vol. 80, no. 4, pp. 580–594, 1950.

[131] I. D. Abella, N. A. Kurnit, and S. R. Hartmann, "Photon echoes," *Physical Review*, vol. 141, no. 1, pp. 391–406, 1966.

[132] J. Ruggiero, J. L. Le Gouët, C. Simon, and T. Chanelière, "Why the two-pulse photon echo is not a good quantum memory protocol," *Physical Review A - Atomic, Molecular, and Optical Physics*, vol. 79, no. 5, pp. 1–8, 2009.

[133] N. Sangouard, C. Simon, J. Minář, M. Afzelius, T. Chaneliere, N. Gisin, J.-L. Le Gouët, H. de Riedmatten, and W. Tittel, "Impossibility of faithfully storing single photons with the three-pulse photon echo," *Physical Review A*, vol. 81, no. 6, p. 062333, 2010.

[134] V. Damon, M. Bonarota, A. Louchet-Chauvet, T. Chaneliere, and J.-L. Le Gouët, "Revival of silenced echo and quantum memory for light," *New Journal of Physics*, vol. 13, no. 9, p. 093031, 2011.

[135] M. Nilsson, L. Rippe, S. Kröll, R. Klieber, and D. Suter, "Hole-burning techniques for isolation and study of individual hyperfine transitions in inhomogeneously broadened solids demonstrated in Pr 3+:Y2SiO5," *Physical Review B - Condensed Matter and Materials Physics*, vol. 70, no. 21, pp. 1–11, 2004.

[136] A. L. Alexander, J. J. Longdell, M. J. Sellars, and N. B. Manson, "Photon echoes produced by switching electric fields," *Physical Review Letters*, vol. 96, no. 4, pp. 1–4, 2006.

[137] G. Hétet, J. J. Longdell, A. L. Alexander, P. K. Lam, and M. J. Sellars, "Electro-optic quantum memory for light using two-level atoms," *Physical Review Letters*, vol. 100, no. 2, pp. 1–4, 2008.

[138] M. Hosseini, B. M. Sparkes, G. Campbell, P. K. Lam, and B. C. Buchler, "High efficiency coherent optical memory with warm rubidium vapour," *Nature Communications*, vol. 2, no. 1, 2011.

[139] M. Afzelius, I. Usmani, A. Amari, B. Lauritzen, A. Walther, C. Simon, N. Sangouard, J. Minář, H. De Riedmatten, N. Gisin, and S. Kröll, "Demonstration of atomic frequency comb memory for light with spin-wave storage," *Physical Review Letters*, vol. 104, no. 4, pp. 1–4, 2010.

[140] M. Bonarota, J. Ruggiero, J. L. Gouët, and T. Chanelière, "Efficiency optimization for atomic frequency comb storage," *Physical Review A - Atomic, Molecular, and Optical Physics*, vol. 81, no. 3, pp. 1–10, 2010.

[141] R. H. Dicke, "Coherence in spontaneous radiation processes," *Physical review*, vol. 93, no. 1, p. 99, 1954.

[142] M. Bonarota, J. Le Gouët, and T. Chaneliere, "Highly multimode storage in a crystal," *New Journal of Physics*, vol. 13, no. 1, p. 013013, 2011.

[143] I. Usmani, M. Afzelius, H. De Riedmatten, and N. Gisin, "Mapping multiple photonic qubits into and out of one solid-state atomic ensemble," *Nature Communications*, vol. 1, no. 1, pp. 1–7, 2010.

[144] D. Rieländer, K. Kutluer, P. M. Ledingham, M. Gündoğan, J. Fekete, M. Mazzera, and H. De Riedmatten, "Quantum storage of heralded single photons in a praseodymium-doped crystal," *Physical Review Letters*, vol. 112, no. 4, pp. 1–5, 2014.

[145] M. Gündoğan, P. M. Ledingham, K. Kutluer, M. Mazzera, and H. De Riedmatten, "Solid state spin-wave quantum memory for time-bin qubits," *Physical review letters*, vol. 114, no. 23, p. 230501, 2015.

[146] P. Jobez, C. Laplane, N. Timoney, N. Gisin, A. Ferrier, P. Goldner, and M. Afzelius, "Coherent spin control at the quantum level in an ensemble-based optical memory," *Physical review letters*, vol. 114, no. 23, p. 230502, 2015.

[147] S. P. Horvath, M. K. Alqedra, A. Kinos, A. Walther, S. Kröll, and L. Rippe, "Noise free on-demand atomic-frequency comb quantum memory," *arXiv preprint arXiv:2006.00943*, 2020.

[148] C. Huang, *Rare Earth Coordination Chemistry: Fundamentals and Applications*. 2010.

[149] G. Liu and B. Jacquier, *Spectroscopic properties of rare earths ions in optical materials*, vol. 53. 1970.

[150] G. H. Dieke and R. A. Satten, "Spectra and Energy Levels of Rare Earth Ions in Crystals," *American Journal of Physics*, 1970.

[151] M. Lovrić, P. Glasenapp, and D. Suter, "Spin Hamiltonian characterization and refinement for Pr3 +:YAlO 3 and Pr3 +:Y 2SiO 5," *Physical Review B - Condensed Matter and Materials Physics*, vol. 85, no. 1, pp. 1–8, 2012.

[152] S. Altner, G. Zumofen, U. Wild, and M. Mitsunaga, "Photon-echo attenuation in rare-earth-ion-doped crystals," *Physical Review B - Condensed Matter and Materials Physics*, vol. 54, no. 24, pp. 17493–17507, 1996.

[153] Jin Huang, J. M. Zhang, A. Lezama and T. W. Mossberg, "Excess Dephasing in Photon-Echo Experiments Arising from Excitation-Induced Electronic Level Shifts," vol. 63, no. 1, pp. 2–5, 1989.

[154] D. L. McAuslan, J. G. Bartholomew, M. J. Sellars, and J. J. Longdell, "Reducing decoherence in optical and spin transitions in rare-earth-metal-ion-doped materials," *Physical Review A - Atomic, Molecular, and Optical Physics*, vol. 85, no. 3, pp. 1–9, 2012.

[155] E. Fraval, M. J. Sellars, and J. J. Longdell, "Method of Extending Hyperfine Coherence Times in [Formula presented]," *Physical Review Letters*, vol. 92, no. 7, pp. 5–8, 2004.

[156] R. W. Equall, Y. Sun, R. L. Cone, and R. M. Macfarlane, "Ultraslow optical dephasing in Eu3+:Y2Si05," *Physical Review Letters*, vol. 72, no. 14, pp. 2179–2182, 1994.

[157] D. Serrano, C. Deshmukh, S. Liu, A. Tallaire, A. Ferrier, H. de Riedmatten, and P. Goldner, "Coherent optical and spin spectroscopy of nanoscale pr 3+: Y 2 o 3," *Physical Review B*, vol. 100, no. 14, p. 144304, 2019.

[158] D. A. Steck, "Rubidium 87 d line data," 2001.

[159] R. W. Equall, R. L. Cone, and R. M. MacFarlane, "Homogeneous broadening and hyperfine structure of optical transitions in Pr3+:Y2SiO5," *Physical Review B*, vol. 52, no. 6, pp. 3963–3969, 1995.

[160] C. Li, C. Wyon, and R. Moncorge, "Spectroscopic properties and fluorescence dynamics of er/sup 3+/and yb/sup 3+/in y/sub 2/sio/sub 5," *IEEE journal of quantum electronics*, vol. 28, no. 4, pp. 1209–1221, 1992.

[161] K. Holliday, M. Croci, E. Vauthey, and U. P. Wild, "Spectral hole burning and holography in an Y2SiO5:Pr 3+ crystal," *Physical Review B*, vol. 47, no. 22, pp. 14741–14752, 1993.

[162] B. Ham, M. Shahriar, and M. Kim, "Spin coherence excitation and rephasing with optically shelved atoms," *Physical Review B - Condensed Matter and Materials Physics*, vol. 58, no. 18, pp. R11825–R11828, 1998.

[163] A. Amari, A. Walther, M. Sabooni, M. Huang, S. Kröll, M. Afzelius, I. Usmani, B. Lauritzen, N. Sangouard, H. De Riedmatten, *et al.*, "Towards an efficient atomic frequency comb quantum memory," *Journal of Luminescence*, vol. 130, no. 9, pp. 1579–1585, 2010.

[164] M. Gündoğan, P. M. Ledingham, A. Almasi, M. Cristiani, and H. De Riedmatten, "Quantum storage of a photonic polarization qubit in a solid," *Physical Review Letters*, vol. 108, no. 19, pp. 2–7, 2012.

[165] T. Utikal, E. Eichhammer, L. Petersen, A. Renn, S. Götzinger, and V. Sandoghdar, "Spectroscopic detection and state preparation of a single praseodymium ion in a crystal," *Nature Communications*, vol. 5, 2014.

[166] D. J. Jones, S. A. Diddams, J. K. Ranka, A. Stentz, R. S. Windeler, J. L. Hall, and S. T. Cundiff, "Carrier-envelope phase control of femtosecond mode-locked lasers and direct optical frequency synthesis," *Science*, vol. 288, no. 5466, pp. 635–639, 2000.

[167] R. L. Ahlefeldt, A. Smith, and M. J. Sellars, "Ligand isotope structure of the optical 7F0 → 5D50 transition in EuCl3 · 6H 2O," *Physical Review B - Condensed Matter and Materials Physics*, vol. 80, no. 20, pp. 5–9, 2009.

[168] A. Seri, D. Lago-Rivera, A. Lenhard, G. Corrielli, R. Osellame, M. Mazzera, and H. de Riedmatten, "Quantum storage of frequency-multiplexed heralded single photons," *Physical review letters*, vol. 123, no. 8, p. 080502, 2019.

[169] M. F. Askarani, M. L. G. Puigibert, T. Lutz, V. B. Verma, M. D. Shaw, S. W. Nam, N. Sinclair, D. Oblak, and W. Tittel, "Storage and Reemission of Heralded Telecommunication-Wavelength Photons Using a Crystal Waveguide," *Physical Review Applied*, vol. 11, no. 5, p. 1, 2019.

[170] A. Ortu, A. Tiranov, S. Welinski, F. Fröwis, N. Gisin, A. Ferrier, P. Goldner, and M. Afzelius, "Simultaneous coherence enhancement of optical and microwave transitions in solid-state electronic spins," *Nature materials*, vol. 17, no. 8, pp. 671–675, 2018.

[171] E. Saglamyurek, N. Sinclair, J. Jin, J. A. Slater, D. Oblak, F. Bussieres, M. George, R. Ricken, W. Sohler, and W. Tittel, "Broadband waveguide quantum memory for entangled photons," *Nature*, vol. 469, no. 7331, pp. 512–515, 2011.

[172] P. Jobez, N. Timoney, C. Laplane, J. Etesse, A. Ferrier, P. Goldner, N. Gisin, and M. Afzelius, "Towards highly multimode optical quantum memory for quantum repeaters," *Physical Review A*, vol. 93, no. 3, p. 032327, 2016.

[173] M. W. Doherty, N. B. Manson, P. Delaney, F. Jelezko, J. Wrachtrup, and L. C. Hollenberg, "The nitrogen-vacancy colour centre in diamond," *Physics Reports*, vol. 528, no. 1, pp. 1–45, 2013.

[174] S. Kaboli and P. C. Burnley, "Direct observations of crystal defects in polycrystalline diamond," *Materials Characterization*, vol. 142, no. May, pp. 154–161, 2018.

[175] J. Walker, "Optical absorption and luminescence in diamond," *Reports on Progress in Physics*, vol. 42, no. 10, pp. 1605–1659, 1979.

[176] F. Jelezko and J. Wrachtrup, "Single defect centres in diamond: A review," *Physica Status Solidi (A) Applications and Materials Science*, vol. 203, no. 13, pp. 3207–3225, 2006.

[177] A. Zaitsev, "Vibronic spectra of impurity-related optical centers in diamond," *Physical Review B - Condensed Matter and Materials Physics*, vol. 61, no. 19, pp. 12909–12922, 2000.

[178] W. Saslow, T. K. Bergstresser, and M. L. Cohen, "Band structure and optical properties of diamond," *Physical Review Letters*, vol. 16, no. 9, pp. 354–356, 1966.

[179] M. W. Doherty, N. B. Manson, P. Delaney, and L. C. Hollenberg, "The negatively charged nitrogen-vacancy centre in diamond: The electronic solution," *New Journal of Physics*, vol. 13, 2011.

[180] M. V. Hauf, B. Grotz, B. Naydenov, M. Dankerl, S. Pezzagna, J. Meijer, F. Jelezko, J. Wrachtrup, M. Stutzmann, F. Reinhard, and J. A. Garrido, "Chemical control of the charge state of nitrogen-vacancy centers in diamond," *Physical Review B - Condensed Matter and Materials Physics*, vol. 83, no. 8, pp. 1–4, 2011.

[181] M. Pfender, N. Aslam, P. Simon, D. Antonov, G. Thiering, S. Burk, F. Fávaro de Oliveira, A. Denisenko, H. Fedder, J. Meijer, *et al.*, "Protecting a diamond quantum memory by charge state control," *Nano letters*, vol. 17, no. 10, pp. 5931–5937, 2017.

[182] C. Schreyvogel, V. Polyakov, R. Wunderlich, J. Meijer, and C. Nebel, "Active charge state control of single nv centres in diamond by in-plane al-schottky junctions," *Scientific reports*, vol. 5, no. 1, pp. 1–12, 2015.

[183] A. Gali, "Theory of the neutral nitrogen-vacancy center in diamond and its application to the realization of a qubit," *Physical Review B - Condensed Matter and Materials Physics*, vol. 79, no. 23, pp. 1–6, 2009.

[184] J. N. Becker, "Silicon Vacancy Colour Centres in Diamond: Coherence Properties & Quantum Control," 2017.

[185] M. K. Bhaskar, D. D. Sukachev, A. Sipahigil, R. E. Evans, M. J. Burek, C. T. Nguyen, L. J. Rogers, P. Siyushev, M. H. Metsch, H. Park, F. Jelezko, M. Lončar, and M. D. Lukin, "Quantum Nonlinear Optics with a Germanium-Vacancy Color Center in a Nanoscale Diamond Waveguide," *Physical Review Letters*, vol. 118, no. 22, pp. 1–6, 2017.

[186] J. M. Taylor, P. Cappellaro, L. Childress, L. Jiang, D. Budker, P. R. Hemmer, A. Yacoby, R. Walsworth, and M. D. Lukin, "High-sensitivity diamond magnetometer with nanoscale resolution," *Nature Physics*, vol. 4, no. 10, pp. 810–816, 2008.

[187] P. C. Humphreys, N. Kalb, P. Jaco, J. Morits, R. N. Schouten, R. F. L. Vermeulen, D. J. Twitchen, M. Markham, and R. Hanson, "quantum network," 2018.

[188] C. E. Bradley, J. Randall, M. H. Abobeih, R. C. Berrevoets, M. J. Degen, M. A. Bakker, M. Markham, D. J. Twitchen, and T. H. Taminiau, "A Ten-Qubit Solid-State Spin Register with Quantum Memory up to One Minute," *Physical Review X*, vol. 9, no. 3, p. 31045, 2019.

[189] J. R. Maze, A. Gali, E. Togan, Y. Chu, A. Trifonov, E. Kaxiras, and M. D. Lukin, "Properties of nitrogen-vacancy centers in diamond: The group theoretic approach," *New Journal of Physics*, vol. 13, 2011.

[190] J. H. Loubser and J. A. Van Wyk, "Electron spin resonance in the study of diamond," *Reports on Progress in Physics*, vol. 41, no. 8, pp. 1201–1248, 1978.

[191] A. Lenef and S. Rand, "Electronic structure of the N-V center in diamond: Theory," *Physical Review B - Condensed Matter and Materials Physics*, vol. 53, no. 20, pp. 13441–13455, 1996.

[192] N. Manson, J. Harrison, and M. Sellars, "Nitrogen-vacancy center in diamond: Model of the electronic structure and associated dynamics," *Physical Review B*, vol. 74, no. 10, p. 104303, 2006.

[193] A. Batalov, V. Jacques, F. Kaiser, P. Siyushev, P. Neumann, L. J. Rogers, R. L. McMurtrie, N. B. Manson, F. Jelezko, and J. Wrachtrup, "Low Temperature Studies of the Excited-State Structure of Negatively Charged Nitrogen-Vacancy Color Centers in Diamond," *Physical Review Letters*, vol. 102, no. 19, pp. 1–4, 2009.

[194] G. D. Fuchs, V. V. Dobrovitski, R. Hanson, A. Batra, C. D. Weis, T. Schenkel, and D. D. Awschalom, "Excited-state spectroscopy using single Spin manipulation in diamond," *Physical Review Letters*, vol. 101, no. 11, pp. 19–22, 2008.

[195] L. Robledo, H. Bernien, T. V. D. Sar, and R. Hanson, "Spin dynamics in the optical cycle of single nitrogen-vacancy centres in diamond," *New Journal of Physics*, vol. 13, 2011.

[196] L. Rondin, J. P. Tetienne, T. Hingant, J. F. Roch, P. Maletinsky, and V. Jacques, "Magnetometry with nitrogen-vacancy defects in diamond," *Reports on Progress in Physics*, vol. 77, no. 5, 2014.

[197] G. Kucsko, P. C. Maurer, N. Y. Yao, M. Kubo, H. J. Noh, P. K. Lo, H. Park, and M. D. Lukin, "Nanometre-scale thermometry in a living cell," *Nature*, vol. 500, no. 7460, pp. 54–58, 2013.

[198] M. W. Doherty, F. Dolde, H. Fedder, F. Jelezko, J. Wrachtrup, N. B. Manson, and L. C. Hollenberg, "Theory of the ground-state spin of the NV - center in diamond," *Physical Review B - Condensed Matter and Materials Physics*, vol. 85, no. 20, pp. 1–21, 2012.

[199] A. M. Stoneham, *Theory of defects in solids: electronic structure of defects in insulators and semiconductors*. Oxford University Press, 2001.

[200] H. A. Jahn and E. Teller, "Stability of polyatomic molecules in degenerate electronic states-i—orbital degeneracy," *Proceedings of the Royal Society of London. Series A-Mathematical and Physical Sciences*, vol. 161, no. 905, pp. 220–235, 1937.

[201] K. M. C. Fu, C. Santori, P. E. Barclay, L. J. Rogers, N. B. Manson, and R. G. Beausoleil, "Observation of the dynamic Jahn-Teller effect in the excited states of nitrogen-vacancy centers in diamond," *Physical Review Letters*, vol. 103, no. 25, pp. 1–4, 2009.

[202] L. J. Rogers, R. L. McMurtrie, M. J. Sellars, and N. B. Manson, "Time-averaging within the excited state of the nitrogen-vacancy centre in diamond," *New Journal of Physics*, vol. 11, 2009.

[203] J. Wolters, N. Sadzak, A. W. Schell, T. Schröder, and O. Benson, "Measurement of the ultrafast spectral diffusion of the optical transition of nitrogen vacancy centers in nano-size diamond using correlation interferometry," *Physical Review Letters*, vol. 110, no. 2, pp. 1–5, 2013.

[204] J. F. Barry, J. M. Schloss, E. Bauch, M. J. Turner, C. A. Hart, L. M. Pham, and R. L. Walsworth, "Sensitivity optimization for NV-diamond magnetometry," *Reviews of Modern Physics*, vol. 92, no. 1, 2020.

[205] E. Bauch, S. Singh, J. Lee, C. A. Hart, J. M. Schloss, M. J. Turner, J. F. Barry, L. Pham, N. Bar-Gill, S. F. Yelin, and R. L. Walsworth, "Decoherence of dipolar spin ensembles in diamond," pp. 1–12, 2019.

[206] J. Franck and E. Dymond, "Elementary processes of photochemical reactions," *Transactions of the Faraday Society*, vol. 21, no. February, pp. 536–542, 1926.

[207] E. Condon, "A theory of intensity distribution in band systems," *Physical Review*, vol. 28, no. 6, p. 1182, 1926.

[208] A. Gali, T. Simon, and J. Lowther, "An ab initio study of local vibration modes of the nitrogen-vacancy center in diamond," *New Journal of Physics*, vol. 13, no. 2, p. 025016, 2011.

[209] H.-Q. Zhao, M. Fujiwara, and S. Takeuchi, "Suppression of fluorescence phonon sideband from nitrogen vacancy centers in diamond nanocrystals by substrate effect," *Optics Express*, vol. 20, no. 14, p. 15628, 2012.

[210] I. Aharonovich, S. Castelletto, D. A. Simpson, C. H. Su, A. D. Greentree, and S. Prawer, "Diamond-based single-photon emitters," *Reports on Progress in Physics*, vol. 74, no. 7, 2011.

[211] S. Johnson, P. Dolan, T. Grange, A. Trichet, G. Hornecker, Y.-C. Chen, L. Weng, G. Hughes, A. Watt, A. Auffèves, *et al.*, "Tunable cavity coupling of the zero phonon line of a nitrogen-vacancy defect in diamond," *New Journal of Physics*, vol. 17, no. 12, p. 122003, 2015.

[212] Y. Chu and M. D. Lukin, "Quantum optics with nitrogen-vacancy centers in diamond," 2015.

[213] R. Albrecht, A. Bommer, C. Deutsch, J. Reichel, and C. Becher, "Supplemental Material : Coupling of a single NV center in diamond to a fiber-based microcavity," *Physical Review Letters*, vol. 83, no. 425, pp. 1–12, 2013.

[214] N. Mizuochi, T. Makino, H. Kato, D. Takeuchi, M. Ogura, H. Okushi, M. Nothaft, P. Neumann, A. Gali, F. Jelezko, J. Wrachtrup, and S. Yamasaki, "Electrically driven single-photon source at room temperature in diamond," *Nature Photonics*, vol. 6, no. 5, pp. 299–303, 2012.

[215] Y. Shen, T. M. Sweeney, and H. Wang, "Zero-phonon linewidth of single nitrogen vacancy centers in diamond nanocrystals," *Physical Review B*, vol. 77, no. 3, p. 033201, 2008.

[216] M. L. Goldman, M. W. Doherty, A. Sipahigil, N. Y. Yao, S. D. Bennett, N. B. Manson, A. Kubanek, and M. D. Lukin, "State-selective intersystem crossing in nitrogen-vacancy centers," *Physical Review B - Condensed Matter and Materials Physics*, vol. 91, no. 16, pp. 1–12, 2015.

[217] J. P. Tetienne, L. Rondin, P. Spinicelli, M. Chipaux, T. Debuisschert, J. F. Roch, and V. Jacques, "Magnetic-field-dependent photodynamics of single NV defects in diamond: An application to qualitative all-optical magnetic imaging," *New Journal of Physics*, vol. 14, 2012.

[218] L. Childress, M. G. Dutt, J. Taylor, A. Zibrov, F. Jelezko, J. Wrachtrup, P. Hemmer, and M. Lukin, "Coherent dynamics of coupled electron and nuclear spin qubits in diamond," *Science*, vol. 314, no. 5797, pp. 281–285, 2006.

[219] T. A. Kennedy, J. S. Colton, J. E. Butler, R. C. Linares, and P. J. Doering, "Long coherence times at 300 K for nitrogen-vacancy center spins in diamond grown by chemical vapor deposition," *Applied Physics Letters*, vol. 83, no. 20, pp. 4190–4192, 2003.

[220] F. Jelezko, T. Gaebel, I. Popa, M. Domhan, A. Gruber, and J. Wrachtrup, "Observation of coherent oscillation of a single nuclear spin and realization of a two-qubit conditional quantum gate," *Physical Review Letters*, vol. 93, no. 13, pp. 1–4, 2004.

[221] G. Balasubramanian, P. Neumann, D. Twitchen, M. Markham, R. Kolesov, N. Mizuochi, J. Isoya, J. Achard, J. Beck, J. Tissler, V. Jacques, P. R. Hemmer, F. Jelezko, and J. Wrachtrup, "Ultralong spin coherence time in isotopically engineered diamond," *Nature Materials*, vol. 8, no. 5, pp. 383–387, 2009.

[222] D. A. Hopper, H. J. Shulevitz, and L. C. Bassett, "Spin readout techniques of the nitrogen-vacancy center in diamond," *Micromachines*, vol. 9, no. 9, pp. 1–30, 2018.

[223] B. J. Shields, Q. P. Unterreithmeier, N. P. De Leon, H. Park, and M. D. Lukin, "Efficient Readout of a Single Spin State in Diamond via Spin-to-Charge Conversion," *Physical Review Letters*, vol. 114, no. 13, pp. 1–5, 2015.

[224] N. Aslam, G. Waldherr, P. Neumann, F. Jelezko, and J. Wrachtrup, "Photo-induced ionization dynamics of the nitrogen vacancy defect in diamond investigated by single-shot charge state detection," *New Journal of Physics*, vol. 15, 2013.

[225] G. Balasubramanian, I. Y. Chan, R. Kolesov, M. Al-Hmoud, J. Tisler, C. Shin, C. Kim, A. Wojcik, P. R. Hemmer, A. Krueger, T. Hanke, A. Leitenstorfer, R. Bratschitsch, F. Jelezko, and J. Wrachtrup, "Nanoscale imaging magnetometry with diamond spins under ambient conditions," *Nature*, vol. 455, no. 7213, pp. 648–651, 2008.

[226] E. Togan, Y. Chu, A. S. Trifonov, L. Jiang, J. Maze, L. Childress, M. V. Dutt, A. S. Sørensen, P. R. Hemmer, A. S. Zibrov, and M. D. Lukin, "Quantum entanglement between an optical photon and a solid-state spin qubit," *Nature*, vol. 466, no. 7307, pp. 730–734, 2010.

[227] K. Y. Han, S. K. Kim, C. Eggeling, and S. W. Hell, "Metastable dark states enable ground state depletion microscopy of nitrogen vacancy centers in diamond with diffraction-unlimited resolution," *Nano Letters*, vol. 10, no. 8, pp. 3199–3203, 2010.

[228] R. Schirhagl, K. Chang, M. Loretz, and C. L. Degen, "Nitrogen-Vacancy Centers in Diamond: Nanoscale Sensors for Physics and Biology," *Annual Review of Physical Chemistry*, vol. 65, no. 1, pp. 83–105, 2014.

[229] J. Klatzow, J. N. Becker, P. M. Ledingham, C. Weinzetl, K. T. Kaczmarek, D. J. Saunders, J. Nunn, I. A. Walmsley, R. Uzdin, and E. Poem, "Experimental demonstration of quantum effects in the operation of microscopic heat engines," *Physical Review Letters*, vol. 122, no. 11, p. 110601, 2019.

[230] D. Redman, S. Brown, and S. C. Rand, "Origin of persistent hole burning of N–V centers in diamond," *Journal of the Optical Society of America B*, vol. 9, no. 5, p. 768, 1992.

[231] G. Waldherr, J. Beck, M. Steiner, P. Neumann, A. Gali, T. H. Frauenheim, F. Jelezko, and J. Wrachtrup, "Dark states of single nitrogen-vacancy centers in diamond unraveled by single shot NMR," *Physical Review Letters*, vol. 106, no. 15, pp. 1–4, 2011.

[232] K. Heshami, C. Santori, B. Khanaliloo, C. Healey, V. M. Acosta, P. E. Barclay, and C. Simon, "Raman quantum memory based on an ensemble of nitrogen-vacancy centers coupled to a microcavity," *Physical Review A*, vol. 89, no. 4, p. 040301, 2014.

[233] B. Darquié, M. P. Jones, J. Dingjan, J. Beugnon, S. Bergamini, Y. Sortais, G. Messin, A. Browaeys, and P. Grangier, "Applied Physics: Controlled single-photon emission from a single trapped two-level atom," *Science*, vol. 309, no. 5733, pp. 454–456, 2005.

[234] G. Hétet, L. Slodička, M. Hennrich, and R. Blatt, "Single atom as a mirror of an optical cavity," *Physical Review Letters*, vol. 107, no. 13, pp. 1–5, 2011.

[235] H. Walther, B. T. Varcoe, B. G. Englert, and T. Becker, "Cavity quantum electrodynamics," *Reports on Progress in Physics*, vol. 69, no. 5, pp. 1325–1382, 2006.

[236] C. J. Hood, H. Kimble, and J. Ye, "Characterization of high-finesse mirrors: Loss, phase shifts, and mode structure in an optical cavity," *Physical Review A*, vol. 64, no. 3, p. 033804, 2001.

[237] T. Jung, J. Görlitz, B. Kambs, C. Pauly, N. Raatz, R. Nelz, E. Neu, A. M. Edmonds, M. Markham, F. Mücklich, J. Meijer, and C. Becher, "Spin measurements of NV centers coupled to a photonic crystal cavity," *APL Photonics*, vol. 4, no. 12, pp. 1–13, 2019.

[238] C. Weinzetl, J. Görlitz, J. N. Becker, I. A. Walmsley, E. Poem, J. Nunn, and C. Becher, "Coherent Control and Wave Mixing in an Ensemble of Silicon-Vacancy Centers in Diamond," *Physical Review Letters*, vol. 122, no. 6, p. 63601, 2019.

[239] Y. A. Kelaita, K. A. Fischer, T. M. Babinec, K. G. Lagoudakis, T. Sarmiento, A. Rundquist, A. Majumdar, and J. Vučković, "Hybrid metal-dielectric nanocavity for enhanced light-matter interactions," *Optical Materials Express*, vol. 7, no. 1, p. 231, 2017.

[240] N. V. Proscia, H. Jayakumar, X. Ge, G. Lopez-Morales, Z. Shotan, W. Zhou, C. A. Meriles, and V. M. Menon, "Scalable microcavity-coupled emitters in hexagonal boron nitride," 2019.

[241] C. T. Nguyen, D. D. Sukachev, M. K. Bhaskar, B. MacHielse, D. S. Levonian, E. N. Knall, P. Stroganov, C. Chia, M. J. Burek, R. Riedinger, H. Park, M. Lončar, and M. D. Lukin, "An integrated nanophotonic quantum register based on silicon-vacancy spins in diamond," *Physical Review B*, vol. 100, no. 16, pp. 1–19, 2019.

[242] G. Calajó, F. Ciccarello, D. Chang, and P. Rabl, "Atom-field dressed states in slow-light waveguide QED," *Physical Review A*, vol. 93, no. 3, pp. 1–18, 2016.

[243] M. Bajcsy, S. Hofferberth, V. Balic, T. Peyronel, M. Hafezi, A. S. Zibrov, V. Vuletic, and M. D. Lukin, "Efficient all-optical switching using slow light within a hollow fiber," *Physical Review Letters*, vol. 102, no. 20, pp. 1–4, 2009.

[244] A. Goban, C. L. Hung, J. D. Hood, S. P. Yu, J. A. Muniz, O. Painter, and H. J. Kimble, "Superradiance for Atoms Trapped along a Photonic Crystal Waveguide," *Physical Review Letters*, vol. 115, no. 6, pp. 1–5, 2015.

[245] A. Asenjo-Garcia, M. Moreno-Cardoner, A. Albrecht, H. J. Kimble, and D. E. Chang, "Exponential improvement in photon storage fidelities using subradiance & "selective radiance" in atomic arrays," *Physical Review X*, vol. 7, no. 3, pp. 1–36, 2017.

[246] M. T. Manzoni, M. Moreno-Cardoner, A. Asenjo-Garcia, J. V. Porto, A. V. Gorshkov, and D. E. Chang, "Optimization of photon storage fidelity in ordered atomic arrays," *New Journal of Physics*, vol. 20, no. 8, 2018.

[247] Y. C. Chen, P. S. Salter, S. Knauer, L. Weng, A. C. Frangeskou, C. J. Stephen, S. N. Ishmael, P. R. Dolan, S. Johnson, B. L. Green, G. W. Morley, M. E. Newton, J. G. Rarity, M. J. Booth, and J. M. Smith, "Laser writing of coherent colour centres in diamond," *Nature Photonics*, vol. 11, no. 2, pp. 77–80, 2017.

[248] J. T. Shen and S. Fan, “ 2 ,” vol. 30, no. 15, pp. 2001–2003, 2005.

[249] T. Caneva, M. T. Manzoni, T. Shi, J. S. Douglas, J. I. Cirac, and D. E. Chang, “Quantum dynamics ofropagatinghotons with strong interactions: A generalized input-output formalism,” *New Journal of Physics*, vol. 17, no. 11, pp. 1–13, 2015.

[250] M. T. Manzoni, D. E. Chang, and J. S. Douglas, “Simulating quantum light propagation through atomic ensembles using matrix product states,” *Nature Communications*, vol. 8, no. 1, pp. 1–10, 2017.

[251] H. T. Dung, L. Knöll, and D. G. Welsch, “Resonant dipole-dipole interaction in the presence of dispersing and absorbing surroundings,” *Physical Review A - Atomic, Molecular, and Optical Physics*, vol. 66, no. 6, p. 16, 2002.

[252] F. T. Arecchi, “Theory of Optical Maser Amplifiers,” 1964.

[253] C. W. Gardiner and M. J. Collett, “Input and output in damped quantum systems: Quantum stochastic differential equations and the master equation,” *Physical Review A*, vol. 31, no. 6, pp. 3761–3774, 1985.

[254] P. Solano, P. Barberis-Blostein, F. K. Fatemi, L. A. Orozco, and S. L. Rolston, “Super-radiance reveals infinite-range dipole interactions through a nanofiber,” *Nature Communications*, vol. 8, no. 1, pp. 1–7, 2017.

[255] M. J. Burek, Y. Chu, M. S. Liddy, P. Patel, J. Rochman, S. Meesala, W. Hong, Q. Quan, M. D. Lukin, and M. Lončar, “High quality-factor optical nanocavities in bulk single-crystal diamond,” *Nature communications*, vol. 5, no. 1, pp. 1–7, 2014.

[256] N. V. Corzo, B. Gouraud, A. Chandra, A. Goban, A. S. Sheremet, D. V. Kupriyanov, and J. Laurat, “Large Bragg Reflection from One-Dimensional Chains of Trapped Atoms Near a Nanoscale Waveguide,” *Physical Review Letters*, vol. 117, no. 13, pp. 1–6, 2016.

[257] J. D. Hood, *Atom-light interactions in a photonic crystal waveguide*. PhD thesis, California Institute of Technology, 2017.

[258] A. Asenjo-Garcia, J. D. Hood, D. E. Chang, and H. J. Kimble, “Atom-light interactions in quasi-one-dimensional nanostructures: A Green’s-function perspective,” *Physical Review A*, vol. 95, no. 3, pp. 1–16, 2017.

[259] L. Novotny and B. Hecht, *Principles of Nano-Optics*. 316.

[260] Y.-C. Chen, B. Griffiths, L. Weng, S. S. Nicley, S. N. Ishmael, Y. Lekhai, S. Johnson, C. J. Stephen, B. L. Green, G. W. Morley, M. E. Newton, M. J. Booth, P. S. Salter, and J. M. Smith, “Laser writing of individual nitrogen-vacancy defects in diamond with near-unity yield,” *Optica*, vol. 6, no. 5, p. 662, 2019.

[261] D. E. Chang, L. Jiang, A. Gorshkov, and H. Kimble, “Cavity qed with atomic mirrors,” *New Journal of Physics*, vol. 14, no. 6, p. 063003, 2012.

[262] D. Riedel, I. Söllner, B. J. Shields, S. Starosielec, P. Appel, E. Neu, P. Maletinsky, and R. J. Warburton, "Deterministic enhancement of coherent photon generation from a nitrogen-vacancy center in ultrapure diamond," *Physical Review X*, vol. 7, no. 3, pp. 1–8, 2017.

[263] J. Michl, T. Teraji, S. Zaiser, I. Jakobi, G. Waldherr, F. Dolde, P. Neumann, M. W. Doherty, N. B. Manson, J. Isoya, *et al.*, "Perfect alignment and preferential orientation of nitrogen-vacancy centers during chemical vapor deposition diamond growth on (111) surfaces," *Applied Physics Letters*, vol. 104, no. 10, p. 102407, 2014.

[264] "Lumerical inc. https://www.lumerical.com/products/,"

[265] D. M. Toyli, C. D. Weis, G. D. Fuchs, T. Schenkel, and D. D. Awschalom, "Chip-scale nanofabrication of single spins and spin arrays in diamond," *Nano letters*, vol. 10, no. 8, pp. 3168–3172, 2010.

[266] L. Bassett, F. Heremans, C. Yale, B. Buckley, and D. Awschalom, "Electrical tuning of single nitrogen-vacancy center optical transitions enhanced by photoinduced fields," *Physical review letters*, vol. 107, no. 26, p. 266403, 2011.

[267] N. H. Wan, T.-J. Lu, K. C. Chen, M. P. Walsh, M. E. Trusheim, L. De Santis, E. A. Bersin, I. B. Harris, S. L. Mouradian, I. R. Christen, *et al.*, "Large-scale integration of artificial atoms in hybrid photonic circuits," *Nature*, vol. 583, no. 7815, pp. 226–231, 2020.

[268] S. Pezzagna, B. Naydenov, F. Jelezko, J. Wrachtrup, and J. Meijer, "Creation efficiency of nitrogen-vacancy centres in diamond," *New Journal of Physics*, vol. 12, no. 6, p. 065017, 2010.

[269] S. Pezzagna, D. Wildanger, P. Mazarov, A. D. Wieck, Y. Sarov, I. Rangelow, B. Naydenov, F. Jelezko, S. W. Hell, and J. Meijer, "Nanoscale engineering and optical addressing of single spins in diamond," *small*, vol. 6, no. 19, pp. 2117–2121, 2010.

[270] N. V. Corzo, J. Raskop, A. Chandra, A. S. Sheremet, B. Gouraud, and J. Laurat, "Waveguide-coupled single collective excitation of atomic arrays," *Nature*, vol. 566, no. 7744, pp. 359–362, 2019.

[271] J. D. Hood, A. Goban, A. Asenjo-Garcia, M. Lu, S. P. Yu, D. E. Chang, and H. J. Kimble, "Atom-atom interactions around the band edge of a photonic crystal waveguide," *Proceedings of the National Academy of Sciences of the United States of America*, vol. 113, no. 38, pp. 10507–10512, 2016.

[272] A. Batalov, C. Zierl, T. Gaebel, P. Neumann, I.-Y. Chan, G. Balasubramanian, P. Hemmer, F. Jelezko, and J. Wrachtrup, "Temporal coherence of photons emitted by single nitrogen-vacancy defect centers in diamond using optical rabi-oscillations," *Physical review letters*, vol. 100, no. 7, p. 077401, 2008.

[273] M. Hanks, M. Trupke, J. Schmiedmayer, W. J. Munro, and K. Nemoto, "High-fidelity spin measurement on the nitrogen-vacancy center," *New Journal of Physics*, vol. 19, no. 10, p. 103002, 2017.

[274] A. Sipahigil, R. E. Evans, D. D. Sukachev, M. J. Burek, J. Borregaard, M. K. Bhaskar, C. T. Nguyen, J. L. Pacheco, H. A. Atikian, C. Meuwly, R. M. Camacho, F. Jelezko, E. Bielejec, H. Park, M. Lončar, and M. D. Lukin, "An integrated diamond nanophotonics platform for quantum-optical networks," *Science*, vol. 354, no. 6314, pp. 847–850, 2016.

[275] A. Sipahigil, M. D. Lukin, A. Sipahigil, and M. D. Lukin, "Quantum optics with diamond color centers coupled to nanophotonic devices," *Current Trends in Atomic Physics*, pp. 1–28, 2019.